



UCGE Reports

Number 20303

**Department of Geomatics Engineering**

**Tracking Techniques for GNSS Data/Pilot Signals**  
(URL: <http://www.geomatics.ucalgary.ca/graduatetheses>)

**by**

**Kannan Muthuraman**

January 2010



UNIVERSITY OF CALGARY

Tracking Techniques for GNSS Data/Pilot Signals

by

Kannan Muthuraman

A THESIS

SUBMITTED TO THE FACULTY OF GRADUATE STUDIES  
IN PARTIAL FULFILMENT OF THE REQUIREMENTS FOR THE  
DEGREE OF DOCTOR OF PHILOSOPHY

DEPARTMENT OF GEOMATICS ENGINEERING

CALGARY, ALBERTA

JANUARY, 2010

© Kannan Muthuraman 2010

## ABSTRACT

The introduction of the pilot channel in addition to the navigation data is one of the major developments in the modernized GPS and the new Global Navigation Satellite Systems (GNSS). Although both data and pilot channels pass through the same communication channel before reaching the receiver antenna, joint data/pilot processing is often overlooked as it risks compromising the advantages of utilizing the pilot alone. This dissertation identifies and provides a detailed analysis of issues related to joint data/pilot carrier frequency and phase tracking. Two different methods are proposed to overcome these issues: (i) an adaptive bandwidth joint data/pilot phase tracking loop, and (ii) a Kalman filter based joint data/pilot tracking. Both the adaptive bandwidth algorithm and the Kalman filter utilize carrier-to-noise density ratio ( $C/N_0$ ) estimates as a measure of thermal noise. Hence, it was necessary to have a reliable technique for estimating  $C/N_0$  and a comprehensive analysis of the  $C/N_0$  estimation process with emphasis on the use of both the data and pilot channels as input is provided. This analysis is utilized for the design of a novel iterative joint data/pilot  $C/N_0$  estimator, which is shown to be reliable (in terms of bias and noise variance) under weak signal environments. The  $C/N_0$  estimator has been integrated with the proposed tracking strategies that have been analyzed with respect to pilot-only tracking. The results indicate no significant performance loss in terms of tracking sensitivity when using joint data/pilot tracking. On the contrary, joint data/pilot tracking is more effective under weak signal and dynamic conditions.

## ACKNOWLEDGEMENTS

I am fortunate to have Professor Gérard Lachapelle and Professor Richard Klukas as my supervisors, who allowed me to work without defined bounds. Their boundless support, throughout the research work, helped in the completion of this dissertation. Further, being a proud member of the Position, Location And Navigation group, I had the opportunity to develop valuable professional relationships, which will help me further in my future work environment. External Examiners Dr. Fabio DAVIS and Professor Brent Maundy are gratefully acknowledged for their valuable comments and suggestions. iCORE, part of Alberta Innovates – Technology Futures, and the GEOIDE NCE are acknowledged for their financial support.

Sincere thanks to Dr. Daniele Borio, who was always available for lengthy discussions (with a candy break). His thorough knowledge of the subject matter helped me to realize new possible dimensions of this research work. His help in organizing and structuring the thesis content further improved the quality of my dissertation. I had the opportunity to interact with him, regarding my thesis, for over a year. His guidance in this short span of time helped me in viewing things from a totally different perspective. I am sure that these valuable qualities, which I earned from him, will take me long way out into the future. *Thanks Daniele...!*

Dr. Cillian O’ Driscoll and Professor Mark Petovello are the ones who inspired and motivated me during the crucial initial stages of my research. I am also thankful to them for patiently answering the questions of a fresh graduate student. I also wish to acknowledge a good friend of mine, Dr. Surendran K Shanmugam, for helping me right

from the time I landed in Calgary. His guidance, technical as well as personal, has always helped me to take the right step in my career.

I am also thankful to:

- Shashank, Prathiba and Anshu – Working alongside fresh graduate students helped me to revive my transient response and quickly complete my thesis.
- Cyrille Gernot, Florence Macchi, Ali Broumandan, Saloomeh Abbasiannik, Cécile Mongrédien, Vahid Dehghanian, Pejman Kazemi, and Aiden Morrison, with whom I started exploring this world of navigation.
- Brittany Welsh – For her timely help with the proof-reading part.
- Graduate students belonging to the PLAN group for providing me a memorable learning experience.

Special thanks to Gopi, Kumaran, Poorni, Vani and their family for providing me a healthy personal life, ‘a world outside books’. Without their constant care, I wouldn’t have been able to score in academics. Work tensions would fly away, when my cute models Harini and Naren were in sight. Thanks Saranya, Suresh, Brijesh and Shreya for all your good wishes.

*A distant ray of hope that lights my path...*

*To my dad, mom, aunt and my sweet sister...*

## Table of Contents

ABSTRACT .....	iii
ACKNOWLEDGEMENTS .....	iv
Table of Contents .....	vii
List of Tables .....	x
List of Figures and Illustrations .....	xi
List of Abbreviations .....	xv
CHAPTER ONE: INTRODUCTION .....	1
1.1 Modernization Efforts .....	2
1.2 Motivation .....	5
1.3 Relevant Research .....	7
1.4 Thesis Objectives .....	13
1.5 Thesis Outline and Contributions .....	14
CHAPTER TWO: LEGACY GPS-C/A CODE AND MODERNIZED GPS-L2C RECEIVER DESIGN .....	17
2.1 Legacy GPS Signal .....	17
2.2 Legacy GPS Receiver Architecture .....	19
2.2.1 Antenna and Low-Noise Amplifier .....	20
2.2.2 Down Converters and Amplifiers .....	22
2.2.3 Automatic Gain Control (AGC) and Analog to Digital Converter (ADC) .....	23
2.2.4 Signal Processing Block .....	23
2.2.5 User Position Computation .....	28
2.3 Limitations of the Legacy GPS Signal .....	29
2.4 GPS L2-Civilian (L2C) signal .....	29
2.4.1 L2C Signal Structure .....	31
2.4.2 Limitations of L2C signal .....	33
2.5 L2C Software Receiver .....	34
2.5.1 Local Code Generation .....	34
2.5.2 L2C Acquisition .....	36
2.5.3 L2C Tracking .....	38
CHAPTER THREE: THEORETICAL BOUNDS AND RELIABLE $C/N_0$ ESTIMATION FOR MODERNIZED GNSS SIGNALS .....	40
3.1 Introduction .....	41
3.2 Signal Model .....	46
3.2.1 Data Channel Observations .....	46
3.2.2 Pilot Channel Observations .....	47
3.2.3 $C/N_0$ Estimation Model .....	48
3.3 CRLB for $C/N_0$ estimation .....	48
3.3.1 Case – 1: Pilot Channel .....	49
3.3.2 Case – 2: Data Channel .....	49
3.3.3 Case – 3: Joint Data/Pilot .....	50
3.3.4 Properties of $h(\boldsymbol{\alpha}, \mathbf{K})$ .....	53
3.3.5 Theoretical Gain Analysis of Joint Data/Pilot $C/N_0$ estimation .....	55

3.3.5.1 Theoretical Bound on Achievable Gain.....	55
3.3.5.2 Effect of $T_{\text{coh}}$ on achievable gain .....	56
3.4 Maximum Likelihood (ML) Estimators .....	57
3.4.1 ML Estimator – Data Channel.....	57
3.4.2 Iterative ML Estimator – Data Channel .....	59
3.4.3 Joint Data/Pilot ML Estimator.....	64
3.4.4 Performance Analysis.....	65
3.5 Implementation Aspects .....	68
3.6 Test Methodology .....	71
3.7 Results.....	71
3.8 Summary.....	74
CHAPTER FOUR: JOINT DATA/PILOT CARRIER FREQUENCY TRACKING .....	75
4.1 FLL Theory.....	76
4.2 Joint Data/Pilot Tracking .....	82
4.3 On-The-Fly Variance Estimation.....	85
4.4 Results.....	88
4.4.1 Numerical Simulation.....	88
4.4.1.1 Scenario Description.....	88
4.4.1.2 Test Methodology .....	88
4.4.1.3 Analysis of Results .....	89
4.4.2 Validation of Results with Live Signals.....	92
4.4.2.1 Test Methodology .....	92
4.4.2.2 Analysis of Results .....	94
CHAPTER FIVE: METHODS FOR JOINT DATA/PILOT CARRIER PHASE TRACKING.....	96
5.1 Phase Discriminator Overview .....	98
5.2 Literature Review .....	99
5.3 Motivation and Proposed Methods.....	101
5.4 Methods for Joint Data/Pilot Tracking .....	103
5.4.1 Method 1: Weighted Discriminator Combination with ATAN2 Discriminator on Both Channels.....	103
5.4.2 Method 2: Kalman Filter based Joint Data/Pilot Tracking.....	104
5.5 Adaptive Bandwidth Tuning.....	106
5.5.1 Design in the Analog Domain .....	106
5.5.2 Algorithm Validation.....	111
5.5.3 Issues .....	113
5.5.4 All-Digital Adaptive Bandwidth Tracking Design.....	114
5.5.4.1 Expression for Dynamic Stress Error .....	115
5.5.4.2 Expression for Tracking Jitter due to Thermal Noise.....	116
5.5.4.3 Model Validation .....	118
5.5.4.4 Stability Constraints and Noise bandwidth Estimate for DPLL .....	120
5.5.4.5 Validation of Adaptive Noise Bandwidth Algorithm.....	121
5.5.5 Extension to Weighted Discriminator Combination .....	125

CHAPTER SIX: ADAPTIVE BANDWIDTH DATA/PILOT CARRIER PHASE TRACKING RESULTS.....	129
6.1 Tracking Sensitivity .....	129
6.1.1 Test Setup .....	130
6.1.2 Results .....	133
6.2 Dynamic Scenarios .....	136
6.2.1 Scenario 1: User Dynamics under Weak Signal Conditions .....	136
6.2.1.1 Test Methodology .....	138
6.2.1.2 Results.....	139
6.2.2 Scenario 2: Test under Dynamics with Different Acceleration Stress .....	143
6.2.2.1 Results.....	144
6.3 Summary .....	147
CHAPTER SEVEN: CONCLUSIONS AND RECOMMENDATIONS .....	148
7.1 Conclusions.....	148
7.1.1 Reliable $C/N_0$ Estimation .....	148
7.1.2 Joint Data/Pilot Carrier Frequency Tracking .....	149
7.1.3 Joint Data/Pilot Carrier Phase Tracking .....	151
7.2 Recommendations for Future Work .....	153
REFERENCES .....	156
APPENDIX A: DESIGN OF KALMAN FILTER BASED CARRIER AND CODE TRACKING.....	167
A.1 State Space Model.....	167
A.2 Process Noise .....	169
A.3 Observation Model.....	171
A.4 Observation Noise.....	173
A.5 Necessary Changes for Joint Data/Pilot Tracking .....	174
APPENDIX B: IDENTITIES USED IN THE DERIVATION OF CRLB FOR $C/N_0$ ESTIMATION .....	176
B.1 Identity 1 .....	176
B.2 Identity 2 .....	177
APPENDIX C: CRLB FOR PHASE ESTIMATION IN AWGN CHANNEL.....	178

## List of Tables

Table 5-1: Costas Loop Discriminators .....	98
---	----

## List of Figures and Illustrations

Figure 2-1: Generic GPS receiver block diagram.....	20
Figure 2-2: Carrier tracking loop block diagram .....	26
Figure 2-3: Time multiplexed data and pilot channel generation .....	31
Figure 2-4: Zero padded local code generation for L2C signals .....	36
Figure 2-5: CM code acquisition for PRN 15 (live data) (a) Normalized autocorrelation values across all code phase shifts for a Doppler of -350 Hz (b) Zoomed in view of autocorrelation peak .....	38
Figure 2-6: Normalized correlation plot for 75 different segments of CL code for PRN 15.....	38
Figure 3-1: Analysis of the reliability of the standard $C/N_0$ estimator (averaged across 6 satellites) .....	43
Figure 3-2: Plot of the integrand of $h(\alpha, K)$ for different $T_{coh}$ and $K$ at a $C/N_0$ of 8 dB-Hz.....	53
Figure 3-3: Plot of $h(\alpha, K)$ against $C/N_0$ for different values of $T_{coh}$ and $K = 20/T_{coh}$ .....	54
Figure 3-4: Theoretical gain in noise variance reduction by using both the data and pilot channels for $C/N_0$ estimation as compared to using pilot channel only .....	56
Figure 3-5: The mean of $\tanh(2\alpha y_m/A)$ evaluated as a function of $C/N_0$ with unit amplitude ( $A=1$ ).....	59
Figure 3-6: Performance analysis of iterative MLE against MLE with approximation using data channel only.....	61
Figure 3-7: Plot of $g_{ML,d}(a)$ for a $C/N_0$ of 15 dB-Hz under two different conditions (i) Convergence and (ii) Divergence. The reference curve corresponds to the noiseless condition. Original amplitude ( $A$ ) is set as 10. ....	62
Figure 3-8: Convergence percentage for the iterative ML estimator using data channel only .....	63
Figure 3-9: Comparison of MLE using both the data and pilot channels (DP) (i) with approximation (MLE-DP) (ii) iterative procedure (MLE-DP Iterative) against a MLE using pilot channel only (MLE-Pilot).....	66
Figure 3-10: Comparison of gain in noise variance reduction by using both the data and pilot channels as compared to using pilot channel alone .....	67

Figure 3-11: Comparison of convergence percentage between iterative MLE using data channel alone and iterative MLE using both the data and pilot channels .....	68
Figure 3-12: Algorithm flow as implemented in the software receiver .....	70
Figure 3-13: Bias in estimates obtained from different estimators across $C/N_0$ .....	72
Figure 3-14: Gain in noise variance reduction of data/pilot combined $C/N_0$ estimation as compared to MLE which uses pilot channel only .....	73
Figure 4-1: Cross product frequency discriminator .....	78
Figure 4-2: Normalized cross product frequency discriminator gain .....	79
Figure 4-3: Normalized four-quadrant arctangent (ATAN2) discriminator gain .....	80
Figure 4-4: Normalized cross product with decision feedback discriminator gain .....	82
Figure 4-5: Block diagram of Variance Estimation Loop (Moir 2001) .....	85
Figure 4-6: Measured standard deviations of data and pilot channel frequency discriminator outputs. Corresponding $C/N_0$ for each time interval is given in dB-Hz above the arrows .....	87
Figure 4-7: Comparison of frequency jitter across different implementations to track data and pilot channels .....	90
Figure 4-8: Block diagram of data collection and processing setup .....	92
Figure 4-9: Measured $C/N_0$ of reference and attenuated channels .....	93
Figure 4-10: Frequency jitter comparison across different discriminator implementations with live data for $B_n = 4$ Hz and $T_{coh} = 5$ ms .....	95
Figure 5-1: Bias in phase error estimate using ATAN and ATAN2 (with correction for data bits) on the data channel for phase errors ( $\Delta\Phi$ ) (i) $15^\circ$ (ii) $30^\circ$ (iii) $45^\circ$ ....	104
Figure 5-2: Effect of dynamic stress on discriminator outputs .....	109
Figure 5-3: Dynamic stress measured by two independent PLL with different noise bandwidth is scaled by their respective $\omega_n^2$ and plotted against the true reference.	110
Figure 5-4: Doppler Estimate for PRN 31 with a linear fit of the obtained estimates....	112
Figure 5-5: Noise bandwidth estimates ( $B_{n,APLL}$ ) obtained using the adaptive noise bandwidth algorithm for PRN 31 .....	113
Figure 5-6: Linear model of DPLL with the proposed adaptive noise bandwidth algorithm .....	114

Figure 5-7: Comparison of fit of different models for noise variance at the output of arc tangent discriminator.....	117
Figure 5-8: Comparison of measured tracking jitter due to thermal noise for APLL and DPLL with their respective models for a $C/N_0$ of 37 dB-Hz .....	119
Figure 5-9: Comparison of measured tracking jitter due to thermal noise for APLL and DPLL with their respective models for a $C/N_0$ of 20 dB-Hz .....	120
Figure 5-10: Cost function (theoretical and measured) for the design in the analog (APLL) and digital domain (DPLL) along with the noise bandwidth estimated by the proposed algorithm for a $C/N_0$ of 37 dB-Hz. ....	122
Figure 5-11: Cost function (theoretical and measured) for the APLL and DPLL design along with the noise bandwidth estimated by the proposed algorithm for a $C/N_0$ of 20 dB-Hz.....	123
Figure 5-12: Comparison of actual and theoretically predicted noise bandwidth estimates.....	124
Figure 5-13: Comparison of theoretical and measured cost functions of the APLL and the DPLL with the adaptive bandwidth algorithm.....	125
Figure 5-14: Difference between the noise variance of the phase discriminator outputs on the data and pilot channels. ....	126
Figure 5-15: Block diagram of the proposed method for joint data/pilot carrier phase tracking .....	127
Figure 6-1: Block diagram of data collection and processing setup.....	131
Figure 6-2: Sample plot of measured $C/N_0$ on reference and attenuated channels.....	132
Figure 6-3: Noise bandwidths selected by the adaptive bandwidth algorithms for single channel and data/pilot tracking.....	133
Figure 6-4: Performance comparison of carrier phase tracking methods based on tracking threshold.....	135
Figure 6-5: Velocity profile of the receiver simulated using the Spirent hardware simulator .....	136
Figure 6-6: Sample of true Doppler obtained from the Spirent hardware simulator corresponding to a rectangular trajectory.....	137
Figure 6-7: $C/N_0$ profile chosen for the test under user dynamics.....	138
Figure 6-8: User trajectory with $C/N_0$ level information .....	138

Figure 6-9: Sample plot of noise bandwidths chosen by single channel and data/pilot tracking .....	140
Figure 6-10: Ability of the single channel and data/pilot tracking methods to maintain lock under (i) 85-275 s corresponding to 16.5 dB-Hz and (ii) 275-450 s corresponding to 15.5 dB-Hz. (PRN 04) .....	141
Figure 6-11: Comparison of single channel tracking with data/pilot tracking in dynamics conditions under $C/N_0$ close to their tracking threshold.....	142
Figure 6-12: Vehicle Trajectory with increasing acceleration stress.....	143
Figure 6-13: Comparison of noise bandwidth estimate used by joint data/pilot and pilot-only tracking loops .....	144
Figure 6-14: Sample plot of bias in Doppler estimates and measured $C/N_0$ for satellites away from zenith (elevation angle around $45^0$ ) corresponding to the step trajectory .....	145
Figure 6-15: Comparison of bias in Doppler estimates and measured $C/N_0$ for a reference frequency trajectory with spikes due to acceleration stress (step trajectory).....	146

## List of Abbreviations

<b>Symbol</b>	...	<b>Definition</b>
ADC	...	analog-to-digital converter
AGC	...	automatic gain control
APLL	...	analog phase locked loop
ATAN	...	arctangent
ATAN2	...	four quadrant arctangent
AWGN	...	additive white Gaussian noise
BER	...	bit error rate
BOC	...	binary offset carrier
BPF	...	band pass filter
bps	...	bits per second
BPSK	...	binary phase shift keying
BW	...	bandwidth
C/A	...	coarse/acquisition
$C/N_0$	...	carrier-to-noise density
CDMA	...	code division multiple access
CL	...	civil-long
CM	...	civil-moderate
CNAV	...	civil navigation
CRLB	...	Cramer-Rao lower bound
DPLL	...	digital phase locked loop
EKF	...	extended Kalman filter
FDMA	...	frequency division multiple access
FLL	...	frequency locked loop
FOC	...	fully operational capability
GIOVE	...	Galileo in-orbit validation element
GLONASS	...	Global Navigation Satellite System
GNSS	...	Global Navigation Satellite System
GPS	...	Global Positioning System
$GSNR_x^{TM}$	...	GNSS software navigation receiver
IF	...	intermediate frequency
IRNSS	...	Indian Regional Navigational Satellite System
KF	...	Kalman filter
L2C	...	L2-civil
LF	...	loop filter
LFSR	...	linear feedback shift register
LHCP	...	left hand circular polarized
LNA	...	low noise amplifier
LOS	...	line-of-sight
m- sequence	...	maximum-length sequence
ML	...	maximum-likelihood
MLE	...	maximum-likelihood estimator
mWatt	...	milliWatt
NAV	...	navigation data (as transmitted on L1 C/A signal)

NBP	...	narrow band power
NCO	...	numerically controlled oscillator
NF	...	noise figure
NI	...	National Instruments
pdf	...	probability density function
PLL	...	phase locked loop
RF	...	radio frequency
RHCP	...	right hand circular polarized
SA	...	selective ability
SE	...	standard estimator for $C/N_0$
SNR	...	signal-to-noise ratio
SPS	...	standard positioning service
SV	...	satellite vehicle
WBP	...	wide band power
QZSS	...	Quasi-Zenith Satellite System

## CHAPTER ONE: INTRODUCTION

Civilian use of satellite-based navigation systems is growing steadily. The Global Positioning System (GPS) is a constellation of medium earth orbit satellites. Although GPS was developed primarily for military applications, it has been serving an increasing number of civilian users since fully operational capability (FOC) was declared. Civilian usage accelerated with the removal of Selective Availability (SA) from the civilian signal on May 1, 2000 (The White House 2000). This commitment to increased civilian accuracy was reaffirmed with the decision to procure future GPS III satellites without the SA feature (PNT 2007). Although the removal of SA improved the attainable accuracy with legacy GPS L1 coarse/acquisition (C/A) signals, system performance is still limited by the fact that signal design was based on 1970s-era technologies, with rack mounted receivers capable of 5-channel analog signal processing. Current technology can house nearly fifty channels with over a million correlators, along with other interfacing options, all in a few millimetres of integrated circuit footprint, with power consumption on the order of milliwatts and at a very low cost (U-blox 2008). This advance in technology, together with the ever-increasing number of applications, made it necessary to improve the availability and accuracy of GPS signals, making them usable in harsh environments, particularly in the presence of

- i. Massive signal attenuation
- ii. Intentional or unintentional interference, and
- iii. Multipath effects.

In such environments, the receiver performance is severely degraded, as the signal design of legacy GPS was originally intended for line-of-sight (LOS) positioning.

Moreover, the primary purpose of coarse/acquisition (C/A)-code modulation, the only publically available legacy GPS signal, was aiding acquisition of the P(Y) military signal. Thus, the emerging applications for GPS demand a higher standard of performance under environments for which it was not originally designed. This change in the way GPS is used has motivated its modernization. This dissertation identifies possible improvements in tracking performance using modernized signals.

### **1.1 Modernization Efforts**

To overcome the inherent limitations of legacy GPS signals and to meet the increasing demands of location-based services (LBS), the GPS constellation is being modernized to include new signals at the L1 (1575.42 MHz), L2 (1127.6 MHz) and L5 (1176.45 MHz) frequencies. These modernizations are listed below in the expected order of availability:

- i. A new civilian signal, the L2-civil (L2C) on the L2 frequency, is targeted at the development of low-cost, dual-frequency civilian GPS receivers with the ability to correct for ionospheric errors.
- ii. A civilian signal in the L5 band, which lies in the aeronautical and radio navigation services band, intended for safety-of-life applications.
- iii. A civilian signal on the L1 frequency, L1C, in addition to the existing legacy C/A signal, to maintain interoperability with the European Union's GALILEO system and Japan's Quasi-Zenith Satellite System (QZSS) (Betz et al 2007) and provide improved performance.

The proposed signal design for these modernizations is the result of extensive research and the vast experience gained with the existing system over the years. The most

significant change included in the modernized signals is the use of longer spreading codes and the addition of dataless channels (pilot). Longer spreading codes provide better correlation properties and help to reduce self-interference effects. Self-interference is the condition whereby a strong cross-correlation peak is greater in magnitude than the autocorrelation peak of a weaker signal. The pilot channel aids weak signal tracking. Modernization has also ensured complementary signal designs that will enhance the performance of a multi-frequency GPS receiver. Thus, very high accuracies can be obtained by combining carrier phase measurements from all the civilian signals (Kaplan 2006). Apart from combining, there is also the option to choose one signal over another based on their reliability; this is important in applications where integrity is of concern, such as safety-critical applications including aviation and marine navigation.

Apart from GPS modernization, a number of other Global Navigation Satellite Systems (GNSS) are being built to provide civilian users with reliable positioning anywhere. GLONASS – Global Navigation Satellite System, the Russian counterpart originally initiated in 1976, was revived in 2003, with new satellite launches and signals still being added. At the time of this writing, the GLONASS constellation had 16 satellites in operational capability on three orbital planes, toward the target of a full constellation of 24 satellites (Polischuk et al 2002, Information-Analytical Centre 2009). The proposed GLONASS modernization includes doubling the power on the L2 signal in the M-satellites, precise cesium clocks and, more importantly, open code division multiple access (CDMA) signals with binary offset carrier (BOC) modulation at 1575.42 MHz and 1176.45 MHz, in addition to the existing frequency division multiple access (FDMA) GLONASS signals (Gibbons 2008). The latter is of importance since it

improves the interoperability of the system with the existing GPS signals, and also with the other CDMA-based GNSS currently being built by other countries. These new CDMA signals are scheduled to be transmitted by the third generation of GLONASS-K satellites.

The other major GNSS under development is GALILEO, a project of the European Union, which aims to produce a system of 30 satellites transmitting signals in four bands, namely the E5a (coinciding with L5 – 1176.45 MHz), E5b (1207.14 MHz), E6 (1278.75 MHz) and L1 (1575.42 MHz) bands. With the exception of the E6 signal, these modulations carry an open access signal for civilian users. Apart from a higher minimum received signal power, as compared to the existing GPS L1, and the usage of BOC modulations, a notable feature of the signal design for all four GALILEO bands is that they will contain both data and pilot channels (OS SIS ICD 2006). Further, the signal design also ensures interoperability with GPS signals, thus significantly reducing the complexity of future multi-frequency, multi-constellation receivers. At the time of this writing, two Galileo in-orbit validation element (GIOVE-A and B) satellites are operational (GIOVE 2008).

Other navigation systems currently being built include the Chinese Compass (Beidou – 2) System and the Indian Regional Navigational Satellite System (IRNSS). The former is proposed to be a constellation of 35 satellites, of which 5 are geostationary and 30 are medium earth orbit satellites, whereas the latter is aimed at providing regional navigational capabilities within India using geostationary and geo-synchronous (inclined) orbit satellites (Gao et al 2008, SATNAV 2006). Further, the Japanese Quasi-Zenith

Satellite System (QZSS) is proposed as system of three satellites to augment the GPS within the country and also to aid in regional time transfer.

## 1.2 Motivation

To summarize the modernization efforts across different constellations, the following are considered to be the major changes in GNSS signal design as compared to the legacy GPS L1 C/A signal:

- i. Spreading codes with better correlation properties;
- ii. Enhanced modulation techniques;
- iii. Increased nominal received signal power;
- iv. Faster chipping rates for the spreading sequences and larger bandwidth;
- v. Inclusion of a pilot (dataless) channel in addition to the navigation data channel.

Not all the changes mentioned above are included in each proposed modernized signal. However, the inclusion of a dataless (pilot) channel is found across most of the modernized signals. This is because the use of a pilot channel is widely considered a necessity for improving performance under weak signal environments. Although there is a 3 dB loss due to equal power sharing associated with transmitting an additional signal from a satellite, the advantages outweigh this limitation. The advantages include (i) the ability to average the signal longer under heavy attenuations, and (ii) more robust carrier phase tracking, which is often described as the weakest link in the signal processing blocks of a receiver (Ward et al 2006).

Apart from these advantages, the Doppler shift and code delay of a pilot channel are identical to that of a data channel. Hence, the pilot channel can be considered as an

additional observation. Further, the noise corrupting the data and pilot channels are statistically independent due to one or more of the following features, depending on the signal under consideration:

- i. Transmission using orthogonal carrier components;
- ii. Usage of time-multiplexed data/pilot signals; and
- iii. Usage of different spreading codes for data and pilot channel.

In the third case, even if the receiver noise corrupting the data and pilot channels is identical, the two channels are despread using their respective codes. After despreading, the correlation between the noise corrupting the accumulated correlator outputs of the data and pilot channels is given by the cross-correlation between their respective spreading codes (Van Dierendonck et al 1992). This cross-correlation is negligible, and the two correlator outputs can be considered to be affected by independent noise. Thus, the pilot channel provides an extra and independent observation for the parameters that are to be estimated. This makes joint data/pilot processing an advantageous option to improve signal tracking performance in a receiver. Apart from signal tracking, other blocks, such as carrier-to-noise density ( $C/N_0$ ) estimators, can also benefit from data/pilot combining. Hence, the motivation of this thesis is to develop signal tracking and  $C/N_0$  estimation algorithms that effectively make use of the available data and pilot channels, without losing the advantages of tracking the pilot channel alone.

For validation and analysis of the proposed algorithms, the GPS-L2C signal was used in this thesis. The reasons for this choice are:

- i. Availability of live GPS-L2C signals currently being transmitted by 8 IIR-M satellites (USNO 2009);

- ii. Availability of a Spirent GSS7700 GPS hardware simulator capable of generating the L2C signals for analysis under controlled environments.

Although the algorithms proposed in this thesis are evaluated with one variant of the modernized navigation signal, they are general in nature and can be extended to other signals with little or no modifications.

### **1.3 Relevant Research**

Methods found in the literature to use both data and pilot channels for signal tracking mostly address this problem in the context of GPS L5 signals. However, these algorithms are general and can be applied to any signal with a data/pilot structure. Spilker & Van Dierendonck (1999) suggest a non-coherent combination of the data and pilot channels in order to improve code tracking performance for L5 signals. However, they suggest using the pilot channel alone for carrier phase tracking. Similar recommendations can also be found in Ries et al (2002) and Macabiau et al (2003). This is because a pure phase locked loop (PLL) can be used to track a pilot channel. Tracking a pilot channel with a pure PLL aids in weak signal tracking, i.e. the minimum  $C/N_0$  required for tracking a signal using a pure PLL is 6 dB lower than that of Costas loops (Kaplan 2006). By including the data channel in the design of tracking loops, there is the risk of losing the inherent advantages of using a pure PLL. Still, methods are found in the literature to reduce tracking jitter under nominal  $C/N_0$  conditions ( $C/N_0$  greater than 25 dB-Hz) by utilizing joint data/pilot tracking.

Methods available for joint data/pilot tracking can be classified based on the stage at which the information from the data and pilot channels are combined. One possible option is to combine the data and pilot channel accumulated correlator outputs based on

the maximum power constraint (Mongrédien et al 2006). In this case, the data bit is accounted for using a hard decision approach, the reliability of which is limited by the bit-error-rate (BER) as  $C/N_0$  is reduced. Another option is a discriminator-level combination as suggested by Hegarty (1999). In this approach, the accumulated correlator outputs from the data and pilot channels are allowed to pass through their respective discriminators. The discriminator outputs are weighted and combined to obtain an improved estimate of the phase or frequency error. This combination provides a 3 dB noise reduction under ideal conditions (Hegarty 1999, Tran & Hegarty 2002). Further, when the design of the discriminators and the choice of weights are made properly, it is possible to exploit the joint data/pilot tracking, even under weak  $C/N_0$  conditions, without losing the inherent advantages of a pure PLL on the pilot channel alone.

However, the implementation of weighted discriminator combination is not straightforward due to various issues including the choice of discriminator and the presence of data bits on the data channel. When these issues are not addressed properly, the advantages of using the pilot channel alone are lost in joint data/pilot tracking. Methods to overcome some of these issues for carrier phase tracking have been suggested by Ries et al (2002), Tran & Hegarty (2002) and Julien (2005). A detailed study of issues concerning the weighted discriminator combination and methods available in literature to overcome these issues will be presented in later chapters.

Through performance analysis of joint data/pilot tracking algorithms based on their tracking thresholds, it is possible to quantify the extent to which the advantages of pilot-only tracking are sacrificed. Tracking threshold is defined as the minimum  $C/N_0$  required to track the signal with tracking jitter less than a predefined threshold (Kaplan

2006). Tran & Hegarty (2003) report a degradation of approximately 2.5 dB in tracking threshold by using joint data/pilot tracking as compared to the pilot channel alone, for a stationary as well as an airborne receiver utilizing either the GPS L2C or L5 signals. This difference in performance has been reduced by utilizing the following approach in this thesis:

- (i) Ensuring the validity of weights used in the discriminator combination under weak  $C/N_0$  conditions; the weights are usually fixed based on the theoretical models available in the literature (Tran & Hegarty 2002). However, these theoretical models fail under weak  $C/N_0$  conditions due to the non-linear nature of the discriminators. This issue is not addressed in the existing literature. Proper weights can be obtained by computing them on-the-fly.
- (ii) Design of a discriminator combination whose phase pull-in region and linear relationship between the input and output phase errors are not significantly degraded under weak  $C/N_0$  conditions, as compared to that of a pure PLL discriminator; this helps in reducing the bias in phase error estimates and maintaining phase lock under weak  $C/N_0$  conditions. This methodology has not been considered in the design of joint data/pilot tracking methods available in the current literature.
- (iii) Adaptively choosing an optimum noise bandwidth for a given situation; the tracking threshold is a function of the loop noise bandwidth ( $B_n$ ) used by the tracking loops. A large  $B_n$  helps reduce the effect of dynamic stress, whereas a small  $B_n$  reduces the effect of thermal noise on the tracking

loops. Thus, the correct choice of  $B_n$  can help in maintaining lock under weak  $C/N_0$  conditions. Further, adaptive tuning of noise bandwidth can also help in bringing out an advantage of using joint data/pilot tracking as compared to single channel tracking. Since the effect of thermal noise is reduced in joint data/pilot tracking, it is possible to use a larger noise bandwidth as compared to single channel tracking. This helps in maintaining lock under environments where user dynamics and signal power levels are close to the tracking threshold.

The above approaches for improving the performance of joint data/pilot carrier phase tracking are based on a standard tracking architecture, which is a closed loop system with a discriminator, a loop filter (LF) and a numerically-controlled oscillator (NCO). Kalman filter (KF)-based tracking has gained the attention of the navigation community for its improved performance (Psiaki & Jung 2002, Petovello & Lachapelle 2006, Mongrédien et al 2007). A KF can be employed to track both the data and pilot channels by using the maximum power constraint for accumulating the data/pilot correlator outputs. The combined accumulated correlator outputs are then fed as observations to the KF for estimating the tracking parameters. In this case, no significant changes are required in the KF model as compared to the model available in the literature for GPS L1 signals. This was demonstrated for L5 signals by Mongrédien et al (2007). Similarly, KF-based tracking that utilizes accumulated correlator outputs over multiple data bit periods from data and pilot channels is found in Ziedan (2005). Here again, the data and pilot channel accumulated correlator outputs are combined and used as observations for the KF. In both implementations, the KF is not used to weight the data

and pilot channel observations directly. The possibility of using a KF to weight the data and pilot channel observations directly can help in realizing the advantages of joint data/pilot tracking without losing the inherent advantages of pilot-only tracking.

Moreover, the analysis available in the literature for joint data/pilot tracking has been done only for carrier phase and code tracking. The design choices affecting the combination for carrier frequency tracking need to be studied thoroughly, and a detailed performance analysis is required to quantify the advantages and disadvantages of joint data/pilot frequency tracking under weak  $C/N_0$  conditions.

The performance analysis for joint data/pilot carrier phase and frequency can be done under weak  $C/N_0$  conditions in terms of tracking threshold. This involves quantifying the minimum required  $C/N_0$  to track a signal.  $C/N_0$  levels are usually estimated by a receiver using the standard estimator (SE) proposed by Van Dierendonck (1995). The performance of this estimator gets progressively biased as  $C/N_0$  decreases below approximately 23 dB-Hz (Muthuraman et al 2008). Further, the adaptive noise bandwidth algorithm and KF-based tracking both use  $C/N_0$  estimates as a measure of the thermal noise level. Poor estimates of  $C/N_0$  can affect the performance of these algorithms as well. Not limited to the analysis presented in this thesis, most weak GPS signal tracking algorithms found in the literature are analyzed based on their ability to track signals against the  $C/N_0$  levels measured at the receiver end (Kazemi & O'Driscoll 2008, Lashley & Bevely 2008 etc.). Thus, it is important to have a reliable technique to estimate  $C/N_0$ . Also, the theoretical framework of  $C/N_0$  estimation has been only marginally developed in the context of GNSS signals. The problem of  $C/N_0$  estimation can be considered a scaled signal-to-noise ratio (SNR) estimation. Theoretical analysis

for the problem of SNR estimation can be found widely in the communications context (Pauluzzi & Beaulieu 2000, Alagha 2001, Li et al 2002, Chen & Beaulieu 2005 etc.). Still, an analysis of theoretical bounds and achievable performance (in terms of bias and variance) specific to the context of GNSS signals would be more useful to the navigation community.

In the context of GNSS signals, Ramasubramanian & Nadig (2006) address the theoretical analysis by deriving the Cramer-Rao lower bound (CRLB) for  $C/N_0$  estimation for one particular case, where 1 ms accumulated correlator outputs from the data channel are used as observations. Apart from that,  $C/N_0$  estimators derived analytically can be found in Groves (2005), Schmid & Neubauer (2005), Pany & Eissfeller (2006) and Muthuraman et al (2008). These approaches make use of the statistics of the accumulated correlator outputs in order to derive the estimator. The following are limitations of the available literature with regard to  $C/N_0$  estimation:

- i. Bias in  $C/N_0$  estimates under weak  $C/N_0$  conditions and methods to overcome this issue are not addressed;
- ii. Effect of the length of the predetection interval ( $T_{coh}$ ), which is the time period over which the correlator outputs are accumulated and used as inputs for  $C/N_0$  estimators, on  $C/N_0$  estimation; the methods available in the literature use 1 ms accumulated correlator outputs as inputs to  $C/N_0$  estimators (Van Dierendonck 1995). The choice of 1 ms is for implementation ease in receivers using the GPS L1 C/A code, where the C/A code period is 1 ms. However, the period of the spreading codes used

in the modernized signals is different. The advantages and disadvantages in using longer  $T_{coh}$  for  $C/N_0$  estimation require analysis.

- iii. Possibility of utilizing both the data and pilot channels for  $C/N_0$  estimation; the data and pilot channels are transmitted at identical power levels on most modernized GNSS signals, and hence can be used together to estimate the  $C/N_0$ . A detailed theoretical analysis can bring out the advantages in using the pilot channel in addition to the data channel, particularly in the case of weak  $C/N_0$  estimation.

#### **1.4 Thesis Objectives**

In light of the above-mentioned limitations of the methods available in the literature for joint data/pilot tracking and  $C/N_0$  estimation, the objectives of this thesis can be summarized as follows:

- a) Development of a reliable technique to estimate  $C/N_0$  under weak signal conditions; the derived estimator will be used in the performance analysis of the proposed signal tracking algorithms and as a measure of thermal noise in adaptive bandwidth and Kalman filter based tracking methods.
- b) Performance analysis of joint data/pilot carrier frequency tracking using weighted combination of discriminators with emphasis on weak signal environments; this involves identifying the issues, analysing their effects on the signal tracking quality, and proposing solutions to overcome the issues.
- c) Comprehensive design of joint data/pilot carrier phase tracking which does not suffer from performance degradation under weak signal scenarios

as compared to a pure-PLL operating on the pilot channel; issues specific to the case of joint data/pilot carrier phase tracking needs to be identified followed by a detailed design procedure for joint data/pilot tracking using (i) an extension of the standard tracking architecture and (ii) a Kalman filter based tracking architecture.

- d) Design of an adaptive noise bandwidth algorithm; this will help in obtaining a robust tracking loop design for a given scenario and for a fair comparison of the standard tracking with Kalman filter based tracking architecture.
- e) Performance analysis of the proposed methods under weak signal environments and scenarios with some user dynamics in order to quantify the degradation, if any, and to analyse the advantages in using joint data/pilot tracking as compared to using pure-PLL.

The following section describes the organization of the thesis and the research flow, with a brief outline of the contributions made.

### **1.5 Thesis Outline and Contributions**

This dissertation is organized into three broad sections, following a brief review of legacy and modernized GNSS signals in Chapter 2:

- (i)  $C/N_0$  Estimation: Chapter 3 provides a comprehensive theoretical analysis of the  $C/N_0$  estimation process. The emphasis of this chapter is on the theoretical framework for  $C/N_0$  estimation using both the data and pilot channels. A theoretical bound on the amount of noise reduction achievable

in the  $C/N_0$  estimates (using both the data and pilot channels) is derived. The derivation and use of this bound for the analysis of  $C/N_0$  estimators is considered one of the novel contributions of this chapter. Maximum likelihood (ML) estimators that use either the data channel alone or both data and pilot channels are derived, with a detailed analysis on the bias levels and noise variance under weak  $C/N_0$  conditions. A novel iterative method for  $C/N_0$  estimation is proposed initially for the data channel only and then extended to use both channels. The proposed iterative method has been shown to be reliable under weak  $C/N_0$  conditions.  $C/N_0$  estimates obtained using the proposed estimator are employed in the performance analysis of the methods in Chapters 4 – 6.

- (ii) Joint data/pilot carrier frequency tracking: Chapter 4 gives a detailed analysis of issues affecting joint data/pilot carrier frequency tracking using a weighted discriminator combination. Solutions to overcome some issues are provided and a performance analysis comparing joint data/pilot tracking with a single channel (either data or pilot) is given. The results are mainly used as a precursor in understanding the effects of joint data/pilot tracking under weak  $C/N_0$  conditions. This understanding is then utilized while designing joint data/pilot carrier phase tracking methods.
- (iii) Joint data/pilot carrier phase tracking: Chapters 5 and 6 provide an analysis of design choices and issues in joint data/pilot carrier phase tracking. Two novel methods to effectively make use of both data and pilot channels for carrier phase tracking, without significantly losing the

inherent advantages of a pure PLL, are described in Chapter 5. Further, the design of a novel adaptive noise bandwidth algorithm for the standard tracking architecture is given. The results for the performance comparison of the proposed methods against pure PLL tracking under environments with weak  $C/N_0$  and user dynamics are provided in Chapter 6.

Finally, Chapter 7 summarizes the thesis contributions, and the conclusions of the thesis are drawn.

## **CHAPTER TWO: LEGACY GPS-C/A CODE AND MODERNIZED GPS-L2C RECEIVER DESIGN**

This chapter briefly discusses the signal structure of the legacy GPS L1 C/A signal and the standard receiver architecture used to acquire and track the signal. Emphasis is given to the carrier tracking module and the received carrier-to-noise density ( $C/N_0$ ) calculations, which form the introductory material to the algorithms proposed in subsequent chapters. The limitations of the legacy L1 C/A signal structure are outlined and the need for signal modernization is clearly stated. The important distinguishing features of the modernized GPS signal structure and their impact on receiver architecture are discussed. The signal structure, code properties, advantages, and limitations of the L2-civilian (L2C) signal are provided. A detailed description of the signal structure can be found in IS-GPS-200-D (2006). Finally, a brief introduction is given on the L2C software receiver developed for implementing and testing the algorithms proposed in this thesis.

### **2.1 Legacy GPS Signal**

The primary GPS ranging signal is transmitted as a binary phase shift keying (BPSK) signal at 1575.42 MHz (L1). It carries navigation data with the coarse/acquisition (C/A) code in phase-quadrature with the precision (P) code. The P-code is the principal ranging code. The C/A code was originally intended as an acquisition aid to the longer P code, which has a code period of seven days at a chipping rate of 10.23 Mbps (Tran & Hegarty 2002). The P code allows more precise ranging than the C/A code. However it is encrypted and only authorized users have access to it. Thus, civilian users, using single frequency (L1) receivers, are limited to the positioning accuracy provided by the C/A

code. Survey grade receivers used in high accuracy applications, in addition to the L1 carrier recovery, attempt to reconstruct the L2 carrier (1227.6 MHz) without the knowledge of the military code P(Y) transmitted on it. They are referred to as either semicodeless or codeless tracking based on the technique used for the L2 carrier recovery. Since they operate without the knowledge of the spreading code, semicodeless or codeless tracking suffer from low signal-to-noise (SNR) problems and lack robustness (Woo 1999).

The use of the C/A code for positioning is referred to as standard positioning service (SPS). The C/A code is a short code with a period of  $2^{10}-1$  (1023) bits transmitted at a chipping rate of 1.023 Mbps. Each satellite is assigned a unique C/A code, which is chosen from a family of Gold codes. Gold codes are obtained by modulo-2 addition of two maximum-length (m-sequence) sequences of equal period (in this case, 1023 bits). This C/A code is modulated by the navigation data bit sequence, which is transmitted at 50 bps. Since the C/A code is aligned with the navigation data bit boundaries at the time of transmission, there are exactly 20 C/A code periods within each data bit. The resulting signal is then used to modulate the L1 carrier for transmission. By assigning a unique C/A code for each satellite, the C/A-code cross-correlation properties enable all the satellites to share the same frequency band with limited interference. Thus, the GPS satellites use code division multiple access (CDMA) for transmitting the ranging signals. Minimum received power of the GPS L1 C/A signals listed in IS-GPS-200-D (2006) is -158.5 dBW (or -128.5 dBm). The minimum received power is defined as (IS-GPS-200-D 2006)

“the power measured at the output of a 3dB<sub>i</sub> linearly polarized user receiving antenna (located near ground) at worst normal orientation, when the satellite vehicle (SV) is above a 5-degree elevation angle”

The important factor contributing to power attenuation is the path loss as the signal travels approximately 20,000 to 25,000 km from the satellite to the user on the earth’s surface (Ray 2007). The path loss is calculated as

$$Path\ Loss = 10 \log_{10} \left( \frac{1}{4\pi d^2} \right) \text{ dB} \quad (2.1)$$

where  $d$  is the distance in metres. For GPS signals, the path loss is approximately -157 to -159 dB. Further, atmospheric losses may add up to 2 dB of signal attenuation (Ray 2007). For a satellite at the zenith transmitting the GPS signal at 14.3 dBW with 10.2 dB of satellite antenna gain, the received signal power per square metre is calculated as

$$\begin{aligned} Received\ Power &= 14.3 \text{ dBW} + 10.2 \text{ dB} - 157\text{dB} - 2 \text{ dB} \\ &= -134.5 \text{ dBW} \end{aligned} \quad (2.2)$$

## 2.2 Legacy GPS Receiver Architecture

With advances in technology, most modern day GPS receivers are digital. Figure 2-1 shows the block diagram of a generic digital GPS receiver. The following sections briefly describe each stage of the processing involved in a GPS receiver from signal reception to user position computation. The emphasis is placed on the limitations of the legacy GPS signal structure for signal tracking, which is a part of the signal processing block.

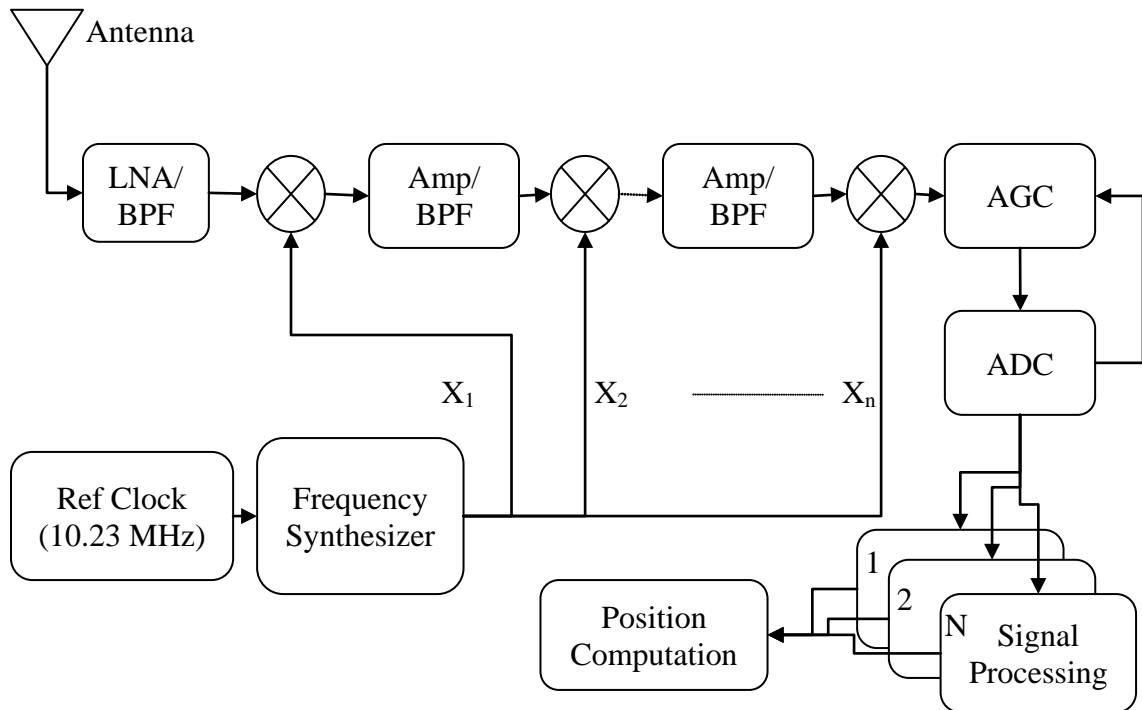


**Figure 2-1: Generic GPS receiver block diagram**

### 2.2.1 Antenna and Low-Noise Amplifier

The GPS signals of all satellite vehicles (SV) in view are received by a right hand circular polarized (RHCP) antenna. The GPS signals are RHCP on transmission and, hence, reflected signals are mostly left hand circular polarized (LHCP). However, the polarization of the reflected signal, as received at the antenna, depends on the reflecting surface and the number of reflections the signal underwent before reaching the receiver. Still, choosing an RHCP antenna helps to at least partially attenuate the reflected signals or multipath. The antenna gain pattern is nearly hemispherical with the main lobe pointing towards the sky. This helps in attenuating ground reflected signals. The antenna gain for signals at zenith is typically around 4-5 dBic (u-blox ANN-MS 2009, NovAtel

701G 2009). The antenna gain for signals gradually rolls off from the zenith to the horizon.

The power of the GPS signal received by an antenna on the ground is calculated as

$$\text{Effective Received Power} = \frac{\lambda_{L1}^2}{4\pi} \times \text{Received Power per sq.m} \quad (2.3)$$

where  $\frac{\lambda_{L1}^2}{4\pi}$  is the effective antenna area and  $\lambda_{L1}$  is the wavelength of the GPS L1 carrier signal. When the nominal received power per square metre calculated in Eq. (2.2) is applied to Eq. (2.3), the effective received power is approximately -160 dBW. This calculation applies for the L1 C/A signal transmitted by the older II, IIA and IIR satellites. The effective received power of the L1 C/A signal transmitted by modernized satellites (IIR-M and IIF) has been increased to -158.5 dBW (IS-GPS-200-D 2006).

Most GPS antenna assemblies house a low noise amplifier (LNA), which rejects out of band signals and provides sufficient gain for the GPS signals (typically around 27-29 dB). The noise figure (NF) of the LNA should be low (in the order of 1.5 – 2 dB) to reduce the effect of any further losses introduced by the components in the radio frequency (RF) chain that follows, e.g. cable losses, noise figure of other amplifiers, filters, etc. To stress the importance of the noise figure of the LNA in a receiver, a brief mathematical explanation is provided. The thermal noise spectral density ( $N_0$ ) of a receiver is given by

$$N_0 = k_B \times T_{sys} \quad (2.4)$$

where  $k_B$  is Boltzmann's constant (-228.6 dBW/kHz) and  $T_{sys}$  is the system noise temperature.  $T_{sys}$  is calculated as (Ray 2007)

$$T_{\text{sys}} = T_{\text{sky}} + T_{\text{R}} \quad (2.5)$$

where  $T_{\text{sky}}$  is the sky temperature (100 K) and  $T_{\text{R}}$  is the receiver temperature. The receiver temperature depends on the losses and gains introduced by each element in the RF chain.  $T_{\text{R}}$  is calculated using the Friis formula as

$$T_{\text{R}} = T_0 \left\{ [L_{\text{Ant/LNA}} - 1] + L_{\text{Ant/LNA}} [NF_{\text{LNA}} - 1] + L_{\text{Ant/LNA}} \left[ \frac{L_2 - 1}{G_{\text{LNA}}} \right] \right. \\ \left. + L_{\text{Ant/LNA}} L_2 \left[ \frac{NF_2 - 1}{G_{\text{LNA}}} \right] + L_{\text{Ant/LNA}} L_2 \left[ \frac{L_3 - 1}{G_1 G_2} \right] + \dots \right\} \quad (2.6)$$

where  $T_0$  is room temperature ( $\sim 290$  K),  $L_{\text{ANT/LNA}}$  is the loss introduced by the antenna and the LNA (often negligible, 0 dB),  $NF_{\text{LNA}}$  is the noise figure of the LNA,  $G_{\text{LNA}}$  is the gain of the LNA and  $\{NF_n, L_n, G_n\}$  are the noise figure, loss, and gain introduced by element  $n$  in the RF chain, where  $n$  indicates the sequential order of the element in the chain. As given by Eq.(2.6),  $NF_{\text{LNA}}$  is the only element that linearly contributes to  $T_{\text{R}}$  without any scaling. In other words, all other  $NF_n$  are scaled by the product of the gain of the previous elements, thus reducing their effect. This also makes the LNA gain ( $G_{\text{LNA}}$ ) another important factor to reduce the effect of  $NF_n$  on the following elements. In summary, the gain and noise figure of the LNA essentially determine the noise figure of the system.

### 2.2.2 Down Converters and Amplifiers

A stable fundamental clock ( $f_{\text{clk}}$ , typically 10.23 MHz) is used to generate the local frequencies. Mixers beat the incoming signal and the resulting lower sidebands are filtered for further amplification using band pass filters (BPF). This down-conversion can be done at multiple stages ( $X_1, X_2 \dots X_n$ ), where  $X_n = k_n f_{\text{clk}}$  is the frequency used by the  $n^{\text{th}}$  mixer. The scaling factor  $k_n$  depends on the receiver design. These multiples of the

fundamental clock frequency are generated by a frequency synthesizer, which uses a phase locked loop (PLL) to lock to the reference clock. The resulting IF frequency is given by  $(1575.42 - \sum_n X_n) \text{ Hz}$ . The net gain provided by the amplifiers in the RF chain is approximately 100 dB.

### **2.2.3 Automatic Gain Control (AGC) and Analog to Digital Converter (ADC)**

Most commercial receivers use 1-bit quantization or hard limiters (Van Dierendonck 1995). This implementation does not require an automatic gain control (AGC) but lacks the ability to provide a dynamic operating range due to gain variations and interference. Receivers that process multi-bit, quantized, GPS signals include an AGC towards the end of their RF chain. An AGC works along with the analog to digital converter (ADC) to maintain the signal level at a sufficient amplitude range for reliable quantization. Until this stage, the GPS signal is below the noise floor. For example, the nominal  $C/N_0$ , calculated as a ratio of Eq. (2.3) and (2.4), is approximately 42 dB-Hz. For a pre-correlation bandwidth (BW) of 2.5 MHz, which is wide enough for the main lobe of C/A code, the SNR of the signal is calculated as

$$SNR_{dB} = (C/N_0)_{dB-Hz} - 10 \log_{10}(BW_{Hz}) \quad (2.7)$$

which is approximately -22 dB. Thus, further processing is required to boost the signal power and this is done in the signal processing block.

### **2.2.4 Signal Processing Block**

The signal processing block has multiple channels with one for each SV in view. In each channel, the receiver initially attempts to obtain a rough estimate of the code phase delay and Doppler information. The code phase delay estimate is required to properly remove the spreading code modulation from the signal, as an offset of 1 chip or

more in the local code phase can lead to a total loss of signal power. The Doppler is due to the relative motion between the satellite and the user. This stage is called the signal acquisition stage.

Once the signal is acquired, the receiver has to track the signal continuously for changes due to satellite movement or user dynamics. The continuous tracking helps in the complete removal of the residual Doppler and phase (carrier and code phase) offsets. This is called the signal tracking stage. Signal tracking consists of carrier and code tracking. Carrier tracking estimates the residual carrier phase and frequency offset whereas code tracking estimates the residual code delay. These estimates are then applied as corrections to the respective local carrier and code generators. Carrier tracking is often described as the weaker link in signal tracking, as the thermal noise and dynamic stress have a more significant impact on the carrier phase. Hence, carrier tracking is of interest in this work and a more detailed introduction is provided below. Limitations on the performance of the carrier tracking algorithms due to the legacy GPS signal structure are included when appropriate.

Carrier tracking can be done with either a frequency or phase tracking loop. Carrier phase tracking is the preferred state in a GPS receiver as it provides more error free data extraction (or demodulation) when compared to frequency tracking (Kaplan 2006). The tracking algorithms start functioning after signal acquisition. Signal acquisition reduces the uncertainty in residual Doppler frequency to the size of a Doppler bin. Typically, a Doppler bin size of  $\left(\frac{2}{3T_{coh}}\right) Hz$  is used, where  $T_{coh}$  is the predetection interval (Van Dierendonck 1995). There is a need to quickly acquire the remaining

Doppler offset to enable phase tracking. Although phase tracking loops can close-in on the residual frequency offset in the incoming signal, they are relatively slow compared to carrier frequency loops. For example, with a second order PLL, the time taken for frequency acquisition is proportional to the square of the initial frequency error. When carrier frequency tracking is used, the pull-in time reduces to the logarithm of the initial frequency error (Gardner 2005). Normally, receivers are initialized with frequency and code tracking following signal acquisition. After frequency lock is attained, phase tracking is initiated (Kaplan 2006).

Figure 2-2 shows a generic block diagram of the carrier tracking loop. The pre-detection integrators ( $\Sigma_{T_{coh}}$ ), the discriminator and the loop filter (LF) characterize the tracking loop. The digitized incoming IF samples are subjected to IF and residual Doppler removal. The former is a known value whereas the latter is estimated continuously within the signal processing block. Then, the spreading code is removed by correlation with the output of a local code generator.

The Doppler-removed and despreaded samples are then accumulated over a period of time, which is referred to as the predetection interval ( $T_{coh}$ ). If the noise corrupting the IF samples is assumed to be additive white Gaussian noise (AWGN), then coherent accumulation of correlator outputs over  $T_{coh}$  provides a SNR gain of

$$Gain (dB) = 10 \log_{10}(BW \times T_{coh}) \quad (2.8)$$

This corresponds to a gain of 34 dB with 1 ms of averaging and 2.5 MHz of pre-correlation bandwidth (BW). Continuing from the example in Section 2.2.3, the signal at an SNR of -22 dB receives 34 dB of gain after a coherent integration of 1 ms. Thus

coherent integration effectively aids in bringing the signal power out of the noise floor for the proper operation of the tracking algorithms.

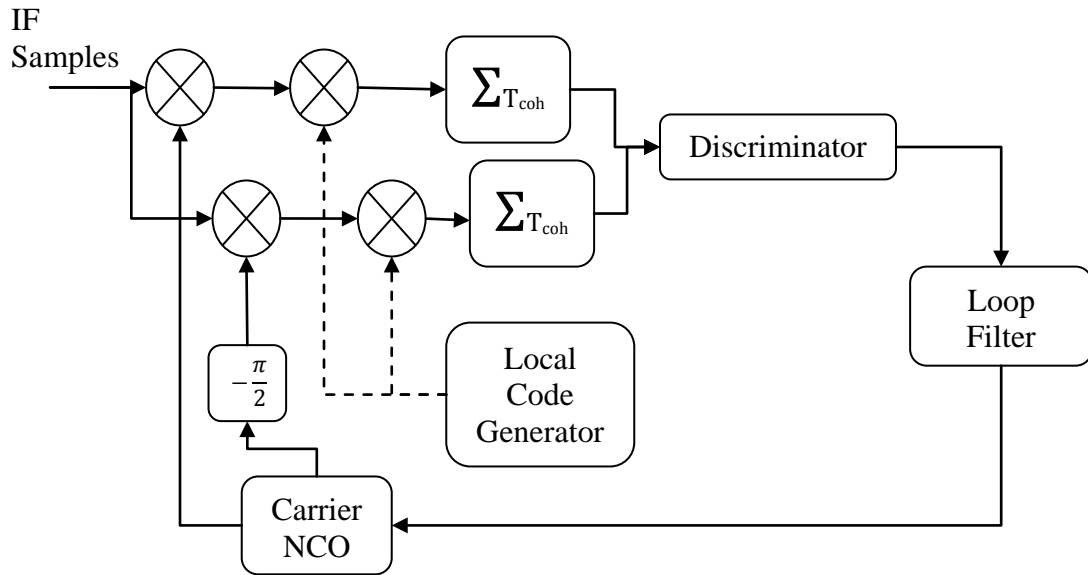


**Figure 2-2: Carrier tracking loop block diagram**

The following limitations are encountered when increasing the gain described in Eq. (2.8):

*Limitation 1:* Although Eq. (2.8) suggests that a longer predetection interval results in a higher gain, the presence of unknown data bits in the incoming signal limits the length of averaging. Hence,  $T_{coh}$  cannot be extended beyond 10 ms without knowledge of the data bit boundary for single point positioning (Akos 2000). If the data bit boundaries are known, i.e. the samples at which the data bit sign changes are known, then the coherent integration can be done over the entire length of the data bit period. In this case, this limits the predetection interval to 20 ms for the GPS L1 C/A signal.

*Limitation 2:* Acquisition provides a coarse estimate of the code phase within a C/A code period. However, since there are 20 C/A code repetitions within each data bit, a

separate bit synchronization algorithm is required to find the 1 ms epoch in which the data bit transition occurs. This bit synchronization stage adds overhead to the processing. The performance of the histogram method for bit synchronization used in most receivers degrades at low  $C/N_0$ . This further complicates the problem of weak signal tracking (Van Dierendonck 1995, Anghileri et al 2006).

The accumulated correlator outputs are then fed to the phase or frequency error estimators, which are referred to as discriminators. The phase-error discriminator is used for carrier-phase tracking and the frequency-error discriminator for carrier-frequency tracking. The effect of the data bit on the accumulated correlator outputs needs to be accounted for while estimating the phase or frequency error. The reliable operating range of the frequency discriminators is defined as the range over which the estimated frequency error is approximately equal to the original frequency error.

*Limitation 3:* The reliable operating range of the frequency discriminators, which account for the data bit presence, is one half of that of the discriminators that operate on a channel without data bit modulation (pilot).

For carrier-phase tracking, the tracking loop architecture which makes use of discriminators that account for the data bit presence is called the Costas loop architecture. A pure PLL discriminator can be used only if there is no data modulation in the signal. A pure PLL discriminator (ATAN2 – four quadrant arctangent) has a wider linear region (phase pull-in range) of  $\pm\pi$  radians and improves the signal tracking threshold by up to 6 dB as compared to the Costas loop (Kaplan 2006). The signal tracking threshold is defined as the minimum signal power required to maintain the  $3\sigma$  jitter within one-fourth of the phase pull-in range of the discriminator in use.

*Limitation 4:* The presence of the data bit prevents the usage of the pure PLL for carrier-phase tracking. Thus the advantages such as increased pull-in range and improved signal tracking threshold are lost.

*Limitation 5:* The use of the Costas loop introduces a  $\pm\pi$  ambiguity in phase tracking, which necessitates a preamble (known sequence of data bits) in the data bit train transmitted to aid in resolving the ambiguity.

The discriminator output is passed through a loop filter (LF) before the correction is applied to the local carrier generator, i.e. numerically controlled oscillator (NCO) in Figure 2-2. Apart from reducing noise, the LF plays an important role in determining the response of a tracking loop to different conditions. For example, a second order tracking loop is sensitive to acceleration stress (non-zero steady state error) whereas a third order loop can zero the acceleration error as it approaches the steady state (Gardner 2005). The local carrier generator includes the correction from the LF for phase or frequency errors while generating the reference signal for the next epoch.

### **2.2.5 User Position Computation**

Once carrier and code tracking are achieved, data bit synchronization is performed to detect the data bit boundaries. The data bits are then extracted. The preamble needs to be detected to find the start of a sub frame. Then the received data bits are arranged in the sub-frames from which the Z-Count information is extracted. Z-Count gives the time of transmission of the next sub-frame from that particular SV. Pseudoranges are calculated for every SV tracked at the same measurement time using their respective Z-Count and the receiver time. Pseudoranges measured across all the SVs in view are then used to compute the user position and the receiver time offset.

### **2.3 Limitations of the Legacy GPS Signal**

The L1 C/A signal structure design was originally intended for line-of-sight (LOS) positioning and as an acquisition aid to the military code. But with the growing integration of GPS modules in numerous civilian devices, the need for reliable and accurate positioning in challenging environments needs to be addressed. Challenging environments include areas with heavy signal attenuation (20-30 dB), blockage, intentional or unintentional interference, and reflected signals (multipath).

The focus of this thesis is on signal tracking for attenuated signals; hence it is described herein. The GPS signal experiences heavy attenuation as it passes through building walls and, as a consequence, the received signal power drops to as low as -200 dBW (Dedes & Dempster 2005) or lower. The limitations discussed in Section 2.2.4 make carrier tracking of the legacy GPS signals more challenging under such environments. The presence of data bits is one of the major factors which directly or indirectly cause the above limitations. Although data bits can be stripped off with the help of external aiding or with a reference antenna tracking stronger signals, these options are clearly not applicable to real-life situations (Haddrell & Pratt 2001). Tuning the standard receiver architecture to cope with the aforementioned limitations is an active field of research. Still, a change in the structure of the transmitted signal with the knowledge gained from the L1 C/A signal may effectively address current limitations as well as future demands from civilian users.

### **2.4 GPS L2-Civilian (L2C) signal**

The current GPS satellite constellation is being modernized at L2 (1227.6) and L5 (1176.45 MHz) frequencies to overcome the limitations of the legacy GPS L1 C/A signal.

The civilian signal on L2 (L2C) is targeted at the existing community of dual frequency users and future L2-only single frequency users (Fontana et al 2001). The L5 signal is mainly intended for safety-of-life applications including aviation (Tran & Hegarty 2003). The most distinguishable change incorporated in the signal structure of these modernized signals, as compared to the legacy L1 C/A signal, is the inclusion of a dataless channel (pilot channel) in addition to the navigation data channel. This assists in weak signal tracking. The available transmission power is equally shared between the data and pilot channels. This sharing results in a 3 dB lower signal power on each individual channel. Still, the ability to use a PLL to track the pilot channel provides a gain of 6 dB in tracking threshold, which enables L2 signal tracking at a 3 dB lower strength than the legacy L1 C/A signal (Kaplan 2006). Since September 2005, the constellation is being modernized with IIR-M satellites capable of transmitting the L2C signal. The L2C signal will also be transmitted on future Block IIF and III satellites along with the other modernized signals. The availability of live L2C signals facilitates the option to evaluate the advantages gained by the presence of both the data and pilot signals from each SV.

In this thesis, the L2C signal is used as a tool to validate and analyse the algorithms proposed to use either the data or pilot channel independently (or together) for carrier tracking and  $C/N_0$  estimation. The following sections give a brief introduction to the L2C signal structure and the receiver design changes required. For notational clarification, the term “channel” is often used in the literature to refer to a module that tracks the signal from a particular SV. Owing to the difficulty in extending this terminology for modernized signals due to the presence of a data and pilot signal from every SV, the term “data channel” herein refers to the channel in the receiver that tracks

the data signal and similarly the term “pilot channel” refers to the channel tracking the pilot signal.

### 2.4.1 L2C Signal Structure

The civilian signal on the L2 band is transmitted in phase quadrature to the military signal P(Y) on the same carrier frequency (Fontana et al 2001). The L2C signal carries two codes, the civil-moderate (CM) and civil-long (CL) codes. The CM code for each SV is 20 ms in length with a chipping rate of 511.5 Kbps (10230 chips). The CL code is 75 times longer than the CM code (767250 chips) with the same chipping rate (period = 1.5 s). The CM code is modulated by the navigation data whereas the CL code is not. Thus the former serves as the data channel and the latter as the pilot channel. Since both the data and pilot channels must be transmitted on a single carrier component, they are time-multiplexed on transmission, as shown in Figure 2-3. Thus the effective chipping rate of the time multiplexed code is 1.023 MHz, which is the same as the C/A code chipping rate. The CM code is aligned with the data bit boundaries, thus eliminating the need for a bit synchronization algorithm once signal acquisition is achieved.

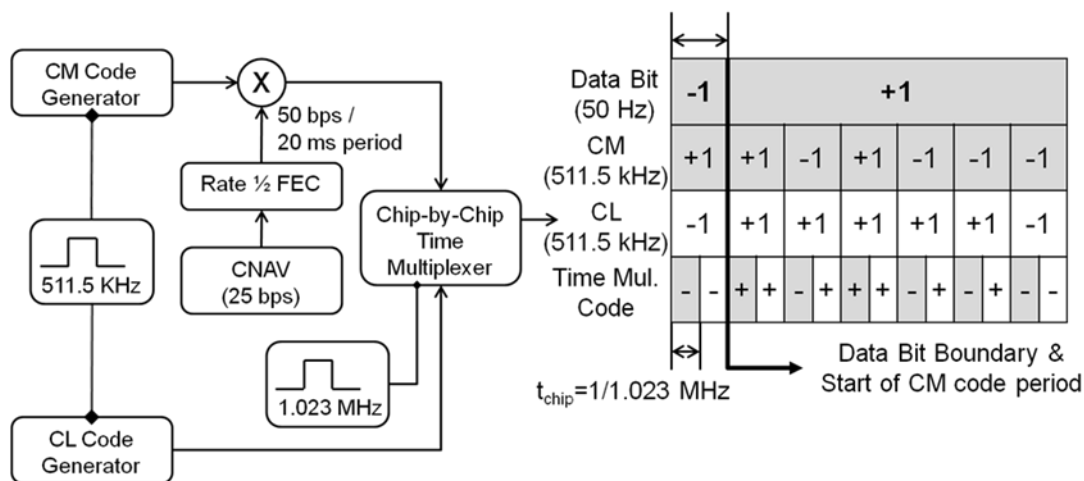


Figure 2-3: Time multiplexed data and pilot channel generation

The CM and CL codes for all the SVs are generated using a 27 bit linear feedback shift register (LFSR) with fixed taps. The generator polynomial is given as

$$G(x) = 1 + x^3 + x^4 + x^5 + x^6 + x^9 + x^{11} + x^{13} + x^{16} + x^{19} + x^{21} + x^{24} + x^{27} \quad (2.9)$$

When allowed to run continuously, the LFSR described by Eq. (2.9) generates a m-sequence with a period of  $2^{27}-1$  chips. However for CM and CL code generation, the LFSR is short cycled to 10230 and 762750 chips, respectively. Distinct initial states of the LFSR generate different subsets of the original long-length m-sequence. The initial and final states of the LFSR corresponding to each SV are given in IS-GPS-200-D (2006). All the subset codes are chosen to be perfectly balanced, i.e. they have equal numbers of 1s and 0s (Fontana et al 2001). There are exactly 75 periods of CM code within each CL code and the CL code is synchronized with the Z-Count (1.5 s).

The CM code is modulated with the civil navigation (CNAV) data. The CNAV data differs from the original navigation data (NAV) carried by the L1 C/A signal, as it includes new parameters for SV ephemerides that improve the accuracy of the satellite position determination and also has a flexible structure for frames (Mongrédien 2008). The CNAV data bit rate is originally 25 bps. It is coded by a rate  $\frac{1}{2}$  convolutional encoder which yields a 50 sps symbol stream. Convolutional coding helps to reduce the bit error rate during data bit extraction in the receiver. Although the CNAV modulation on the CM code is the intended design for the data channel, any of the following combinations can be broadcasted on the data channel during the initial phases of the IIR-M satellites (IS-GPS-200-D 2006):

- i. NAV data as on L1 C/A at 50 bps modulated on CM code
- ii. NAV data with rate  $\frac{1}{2}$  convolutional encoder modulated on CM code

- iii. NAV data modulated on C/A code
- iv. C/A code without data modulations
- v. CM code without data modulations
- vi. CNAV at 50 bps modulated on CM code

#### **2.4.2 Limitations of L2C signal**

As compared to the legacy L1 C/A signal, the following are considered the limitations or shortcomings of using a single frequency L2C receiver:

- i. The minimum received signal power of the L2C signals is 1.5 dB lower than that of the L1 C/A signals (IS-GPS-200-D 2006). However, the addition of the pilot channel and the longer length codes compensates for the difference in signal power.
- ii. The error introduced by the ionosphere is inversely proportional to the square of the carrier frequency. The L2 carrier is transmitted approximately 347 MHz lower than the L1 carrier frequency and thus has 65% more ionospheric refraction error (Fontana et al 2001). A L1/L2 dual frequency receiver can effectively remove the ionospheric error by up to 99% of the total delay (Skone 2005).

Although a single frequency L2C receiver can be considered a robust alternative to the L1 C/A only receiver, due to the complementary signal properties of L2C, a dual frequency receiver using both civilian signals (L1 C/A and L2C) will be advantageous compared to a receiver using individual signals (Gernot et al 2008, Gernot et al 2007). Since the focus of this thesis is on evaluating the advantages of the pilot channel

availability in addition to the data channel for signal tracking, dual frequency processing is not considered in this thesis.

## **2.5 L2C Software Receiver**

Hardware implementation of the GPS receiver is a feasible solution for commercial products when the algorithms used within the receiver are finalized. For research and analysis purposes however, software implementation of the signal processing algorithms allows flexibility and minimizes cost. Software receivers have received much interest in the past few years (Shanmugam 2008, Mongrédien 2008, Ledvina et al 2004, Abbasiannik 2009, Petovello et al 2008 etc.).

In software receivers, the down converted and digitized signal is acquired as a binary bit stream and the entire baseband signal processing (correlation, acquisition, tracking and position computation) is carried out in the post processing stage. This allows for the analysis of the performance of different algorithms with a data set collected in a given scenario.

The global navigation satellite system (GNSS) software navigation receiver (GSNRx<sup>TM</sup>) is a Visual C++ based software receiver developed by the PLAN group at the University of Calgary (Petovello et al 2008). This software receiver, which was initially capable of tracking GPS L1 C/A signal only, was modified by the author to track L2C signals. The following sections describe the L2C specific changes included in the software receiver.

### **2.5.1 Local Code Generation**

As described in Section 2.4.1, the incoming L2C signal carries time multiplexed spreading codes. It is not desirable to use an exact replica of the time-multiplexed version

for the local code generation to acquire the signal due to the presence of data modulation on the CM code (Tran & Hegarty 2002). Hence the local code generation must be appropriately modified. Different methods for local code generation have been suggested in Tran & Hegarty (2003). They are:

- i. The local CM code generator is clocked at its original chipping rate of 511.5 kHz while acquiring or tracking the data channel and, similarly, the pilot channel. This implementation introduces the CM-CL cross-correlation noise in addition to the thermal noise and also flattens the autocorrelation peak (Dempster 2006), thus making acquisition and tracking vulnerable to multipath.
- ii. A zero-padded version of the code is used to acquire or track. For CM code acquisition, the CL segments are replaced with 0s, as shown in Figure 2-4. This option requires the return-to-zero form of the local code, which has three states (+1, -1, and 0) that cannot be applied directly to a simple XOR gate for hardware implementation. The number of code bins during acquisition would also double by using a zero padded version. The length of each CM code is 10230 chips. For a code search step of  $\frac{1}{2}$  chip, the number of code bins to search for is 20460 for the previous implementation (CM code clocked at 511.5 kHz) to ensure a maximum of 25% power loss due to code misalignment. When using a zero-padded CM code, the local code length is doubled to 20460 chips and hence the number of code bins to search is also doubled. Similarly, for the CL code, the CM code segments are replaced with zeros.

As described above, both implementations incur a 3 dB loss of power since one channel is completely unused while processing the other. The latter option has an advantage over the former one, as it reduces the CM-CL cross correlation noise. The zero-padded versions of the CM and CL codes are used in this work.

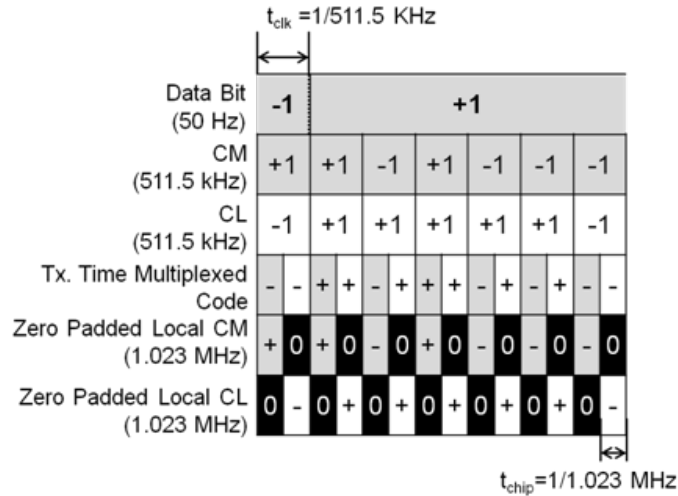


**Figure 2-4: Zero padded local code generation for L2C signals**

### 2.5.2 L2C Acquisition

L2C acquisition starts with the CM code acquisition owing to the length of the CL code. First,  $(20 \text{ ms} \times m \times f_s)$  samples from the digitized and down-converted data is read from the data file, where  $m$  is the number of non-coherent summations required and  $f_s$  is the sampling rate. The zero-padded CM code is generated and sampled at  $f_s$ . This is then used to perform non-coherent acquisition with a fixed coherent integration period of 20 ms. The number of non-coherent summations ( $m$ ) is varied depending on the strength of the incoming signal. When a peak is not detected, the input binary stream is read with a 1 ms offset ( $1 \text{ ms} \times f_s$  sample offset) and acquisition is reattempted. The offset is increased in multiples of 1 ms until a peak is detected. This helps in accounting for data

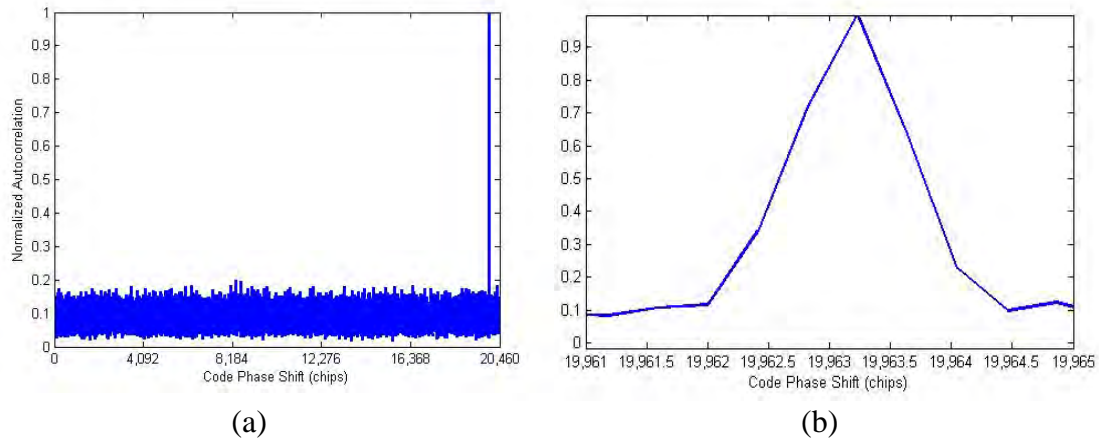
bit transitions. Although this manner of CM acquisition is not a refined or preferred method, it is applied for the current research since the acquisition is done in post-processing where the computational power or timing requirements are not as stringent as they would be in a hardware or real-time software receiver. Once the CM code acquisition is complete, due to the CM-CL code synchronization, the search for the CL code is restricted to only 75 different segments of the CL code corresponding to that CM code interval.

In cold start, once the CL code is ‘correctly’ acquired for a given SV at the  $n^{\text{th}}$  segment, where  $1 \leq n \leq 75$ , it is sufficient to search over only  $(n - 1, n, n + 1)$  CL segments for the other SVs that are in view. This is based on the fact that the maximum difference in range between two SVs will not be more than about 5044 km with  $\theta_e = 5^\circ \rightarrow 90^\circ$ , where  $\theta_e$  is the elevation angle of the satellite with respect to the receiver antenna (Ray 2007). This range difference maps to about 17,211 chips in length at a chipping rate of 1.023 MHz, which is less than the zero-padded CM code period (20460 chips). This difference is used as an empirical test for possible false CL acquisition and hence no statistical proof is provided.

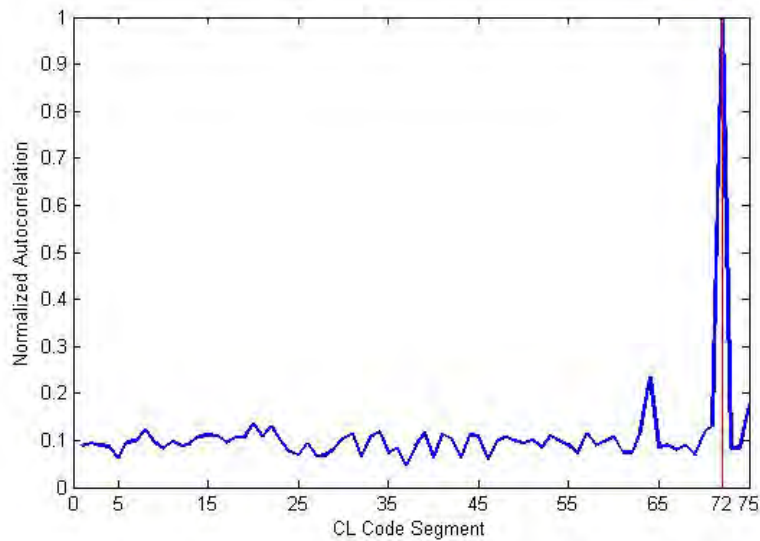
Figure 2-5 shows a plot of the normalized autocorrelation values for a carrier Doppler shift of -350 Hz for the CM code acquisition of PRN 15. PRN 15/SVN 55 is one of the IIR-M satellites transmitting the L2C signal.

Figure 2-6 shows the normalized correlation values corresponding to 75 different CL code segments computed with the aid of the CM code acquisition results. The segment number corresponding to the peak (shown by the red line in Figure 2-6) is then

used along with the CM code phase (corresponding to the peak in Figure 2-5 b) to compute the corresponding CL code phase for tracking.



**Figure 2-5: CM code acquisition for PRN 15 (live data) (a) Normalized autocorrelation values across all code phase shifts for a Doppler of -350 Hz (b) Zoomed in view of autocorrelation peak**



**Figure 2-6: Normalized correlation plot for 75 different segments of CL code for PRN 15**

### 2.5.3 L2C Tracking

The tracking loop shown in Figure 2-2 applies to the tracking of the L2C signal except for the following differences:

- i. two such tracking modules or loops are required for every SV, one to track the data channel and the other for the pilot channel;
- ii. the local code generator is modified to generate the respective zero-padded codes as described in Section 2.5.1; and
- iii. the local carrier NCO is modified to generate the IF and Doppler corresponding to the L2 signal.

There are other options to track the L2C signal. One of the two channels (data or pilot) can be used to derive the tracking error estimates and the error can be fed to both channels. For this architecture, utilizing the pilot channel to derive the tracking error estimates will be advantageous owing to the advantages in overcoming the limitations discussed in Section 2.3 (Ries et al 2002, Macabiau et al 2003). However, using single channel information to track both data and pilot channels is not optimum since one of the channels is not used.

The following chapters discuss in detail the different carrier frequency and phase tracking algorithms that can make use of both the data and pilot channels. Since the focus of this thesis is on the carrier tracking algorithms, the implementation changes with respect to the code tracking algorithm is only mentioned when necessary. Unless otherwise mentioned, the code tracking follows the standard architecture given by Van Dierendonck (1995) and Kaplan (2006).

### **CHAPTER THREE: THEORETICAL BOUNDS AND RELIABLE $C/N_0$ ESTIMATION FOR MODERNIZED GNSS SIGNALS**

To accomplish joint data/pilot weak GPS signal tracking, it is important to have a reliable method for estimating the carrier-to-noise density ratio ( $C/N_0$ ), which will be used to quantify the performance of the proposed tracking algorithms. This chapter provides a comprehensive theoretical analysis of the  $C/N_0$  estimation process with emphasis on the use of both data and pilot channels as input. The following are considered contributions of this thesis towards  $C/N_0$  estimation for modernized GNSS signals:

- i. The derivation of a theoretical bound on the gain achievable by using both the data and pilot channels for  $C/N_0$  estimation, and the use of this bound to analyse the performance of  $C/N_0$  estimators;
- ii. The analysis of the effect of the predetection interval on  $C/N_0$  estimates;
- iii. Maximum-likelihood (ML) estimators that use either the data channel alone or both the data and pilot channels are derived with detailed analysis of the bias levels and noise variance under weak signal conditions;
- iv. A novel iterative method for  $C/N_0$  estimation, proposed first for the data channel only, and then extended to use both channels. The proposed method has been shown to be reliable down to a  $C/N_0$  of 17 dB-Hz when applied to GPS L2C signals. Further, the algorithm provides a less noisy estimator (with lower variance) as compared to using the pilot channel alone.

### 3.1 Introduction

Carrier-to-noise density ( $C/N_0$ ) estimates are considered the most important quality control parameter in GNSS receivers (Kaplan 2006). Apart from its role as a significant parameter to accept or reject satellite observations in the position solution, accurate  $C/N_0$  estimation is also required for:

- i. quantifying the performance of algorithms proposed for weak GNSS signals. Most weak GPS signal tracking algorithms found in the literature are analyzed based on their ability to track signals against the  $C/N_0$  levels measured at the receiver end (Kazemi & O'Driscoll 2008, Lashley & Bevely 2008 etc.);
- ii. algorithms that use  $C/N_0$  estimates as a measure of thermal noise. This includes Kalman filter (KF) based tracking algorithms, which use  $C/N_0$  estimates as a measure of the noise in the accumulated correlator outputs and adaptive noise bandwidth tuning in phase locked loops, which helps in choosing an optimum bandwidth depending on the environment of the receiver (Psiaki & Jung 2002, Petovello & Lachapelle 2006, Mongrédien et al 2007, Muthuraman et al 2008 etc.).

Although several algorithms are used for  $C/N_0$  estimation, the theoretical analysis of the  $C/N_0$  estimation process has been only marginally developed in the GNSS context. The most widely used  $C/N_0$  estimator, which is referred to here as the standard estimator (SE), relies on the computation of the narrow band power (NBP) versus wide band power (WBP) ratio (Van Dierendonck 1995). The SE uses 1 ms accumulated correlator

(complex) outputs to compute the narrow band power over the data bit period of 20 ms (assuming known bit boundary) as

$$NBP_m = \left( \sum_{k=1}^{K=20} I_k \right)_m^2 + \left( \sum_{i=1}^{K=20} Q_k \right)_m^2 \quad (3.1)$$

where  $NBP_m$  is the narrow band power computed over the  $m$ -th data bit period,  $K$  is the number of observations per data bit interval, and  $Y_k = I_k + j Q_k$  represents the 1 ms accumulated correlator outputs. Similarly, the wide band power is calculated as the sum of square of 1 ms outputs as

$$WBP_m = \left( \sum_{k=1}^{K=20} (I_k^2 + Q_k^2) \right)_m \quad (3.2)$$

The ratio  $NP_m$  is computed as

$$NP_m = \frac{NBP_m}{WBP_m} \quad (3.3)$$

The mean of this ratio ( $\mu_{NP}$ ) is given as

$$\mu_{NP} = \frac{1}{M} \sum_{m=1}^M NP_m \quad (3.4)$$

where  $M$  is the number of data bit periods over which the averaging is done. The ratio  $\mu_{NP}$  is a function that monotonically increases with respect to  $C/N_0$ . Thus,  $C/N_0$  can be uniquely estimated by inverting this function. Input blocks of 1 ms, which is the most common configuration, are chosen for ease of implementation in the GPS L1 C/A case (C/A code period = 1 ms). In Figure 3-1, the SE is used for estimating the  $C/N_0$  of a progressively attenuated signal generated using a Spirent GPS hardware simulator. More specifically, the mean and standard deviation of the simulated attenuation, with respect to

a 32 dB-Hz reference level, are shown. Beyond 9 dB of attenuation ( $C/N_0$  of 23 dB-Hz and lower), the SE fails considerably in terms of bias in the estimate and is, therefore, not reliable for weak signals.

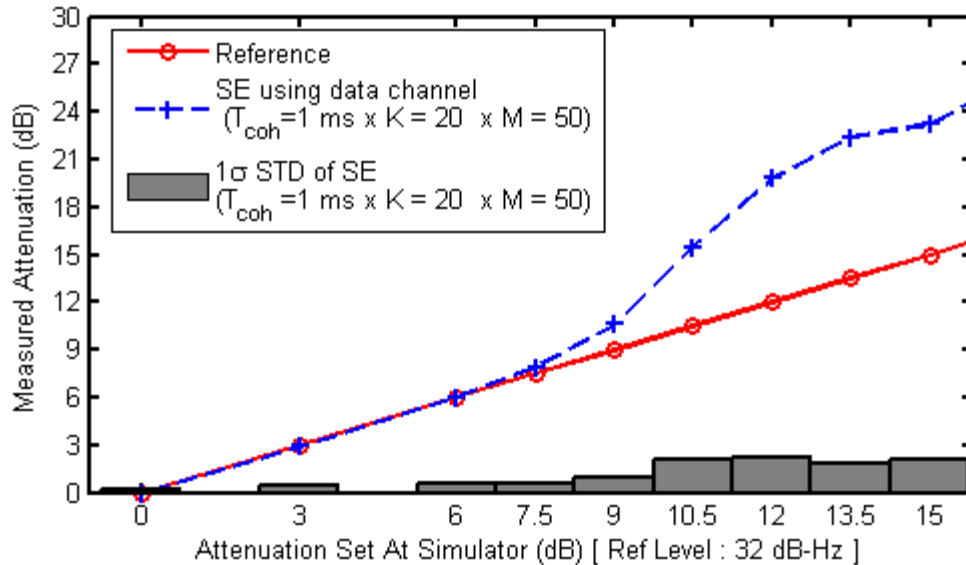


**Figure 3-1: Analysis of the reliability of the standard  $C/N_0$  estimator (averaged across 6 satellites)**

Under such scenarios,  $C/N_0$  estimation can also benefit from the availability of the pilot channel usually present in modernized GNSS signals. For instance, the Cramer-Rao lower bound (CRLB) for the  $C/N_0$  estimation using pilot channel observations is found to be lower than that using data channel observations (Alagha 2001). Rather than evaluating the bias and variance of the SE using pilot channel observations and  $K$  greater than 20, this chapter takes a different approach towards the problem of  $C/N_0$  estimation. The following approach is adopted:

- i. Definition of performance bounds (CRLB) of  $C/N_0$  estimation using either the data or pilot channel and for the joint data/pilot case;

- ii. Theoretical bound on the performance gain achievable by using both the data and pilot channels will be provided;
- iii. Analysis of the effect of the predetection interval ( $T_{coh}$ ) used for  $C/N_0$  estimation on the performance bounds and optimum choice of  $T_{coh}$  to be used with  $C/N_0$  estimators;
- iv. Derivation of approximated ML estimators for  $C/N_0$  for single channels (either data or pilot) and for the joint data/pilot case. Bias and variance analysis of derived estimators.
- v. Iterative solution for joint data/pilot  $C/N_0$  estimation, to account for the nonlinearity, and verification of its reliability for weak signals in the case of the GPS L2C signals.

Although the problem of  $C/N_0$  estimation can be viewed as a scaled signal-to-noise ratio (SNR) estimation and theoretical analysis for SNR estimation is widely available in the communications context (Pauluzzi & Beaulieu 2000), a detailed analysis in the specific context of GNSS signals is still missing in the literature. A comprehensive review of work, available in the literature, related to SNR estimation is provided in the following paragraph.

The CRLB for SNR estimation using pilot symbols alone, with the amplitude and noise variance as unknown parameters, is commonly available in the literature (Kay 1993). Alagha (2001) provides the CRLB using data channel observations and compares it with the estimation process which uses pilot channel observations. The assumptions used in the derivations and results presented by Alagha (2001) include one observation per data bit and equally probable data bits. This was extended to the use of  $N$  data

symbols and  $M$  pilot symbols by Chen & Beaulieu (2005). The latter also propose an approximate maximum-likelihood (ML) estimator for similar input conditions. Further, it is clearly stated that, although the amplitude estimator, which uses both data and pilot inputs, can be viewed as a linear combination of independent amplitude estimators on each channel, the optimal SNR estimator using both channels is a nonlinear combination of the individual SNR estimators. Here again, one observation per data bit was assumed and the results were analyzed using the noise variance at the estimation output. But the approximation used in deriving the ML estimator fails at low SNR, thus leading to biased SNR estimates. Li et al (2002) proposes an iterative search algorithm for the amplitude estimate on the data channel, which tries to solve the ML equation by searching through the values within a given range of normalized amplitudes. As mentioned before, although the above work provides an intuitive insight into the performance of  $C/N_0$  estimation, an analysis of theoretical bounds and achievable performance (in terms of bias and variance) specific to the context of GNSS signals is required.

Ramasubramanian & Nadig (2006) address the theoretical analysis by giving the CRLB for  $C/N_0$  estimation in GPS receivers for one particular case where 1 ms accumulated correlator outputs (20 observations per data bit) from the data channel (GPS L1 C/A) were used. Apart from this,  $C/N_0$  estimators derived with an analytical approach can be found in Groves (2005), Schmid & Neubauer (2005), Pany & Eissfeller (2006) and Muthuraman et al (2008). These approaches make use of the statistics of the accumulated correlator outputs to derive the estimator.

### 3.2 Signal Model

The received GPS signal after code and carrier removal is accumulated coherently on early, prompt and late channels for  $T_{coh}$  seconds. The accumulated correlator output on the prompt channel is the input (observation) to the  $C/N_0$  estimator.

Let  $N$  be the total number of observations to be used per  $C/N_0$  update per channel (either data or pilot). With the assumption of perfect code and carrier lock, this section provides the model and the probability density function used for data and pilot channel observations and the model used for  $C/N_0$  estimation.

#### 3.2.1 Data Channel Observations

For the case of the data channel, the data bit boundaries are assumed to be known or detected before  $C/N_0$  estimation starts. This is often easily achieved with modernized GPS signals, since the code period on the data channel is the same as the data bit period and their boundaries are aligned. The accumulated correlator output vector on the data channel ( $\mathbf{x}_D$ ) is given as

$$\mathbf{x}_D = \left[ \begin{array}{c} \overbrace{x_{1,1} \dots x_{1,K}}^{x_1} \quad \dots \quad \overbrace{x_{M,1} \dots x_{M,K}}^{x_M} \\ x_1 \rightarrow x_N \end{array} \right]^T \quad (3.5)$$

where observations are taken over  $M$  data bit intervals, with  $K$  observations per data bit period ( $M \times K = N$  observations). The parameter  $x_{m,k}$  denotes the  $k$ -th accumulated correlator output belonging to the  $m$ -th data bit. The parameter  $\mathbf{x}'_m$  is used to denote the set of observations belonging to the  $m$ -th data bit. Let  $x_n$  denote the individual observations within the set before grouping them based on the data bit, where  $n = (m - 1)K + k \ \forall (1 \leq n \leq N, 1 \leq m \leq M, 1 \leq k \leq K)$ .

Then

$$x_n = d_m A + w_{nd} \quad (3.6)$$

where  $d_m$  is the  $m$ -th data bit which takes a value in the set  $\{+1, -1\}$  with equal probability. Parameter  $A$  is the signal amplitude ( $A \geq 0$ ) and  $w_{nd}$  is zero mean AWGN noise with variance  $\sigma_n^2$ .

The vector of unknown parameters is given by  $\boldsymbol{\theta} = [A \quad \sigma_n^2]^T$ . The probability density function for the data channel observations belonging to the  $m$ -th data bit is given by

$$p(\mathbf{x}'_m; \boldsymbol{\theta}) = \frac{1}{(2\pi\sigma_n^2)^{\frac{K}{2}}} \exp\left(-\frac{1}{2\sigma_n^2} \left\{ \sum_k x_{m,k}^2 + A^2 \right\}\right) \cosh\left(\frac{A}{\sigma_n^2} \sum_k x_{m,k}\right). \quad (3.7)$$

Thus the joint pdf of  $\mathbf{x}_D$  is given as

$$p(\mathbf{x}_D; \boldsymbol{\theta}) = \prod_m p(\mathbf{x}'_m; \boldsymbol{\theta}). \quad (3.8)$$

### 3.2.2 Pilot Channel Observations

The observation vector for the pilot channel ( $\mathbf{x}_P$ ) need not be grouped as in  $\mathbf{x}_D$  due to the absence of data bits and is given as

$$\mathbf{x}_P = [x_{N+1} \quad \dots \quad x_{2N}]^T \quad (3.9)$$

where

$$x_n = A + w_{np} \quad (3.10)$$

for  $N + 1 \leq n \leq 2N$ , where  $w_{np}$  is the AWGN noise on the pilot channel accumulated correlator outputs characterized by the same distribution as  $w_{nd}$ . A shifted index ( $N + 1 \rightarrow 2N$  instead of  $1 \rightarrow N$ ) is used for the pilot channel for notational convenience. The pdf of  $\mathbf{x}_P$  is given by

$$p(\mathbf{x}_P; \boldsymbol{\theta}) = \prod_{n=N+1}^{2N} p(x_n; \boldsymbol{\theta}) \quad (3.11)$$

where  $p(x_n; \boldsymbol{\theta})$  denotes the pdf of individual pilot channel observations following a Gaussian distribution,  $\mathcal{N}(A, \sigma_n^2)$ .

Further, the cross correlation between the noise corrupting the data and pilot channel accumulated correlator outputs is assumed to be zero, as discussed in Chapter 2:

$$E[w_{np} w_{nd}] = 0 \quad \forall n. \quad (3.12)$$

### 3.2.3 C/N<sub>0</sub> Estimation Model

The C/N<sub>0</sub> expressed in units of *dB – Hz* is related to the post correlation SNR ( $\alpha$ ) as (Kaplan 2006)

$$\left(\frac{C}{N_0}\right)_{dB-Hz} = 10 \log_{10} \left(\frac{A^2}{2\sigma_n^2}\right) - 10 \log_{10} \left(\frac{T_{coh}}{2}\right). \quad (3.13)$$

Since  $T_{coh}$  is a known constant, the variance bound for C/N<sub>0</sub> estimation is given by that of the post correlation SNR term expressed in dB ( $\alpha = \frac{A^2}{2\sigma_n^2}$ ). Thus, it is required to evaluate the CRLB of a function of  $\boldsymbol{\theta}$ , given by  $g(\boldsymbol{\theta})$  as

$$g(\boldsymbol{\theta}) = 10 \log_{10} \left(\frac{A^2}{2\sigma_n^2}\right) = 10 \log_{10}(\alpha). \quad (3.14)$$

### 3.3 CRLB for C/N<sub>0</sub> estimation

In this section, the CRLB for C/N<sub>0</sub> estimation is derived, initially using either the pilot or data channel observations only and then for the joint data/pilot case. A detailed analysis of the results obtained is provided to make intuitive interpretations for practical scenarios.

### 3.3.1 Case – 1: Pilot Channel

When observations from the pilot channel alone are used for  $C/N_0$  estimation, the problem of deriving a bound reduces to the simple SNR estimation analyzed in the standard literature (Kay 1993). For this case, the Fisher information matrix ( $I_p(\boldsymbol{\theta})$ ) is given by

$$I_p(\boldsymbol{\theta}) = \begin{bmatrix} \frac{N}{\sigma_n^2} & 0 \\ 0 & \frac{N}{2\sigma_n^4} \end{bmatrix} \quad (3.15)$$

and thus the CRLB for  $C/N_0$  estimation is given by (Alagha 2001)

$$CRLB_p(g(\boldsymbol{\theta})) = \frac{200}{N(\ln 10)^2} \left( \frac{1}{\alpha} + 1 \right) [dB^2]. \quad (3.16)$$

### 3.3.2 Case – 2: Data Channel

The CRLB bound provided by Ramasubramanian & Nadig (2006) is specific to the case of  $K = 20$ ,  $T_{coh} = 1$  ms. Since one objective of this work is to analyse the effect of the predetection interval ( $T_{coh}$ ) on the  $C/N_0$  estimation process, an extension of this work is provided in this section. The Fisher information matrix, calculated using Eq. (3.8), is given by

$$I_d(\boldsymbol{\theta}) = \frac{N}{\sigma_n^4} \begin{bmatrix} \sigma_n^2 - \sigma_n^2 \frac{h(\alpha, K)}{K} & A \frac{h(\alpha, K)}{K} \\ A \frac{h(\alpha, K)}{K} & \frac{1}{2} - \frac{A^2 h(\alpha, K)}{\sigma_n^2 K} \end{bmatrix} \quad (3.17)$$

where  $h(\alpha, K)$  is a scalar function defined as

$$h(\alpha, K) = \frac{\exp(-K\alpha)}{\sqrt{2\pi K}} \int_{-\infty}^{+\infty} \frac{u^2 \exp\left(-\frac{u^2}{2K}\right)}{\cosh(u\sqrt{2\alpha})} du. \quad (3.18)$$

A detailed characterisation of  $h(\alpha, K)$  is provided in Section 3.3.4 . Using the Fisher information matrix (Eq. (3.17)), the CRLB for C/N<sub>0</sub> estimation on the data channel is given by

$$CRLB_d(g(\boldsymbol{\theta})) = K \frac{200}{N(\ln 10)^2} \frac{\frac{1}{\alpha} \frac{1}{K} h(\alpha, K) + 1}{K - 4\alpha h(\alpha, K) - h(\alpha, K)} [dB^2]. \quad (3.19)$$

Substituting  $K = 1$  in Eq. (3.19) yields the CRLB for ‘one observation per data bit’, which is the case considered by Alagha (2001).

### 3.3.3 Case – 3: Joint Data/Pilot

The observations at the input of the C/N<sub>0</sub> estimation process which uses both the data and pilot channels is given by  $\mathbf{x} = [\mathbf{x}_D^T \quad \mathbf{x}_P^T]^T$ . The joint pdf,  $p(\mathbf{x}; \boldsymbol{\theta})$ , is given by

$$p(\mathbf{x}; \boldsymbol{\theta}) = p(\mathbf{x}_D; \boldsymbol{\theta}) p(\mathbf{x}_P; \boldsymbol{\theta}). \quad (3.20)$$

Defining  $P \equiv \ln(p(\mathbf{x}; \boldsymbol{\theta}))$  and  $y_m = \{\sum_{k=1}^K x_{m,k}\}$ , the following expression is obtained for  $P$ :

$$P = -N \ln 2\pi\sigma_n^2 - \frac{NA^2}{\sigma_n^2} + \frac{A}{\sigma_n^2} \sum_{n=N+1}^{2N} x_n - \frac{1}{2\sigma_n^2} \sum_{n=1}^{2N} x_n^2 + \sum_{m=1}^M \ln \cosh\left(\frac{A}{\sigma_n^2} y_m\right) \quad (3.21)$$

where the pdf of  $y_m$  is given by

$$p(y_m; \theta) = \frac{1}{\sqrt{2\pi K \sigma_n^2}} \exp\left(-\frac{1}{2K\sigma_n^2} (y_m^2 + K^2 A^2)\right) \cosh\left(\frac{y_m A}{\sigma_n^2}\right). \quad (3.22)$$

The CRLB for  $g(\boldsymbol{\theta})$  for the joint data/pilot case is given by

$$CRLB_{dp}(g(\boldsymbol{\theta})) = \frac{\partial g(\boldsymbol{\theta})}{\partial \boldsymbol{\theta}} I_{dp}^{-1}(\boldsymbol{\theta}) \left(\frac{\partial g(\boldsymbol{\theta})}{\partial \boldsymbol{\theta}}\right)^T \quad (3.23)$$

where  $\frac{\partial g(\boldsymbol{\theta})}{\partial \boldsymbol{\theta}}$  is the Jacobian matrix defined as

$$\frac{\partial g(\boldsymbol{\theta})}{\partial \boldsymbol{\theta}} = \left[ \frac{\partial g(\boldsymbol{\theta})}{\partial A} \quad \frac{\partial g(\boldsymbol{\theta})}{\partial \sigma_n^2} \right] \quad (3.24)$$

and the transformation  $g(\boldsymbol{\theta})$  is defined in Eq. (3.14). The Fisher information matrix,  $I_{dp}(\boldsymbol{\theta})$ , for the joint data/pilot case is given as

$$[I_{dp}(\boldsymbol{\theta})]_{ij} = -E \left[ \frac{\partial^2 P}{\partial \theta_i \partial \theta_j} \right]. \quad (3.25)$$

The partial derivatives of Eq. (3.25) are given as

$$\frac{\partial^2 P}{\partial A^2} = -\frac{2N}{\sigma_n^2} + \frac{1}{\sigma_n^4} \sum_{m=1}^M \left( \frac{y_m^2}{\cosh^2\left(\frac{A}{\sigma_n^2} y_m\right)} \right) \quad (3.26)$$

$$\frac{\partial^2 P}{\partial A \partial \sigma_n^2} = \frac{\partial^2 P}{\partial \sigma_n^2 \partial A}$$

$$= \frac{2NA}{\sigma_n^4} - \frac{1}{\sigma_n^4} \sum_{n=N+1}^{2N} x_n \quad (3.27)$$

$$- \frac{1}{\sigma_n^4} \sum_{m=1}^M \left\{ \frac{A}{\sigma_n^2} \frac{y_m^2}{\cosh^2\left(\frac{A}{\sigma_n^2} y_m\right)} + y_m \tanh\left(\frac{A}{\sigma_n^2} y_m\right) \right\}$$

$$\begin{aligned} \frac{\partial^2 P}{\partial (\sigma_n^2)^2} &= \frac{N}{\sigma_n^4} - \frac{2NA^2}{\sigma_n^6} + \frac{2A}{\sigma_n^6} \sum_{n=N+1}^{2N} x_n - \frac{1}{\sigma_n^6} \sum_{n=1}^{2N} x_n^2 \\ &+ \frac{1}{\sigma_n^6} \sum_{m=1}^M \left\{ \frac{y_m^2}{\cosh^2\left(\frac{A}{\sigma_n^2} y_m\right)} \frac{A^2}{\sigma_n^2} + 2A y_m \tanh\left(\frac{A}{\sigma_n^2} y_m\right) \right\}. \end{aligned} \quad (3.28)$$

The following identities are used to evaluate the expectation of the derivatives listed above. The proof of these identities is provided in Appendix B.

*Identity 1:*

$$E \left[ \frac{y_m^2}{\cosh^2 \left( \frac{A}{\sigma_n^2} y_m \right)} \right] = \sigma_n^2 h(\alpha, K) \quad (3.29)$$

*Identity 2:*

$$E \left[ r \tanh \left( \frac{rA}{\sigma_n^2} \right) \right] = A \quad (3.30)$$

where  $r$  is a random variable that follows the distribution  $(p(r; \theta))$  given by

$$p(r; \theta) = \frac{1}{\sqrt{2\pi\sigma_n^2}} \exp \left( -\frac{r^2 + A^2}{2\sigma_n^2} \right) \cosh \left( \frac{rA}{\sigma_n^2} \right). \quad (3.31)$$

By using Identity 2, it can be shown that

$$E \left[ y_m \tanh \left( \frac{A}{\sigma_n^2} y_m \right) \right] = KA. \quad (3.32)$$

Applying the expectation operation on the partial derivatives in Eq. (3.26), (3.27) and (3.28), the Fisher Information Matrix ( $I_{dp}(\boldsymbol{\theta})$ ) becomes

$$I_{dp}(\boldsymbol{\theta}) = \frac{2N}{\sigma_n^4} \begin{bmatrix} \sigma_n^2 - \frac{\sigma_n^2}{2K} h(\alpha, K) & \frac{A}{2K} h(\alpha, K) \\ \frac{A}{2K} h(\alpha, K) & \frac{1}{2} - \frac{1}{2K} \frac{A^2}{\sigma_n^2} h(\alpha, K) \end{bmatrix} \quad (3.33)$$

and the determinant is given by

$$|I_{dp}(\boldsymbol{\theta})| = \frac{2N}{\sigma_n^4} \left( \frac{\sigma_n^2}{2} - \frac{A^2}{2K} h(\alpha, K) - \frac{\sigma_n^2}{4K} h(\alpha, K) \right). \quad (3.34)$$

The CRLB for the estimation of  $g(\theta)$  using both the data and pilot channels can be derived using Eq. (3.23) as

$$\begin{aligned}
& CRLB_{dp}(g(\boldsymbol{\theta})) \\
&= \frac{1}{|I_{dp}(g(\boldsymbol{\theta}))|} \frac{1}{(\ln 10)^2} \begin{bmatrix} \frac{20}{A} & -\frac{10}{\sigma_n^2} \end{bmatrix} \begin{bmatrix} \frac{1}{2} - \frac{1}{2K} \frac{A^2}{\sigma_n^2} h(\alpha, K) & -\frac{A}{2K} h(\alpha, K) \\ -\frac{A}{2K} h(\alpha, K) & \sigma_n^2 - \frac{\sigma_n^2}{2K} h(\alpha, K) \end{bmatrix} \begin{bmatrix} \frac{20}{A} \\ -\frac{10}{\sigma_n^2} \end{bmatrix} \quad (3.35)
\end{aligned}$$

which reduces to

$$CRLB_{dp}(g(\boldsymbol{\theta})) = K \frac{200}{N (\ln 10)^2} \frac{\left[ \frac{1}{\alpha} - \frac{1}{2K} h(\alpha, K) + 1 \right]}{2K - h(\alpha, K) - 4\alpha h(\alpha, K)} [dB^2]. \quad (3.36)$$

### 3.3.4 Properties of $h(\alpha, K)$

The integrand of Eq. (3.18) is plotted in Figure 3-2. The  $C/N_0$  for this case is chosen as 8 dB-Hz since the area under the curve diminishes for large  $C/N_0$ . To numerically evaluate the function defined in Eq. (3.18), the integration limits have to be finite. For  $C/N_0$  values of interest to the GNSS community, the integrand of  $h(\alpha, K)$  is significant for  $|u| < 20$ , where  $u$  is a variable in the integrand in Eq. (3.18) and the integration is performed with respect to it. Thus, to calculate the area under the curve,

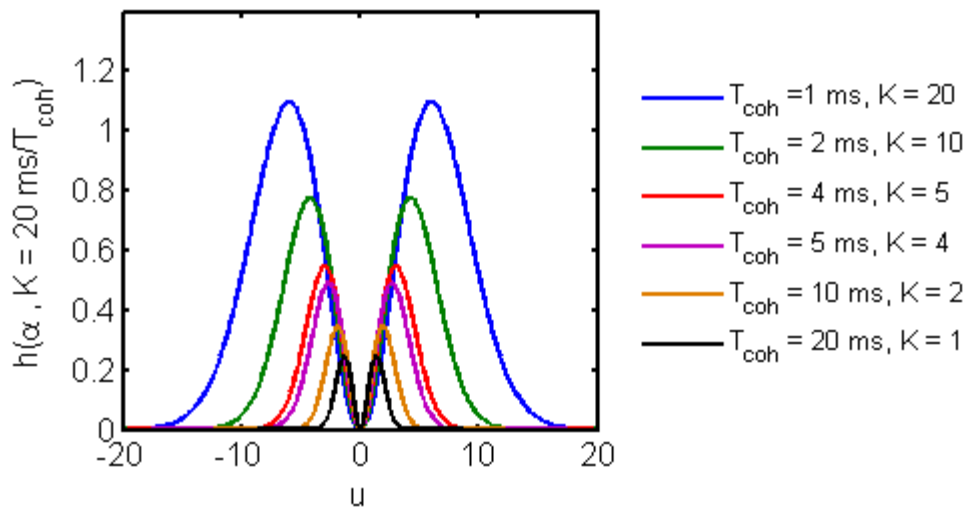


**Figure 3-2: Plot of the integrand of  $h(\alpha, K)$  for different  $T_{coh}$  and  $K$  at a  $C/N_0$  of 8 dB-Hz**

numerical integration is performed for  $|u| < 50$  with a step size of  $5 \times 10^{-4}$  to allow for sufficient accuracy.

Figure 3-3 shows the area under the curve for different values of  $T_{coh}$  ( $K = 20 \text{ ms}/T_{coh}$ ). Theoretically, the choice of the predetection interval,  $T_{coh}$ , will not have a significant impact on  $C/N_0$  estimation for received  $C/N_0 > 25 \text{ dB-Hz}$ , as  $h(\alpha, K) \rightarrow 0$ . By substituting  $h(\alpha, K) \rightarrow 0$  in  $CRLB_d(g(\theta))$ , defined by Eq.(3.19), namely

$$CRLB_d(g(\theta))\big|_{h(\alpha, K) \rightarrow 0} = K \frac{200}{N (\ln 10)^2} \frac{\left(1 + \frac{1}{\alpha}\right)}{K} = CRLB_p(g(\theta)), \quad (3.37)$$

it can be verified that  $CRLB_d$  approaches  $CRLB_p$  for large  $C/N_0$ .  $h(\alpha, K)$  increases significantly for weak GNSS signals, and hence, the theoretical performance bounds for the data and pilot channels start to differ considerably.

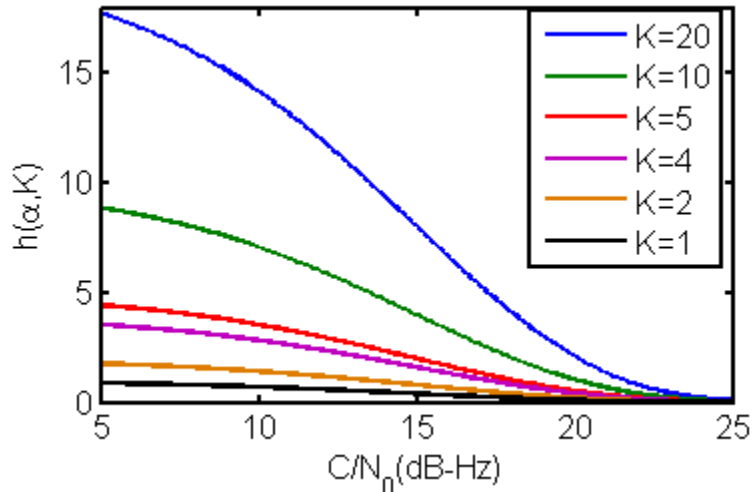


**Figure 3-3: Plot of  $h(\alpha, K)$  against  $C/N_0$  for different values of  $T_{coh}$  and  $K = 20/T_{coh}$**

### 3.3.5 Theoretical Gain Analysis of Joint Data/Pilot $C/N_0$ estimation

#### 3.3.5.1 Theoretical Bound on Achievable Gain

The theoretical bound on performance gain in noise variance reduction by using both the data and pilot channels for  $C/N_0$  estimation against the use of the pilot channel alone is provided in this section.

For very high  $C/N_0$ ,  $h(\alpha, K) \rightarrow 0$ . Thus, comparing Eq. (3.16) and (3.36) leads to

$$\left. \frac{CRLB_{dp}}{CRLB_p} \right|_{h(\alpha, K) \rightarrow 0} = \frac{1}{2} \Rightarrow 3 \text{ dB reduction in noise variance.} \quad (3.38)$$

Thus, using both the data and pilot channel leads to a 3 dB reduction in noise variance (gain). For a very low  $C/N_0$  such as 5 dB-Hz, which corresponds to a scaled SNR of  $\alpha = 0.0016$  for  $T_{coh} = 1 \text{ ms}$ , and  $K = 20$ ,  $h(\alpha, K)$  is approximately equal to 18.

Comparing the CRLB bound leads to

$$\left. \frac{CRLB_{dp}}{CRLB_p} \right|_{h(\alpha, K) \rightarrow 18} \Rightarrow 0.4 \text{ dB reduction in noise variance.} \quad (3.39)$$

With the results from the above analysis for maximum and minimum values of  $C/N_0$  of interest, it is clear that the theoretical gain in noise variance reduction by using both channels decreases with the  $C/N_0$ . To highlight the change in gain for weak signals, a numerical computation is performed for different choices of  $T_{coh}$  ( $K = 20 \text{ ms}/T_{coh}$ ). Figure 3-4 shows that a 3 dB gain in noise variance reduction is possible for  $C/N_0 > 25$  dB-Hz. However, below 25 dB-Hz, the curves show the effect of the value of  $K$  ( $T_{coh}$ ) on  $C/N_0$  estimation.

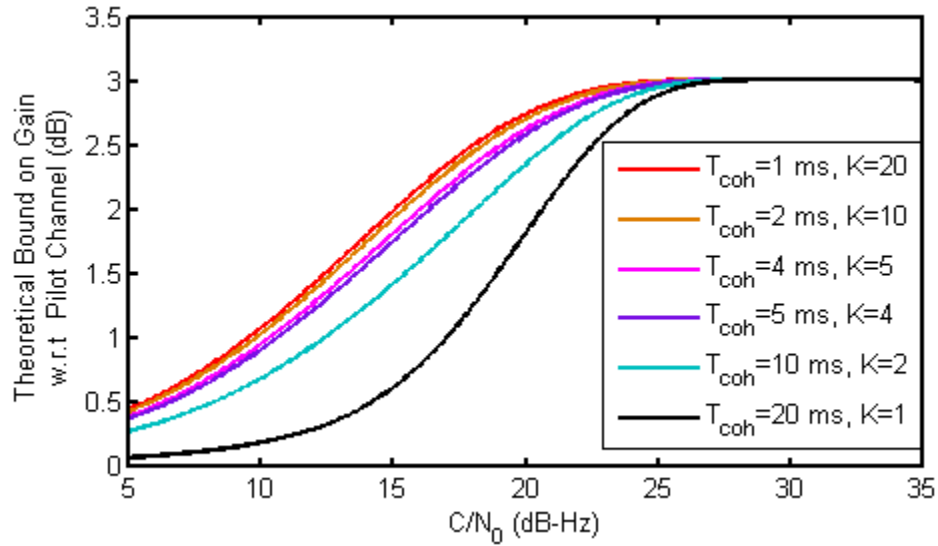


**Figure 3-4: Theoretical gain in noise variance reduction by using both the data and pilot channels for  $C/N_0$  estimation as compared to using pilot channel only**

### 3.3.5.2 Effect of $T_{coh}$ on achievable gain

A choice of 1 ms for  $T_{coh}$  with the knowledge of  $K = 20$  observations per data bit has a greater gain at low  $C/N_0$  as compared to the use of  $T_{coh} = 20$  ms where the data bit sign is uncorrelated across all observations. This difference in performance can be explained using the concept of sufficient statistics for data channel observations alone. When  $\mathbf{x}_D$  is populated with 1 ms observations, it can be considered a set which contains all the information required. Define  $\mathbf{x}'_D$  as the vector that contains accumulations of  $\mathbf{x}_D$  over every data bit period ( $\mathbf{x}'_D \subset \mathbf{x}_D$ ):

$$\mathbf{x}'_D = \left\{ x'_D(m) = \sum_{k=1}^{20} x_{m,k} \quad \forall m = 1 \dots M \right\}. \quad (3.40)$$

The sufficient statistics for the vector ( $\mathbf{x}_D$ ) are given by  $T_{1,d}(x)$  and  $T_{2,d}(x)$  where

$$T_{1,d}(x) = \left\{ \sum_k x_{m,k} \quad \forall m = 1 \dots M \right\} \quad (3.41)$$

$$T_{2,d}(x) = \sum_n x_n^2 \quad \forall n = 1 \dots N. \quad (3.42)$$

If  $\mathbf{x}'_{\mathcal{D}}$  can be shown to allow the computation of both  $T_{1,d}(x)$  and  $T_{2,d}(x)$ , the performance would be the same regardless of the  $T_{coh}$  chosen.  $T_{1,d}(x)$  can be directly evaluated from  $\mathbf{x}'_{\mathcal{D}}$ , but the information conveyed by  $T_{2,d}(x)$  is lost in transforming  $\mathbf{x}_{\mathcal{D}}$  to  $\mathbf{x}'_{\mathcal{D}}$ . This provides an intuitive explanation for the difference in performance based on the choice of  $T_{coh}$ . A rather complicated way to prove this is to show that  $p(T_{2,d}(x)|\mathbf{x}'_{\mathcal{D}})$  does not depend on the unknown parameters ( $\boldsymbol{\theta}$ ) (Kay 1993).

### 3.4 Maximum Likelihood (ML) Estimators

The CRLB analysis in the previous section addresses the theoretical bounds on the achievable gain by using both the data and pilot channels. This section derives estimators for weak GPS signals which perform close to the bounds without significant bias. A ML estimator using data channel inputs is derived and analyzed to outline the issue with the validity of the approximations under weak GPS signal conditions. An iterative solution to overcome the issue is then evaluated with emphasis on its convergence percentage. This is then carried forward to derive an estimator which uses both the data and pilot channels and effectively overcomes the problems faced in the iterative procedure. In both cases,  $T_{coh}$  is fixed to 1 ms ( $K = 20$ ) based on the previous analysis.

#### 3.4.1 ML Estimator – Data Channel

Using the pdf function defined in Eq. (3.8), the partial derivatives of the likelihood function are computed with respect to  $A$  and  $\sigma_n^2$  as

$$\frac{\partial}{\partial A} [\ln p(\mathbf{x}_D; \boldsymbol{\theta})] \Big|_{\hat{\boldsymbol{\theta}}} = \hat{A} - \frac{1}{N} \sum_m \left[ y_m \tanh \left( \frac{\hat{A}}{\hat{\sigma}_n^2} y_m \right) \right] = 0 \quad (3.43)$$

$$\begin{aligned} \frac{\partial}{\partial \sigma_n^2} [\ln p(\mathbf{x}_D; \boldsymbol{\theta})] \Big|_{\hat{\boldsymbol{\theta}}} \\ &= 1 - \frac{\hat{A}^2}{\hat{\sigma}_n^2} - \frac{1}{\hat{\sigma}_n^2} \frac{1}{N} \sum_n x_n^2 + \frac{2\hat{A}}{\hat{\sigma}_n^2} \frac{1}{N} \sum_m \left[ y_m \tanh \left( \frac{\hat{A}}{\hat{\sigma}_n^2} y_m \right) \right] \\ &= 0. \end{aligned} \quad (3.44)$$

The ML estimate for noise variance ( $\hat{\sigma}_n^2$ ) is obtained by substituting (3.43) into (3.44), and is

$$\hat{\sigma}_n^2 = \frac{1}{N} \sum_n x_n^2 - \hat{A}^2. \quad (3.45)$$

The amplitude cannot be directly evaluated because of the presence of the *tanh* function.

The following approximation can be used to simplify the computation (Li et al 2002):

$$y_m \tanh \left( y_m \frac{2\hat{\alpha}}{\hat{A}} \right) \approx y_m \operatorname{sign}(y_m) = |y_m|. \quad (3.46)$$

The approximation in Eq. (3.46) is valid for real, positive values of  $\hat{\alpha}$  and  $\hat{A}$ . Using Eq. (3.46) in Eq.(3.43) yields

$$\hat{A} = \frac{1}{N} \sum_m |y_m|. \quad (3.47)$$

Using the invariance property (Kay 1993), the ML estimator for C/N<sub>0</sub> is given by

$$\left( \frac{C}{N_0} \right)_{dB-Hz} = 10 \log_{10} \hat{\alpha} - 10 \log_{10} \left( \frac{T_{coh}}{2} \right) \quad (3.48)$$

where  $\hat{\alpha} = \frac{\hat{A}^2}{2\hat{\sigma}_n^2}$  is the ML estimate of the post correlation SNR.

To verify the validity of the approximation used, a numerical simulation was performed with unit amplitude,  $T_{coh} = 1 \text{ ms}$ , and  $K = 20$ . The mean of the  $\tanh$  function is plotted as a function of  $C/N_0$  in Figure 3-5. The  $\text{sign}$  function in Eq. (3.46) maps the curve to  $\{+1, -1\}$  depending on the data bit sign. It is clear that the approximation is valid for  $C/N_0$  greater than 25 dB-Hz and starts to degrade for weak signals. This leads to a considerable bias in  $C/N_0$  estimation of weak GNSS signals.

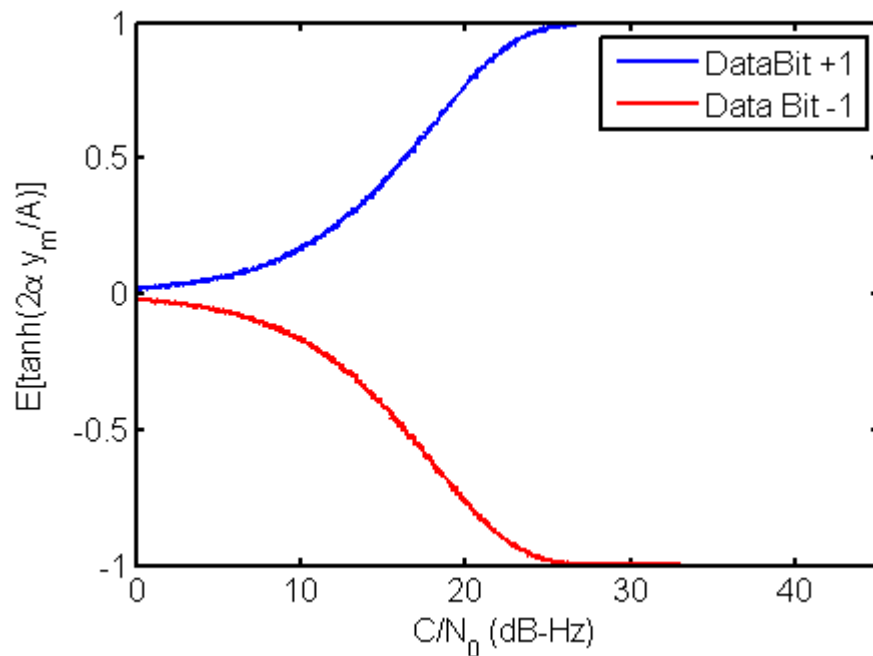


**Figure 3-5: The mean of  $\tanh(2\alpha y_m/A)$  evaluated as a function of  $C/N_0$  with unit amplitude ( $A=1$ ).**

### 3.4.2 Iterative ML Estimator – Data Channel

To overcome the problem of bias in the  $C/N_0$  estimate for weak signals, iterative approaches can be used (Li et al 2002). In this work, the Newton-Raphson method is used to solve Eq. (3.43), the ML equation for amplitude. Initial estimates for the iterative procedure are obtained using the estimates given by the approximate solution described above. Let  $g_d(a)$  be

$$g_d(a) = a - \frac{1}{N} \sum_m \left[ y_m \tanh \left( \frac{2\alpha}{a} y_m \right) \right]. \quad (3.49)$$

The roots of  $g_d(a)$  correspond to the ML estimate of  $A$ . In this iterative method,  $\alpha$  is considered independent of  $A$  and thus is treated as a constant in the partial derivative  $\partial g_d / \partial a$ . An optimization with respect to  $A$  is performed to reduce the dimensionality of the search.

The update for  $\hat{A}_{i+1}$  is obtained as

$$\hat{A}_{i+1} = \hat{A}_i - \frac{g_d(\hat{A}_i)}{\left. \frac{\partial g_d(a)}{\partial a} \right|_{\hat{A}_i}} \quad (3.50)$$

where  $\hat{A}_i$  is the amplitude estimate at the  $i$ -th iteration and the partial derivative is given by

$$\frac{\partial g_d(a)}{\partial a} = 1 + \frac{1}{N} \frac{2\alpha}{a^2} \sum_m \left[ \frac{y_m^2}{\cosh^2 \left( \frac{2\alpha}{a} y_m \right)} \right]. \quad (3.51)$$

Once  $\hat{A}_{i+1}$  is obtained,  $\widehat{\sigma}_{n_{i+1}}^2$  is updated using Eq. (3.45), which is then used to compute  $\hat{\alpha}_{i+1}$ . The initial estimate,  $\hat{A}_1$ , is obtained using the approximate version of the ML estimator, as given by Eq. (3.47). The above implementation actually searches for a root of the equation  $g_{ML,d}(a) = 0$ , given by

$$g_{ML,d}(a) = a - \frac{1}{N} \sum_m \left[ y_m \tanh \left( \frac{a}{P_d - a^2} y_m \right) \right] \quad (3.52)$$

where

$$P_d = \frac{1}{N} \sum_n x_n^2. \quad (3.53)$$

Eq. (3.52) is obtained by substituting Eq. (3.45) into Eq. (3.43).

Figure 3-6 shows the improvement in performance obtained by using the iterative method to compute the  $C/N_0$  as compared to the MLE with approximation. The plot is obtained with 10 iterations per estimate with a  $C/N_0$  output rate of 500 ms (corresponding  $T_{coh} = 1$  ms,  $K = 20$ ,  $N = 500$ ). A total of  $10^4$  estimates are averaged for each considered  $C/N_0$ . As shown in Figure 3-6, the ML estimator with approximation is considerably biased for  $C/N_0$  values less than 20 dB-Hz, and hence does not parallel the CRLB bound for variance. The iterative method is significantly less biased than the approximate MLE.

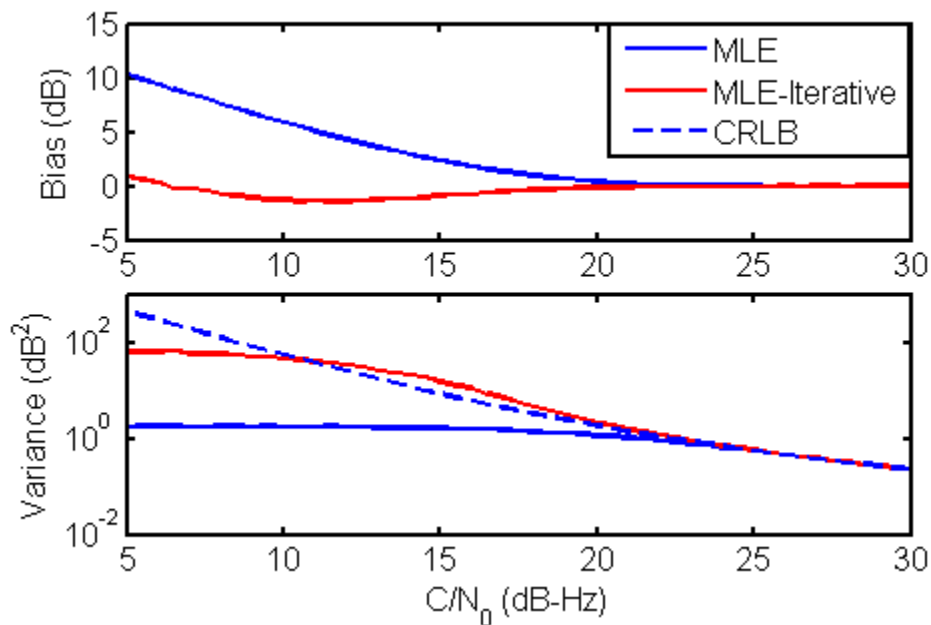


**Figure 3-6: Performance analysis of iterative MLE against MLE with approximation using data channel only**

Although the iterative method involves computing the  $\tanh(\cdot)$  and  $\cosh^2(\cdot)$  functions, this can be performed in offline software receivers where computational complexity is not of significant concern. This is particularly helpful in determining the

performance of algorithms proposed for weak signal environments, where offline tests can be carried out. Another option is to use look-up tables for real-time applications.

Since the initial estimate for the data channel only  $C/N_0$  estimator is obtained from the MLE with approximation, this might lead to poor initialization of the iterative algorithm. Further, as shown in Figure 3-7, the roots of  $g_{ML,d}(a)$  includes  $\{\pm A, 0\}$  even under noiseless conditions. Hence, depending on the initial estimates used for the iterative procedure, the iteration can converge to any one of the three roots. Ignoring the possibility of negative initialization for the amplitude estimate, the iteration can converge either close to the original amplitude ( $a = +A$ ) or the origin ( $a = 0$ ). There are also some cases where the noise level is too high and the root  $a = +A$  vanishes under such low SNR conditions. When the iteration converges to  $a = 0$ , the  $C/N_0$  estimate becomes  $-\infty$ . This condition is referred to as divergence. Convergence is declared when the iterative algorithm settles on a non-zero root ( $a > 0$ ).

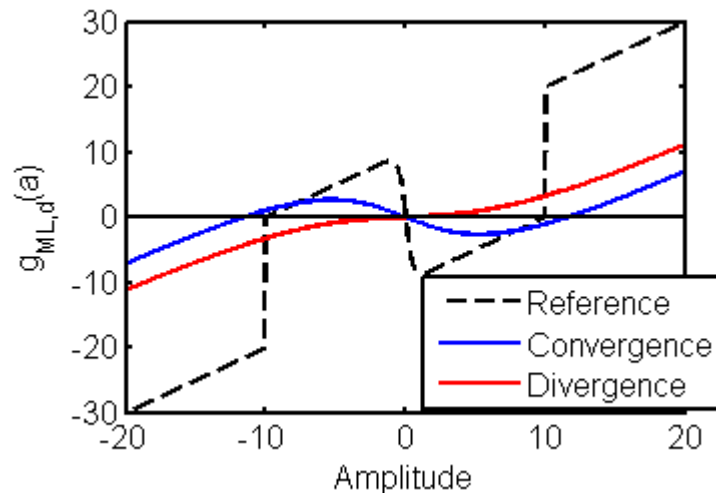


**Figure 3-7: Plot of  $g_{ML,d}(a)$  for a  $C/N_0$  of 15 dB-Hz under two different conditions (i) Convergence and (ii) Divergence. The reference curve corresponds to the noise-less condition. Original amplitude ( $A$ ) is set as 10.**

Hence, in order to analyse the convergence percentage, a simple detector is utilized. For each  $C/N_0$  estimate, the algorithm is allowed to run for 100 iterations to check for divergence. Since the maximum variance of the estimator can be of the order of  $10^2$  (corresponding to a  $C/N_0$  of 5 dB-Hz), which translates to  $1\sigma_{est} = \pm 10$  dB, convergence is declared when both of the following conditions are met:

- i.  $|\text{Final Estimate} - \text{Initial Estimate from ML with approximation}| < 30$  dB
- ii.  $|\text{Final Estimate} - \text{True } C/N_0| < 10$  dB

The first condition is a rough check designed for early detection of divergence. The true  $C/N_0$  is the  $C/N_0$  used to simulate the input vectors and would not be available under live signal conditions. The results shown in Figure 3-8 are averaged across  $10^4$  such estimates.

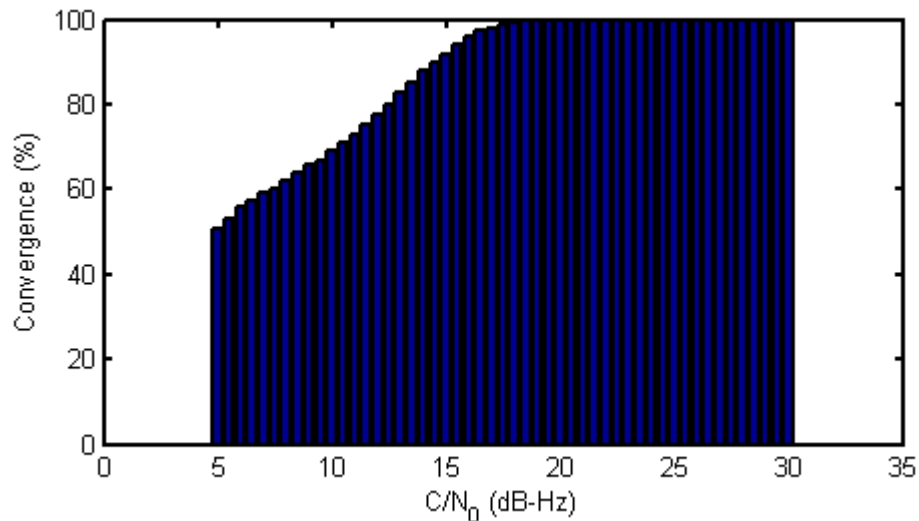


**Figure 3-8: Convergence percentage for the iterative ML estimator using data channel only**

The convergence percentage of the iterative algorithm drops slowly below 20 dB-Hz, but is approximately 70% or greater for  $C/N_0$  values which are of interest to weak

signal positioning users (10 dB-Hz and above). This problem can be minimized by making use of the presence of the pilot channel (i.e., pilot channel ML estimates can be used as initial  $C/N_0$  estimates).

### 3.4.3 Joint Data/Pilot ML Estimator

The ML Estimator for  $C/N_0$  using both the data and pilot channel observations is derived (i) using the *tanh* approximation, and (ii) using the iterative method as described in Section 3.4.2.

*With Approximation:*

Maximizing  $P$  defined in Eq. (3.21) w.r.t  $\theta$ , one obtains

$$\frac{\partial P}{\partial A} = -\frac{2NA}{\sigma_n^2} + \frac{1}{\sigma_n^2} \sum_{n=N+1}^{2N} x_n + \frac{1}{\sigma_n^2} \sum_m \left( y_m \tanh\left(\frac{A}{\sigma_n^2} y_m\right) \right) = 0 \quad (3.54)$$

$$\begin{aligned} \frac{\partial P}{\partial \sigma_n^2} &= -\frac{N}{\sigma_n^2} + \frac{NA^2}{\sigma_n^4} - \frac{A}{\sigma_n^4} \sum_{n=N+1}^{2N} x_n + \frac{1}{2\sigma_n^4} \sum_{n=1}^{2N} x_n^2 - \frac{A}{\sigma_n^4} \sum_m \left( y_m \tanh\left(\frac{A}{\sigma_n^2} y_m\right) \right) \\ &= 0. \end{aligned} \quad (3.55)$$

Eq. (3.54) can also be written as

$$\sum_m \left( y_m \tanh\left(\frac{A}{\sigma_n^2} y_m\right) \right) = 2NA - \sum_{n=N+1}^{2N} x_n. \quad (3.56)$$

Substituting Eq.(3.56) into Eq.(3.55), the ML estimate for variance is given as

$$\widehat{\sigma_n^2} = \left( \frac{1}{2N} \left[ \sum_{n=1}^{2N} x_n^2 \right] \right) - \hat{A}^2. \quad (3.57)$$

Applying the *tanh* approximation in Eq. (3.54), the amplitude estimate is given as

$$\hat{A} = \frac{1}{2N} \left( \sum_m |y_m| + \sum_{n=N+1}^{2N} x_n \right). \quad (3.58)$$

i. *Iterative Procedure:*

Define a function  $g_{DP}(a)$  as

$$g_{DP}(a) = 2a - \frac{1}{N} \sum_{n=N+1}^{2N} x_n - \frac{1}{N} \sum_m \left[ y_m \tanh\left(\frac{2\alpha}{a} y_m\right) \right] \quad (3.59)$$

whose roots corresponds to the ML estimate of amplitude ( $\hat{A}$ ). The partial derivative, with  $\alpha$  considered independent of  $A$ , is given by

$$\frac{\partial g_{DP}(a)}{\partial a} = 2 + \frac{1}{N} \frac{2\alpha}{a^2} \sum_m \left[ \frac{y_m^2}{\cosh^2\left(\frac{2\alpha}{a} y_m\right)} \right]. \quad (3.60)$$

The iterative procedure using both the data and pilot channel observations has an advantage compared to using the data channel alone. With the iterative procedure, a more valid initial estimate can be obtained using the pilot channel alone. This in turn ensures convergence even for weak signals and also reduces the noise variance.

Thus initializing  $\hat{A}_1$  and  $\hat{\alpha}_1$  using the MLE on the pilot channel alone, the amplitude estimate is updated every iteration as

$$\hat{A}_{i+1} = \hat{A}_i - \frac{g_{DP}(\hat{A}_i)}{\left. \frac{\partial g_{DP}(a)}{\partial a} \right|_{\hat{A}_i}}. \quad (3.61)$$

#### 3.4.4 Performance Analysis

The joint data/pilot MLE, for both cases (i), with approximation, and (ii), iterative, is compared against the MLE for pilot channel alone using numerical simulations. The following simulation parameters are used:

- i.  $T_{coh} = 1 \text{ ms}, K = 20$
- ii.  $C/N_0$  update time of 500 ms ( $N = 500$ )

- iii. 10 iterations per estimate (this is an empirical choice made using numerical simulations for the number of iterations required by the algorithm to settle on a root)
- iv. Initial estimates for  $\hat{A}_1$  and  $\hat{\alpha}_1$  correspond to the MLE obtained using the pilot channel alone
- v. Bias and variance are measured as the mean of  $10^4$  such estimates.

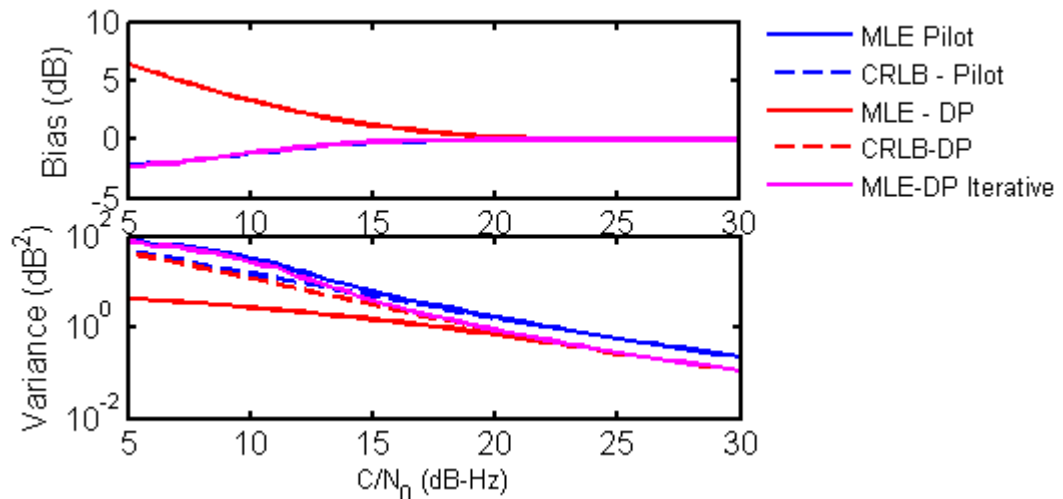


**Figure 3-9: Comparison of MLE using both the data and pilot channels (DP) (i) with approximation (MLE-DP) (ii) iterative procedure (MLE-DP Iterative) against a MLE using pilot channel only (MLE-Pilot)**

Figure 3-9 shows the results obtained for the bias level and noise variance with the corresponding CRLB as reference. The joint data/pilot MLE with approximation performs similarly to the pilot channel in terms of bias for  $C/N_0 > 20$  dB-Hz and follows the derived CRLB. However, as the  $C/N_0$  drops below 20 dB-Hz, the joint data/pilot MLE with approximation gradually becomes biased and no longer follows the defined bound (since the bound is valid only for an unbiased estimator (Kay 1993)). Rather, the

iterative joint data/pilot ML estimator is able to provide estimates with significantly less bias and reduced noise variance.

Figure 3-10 compares the gain in noise variance reduction with the theoretical bound as plotted in Figure 3-4 for  $T_{coh} = 1 \text{ ms}$  and  $K = 20$ . The gain achieved using the iterative estimator closely follows the bound.

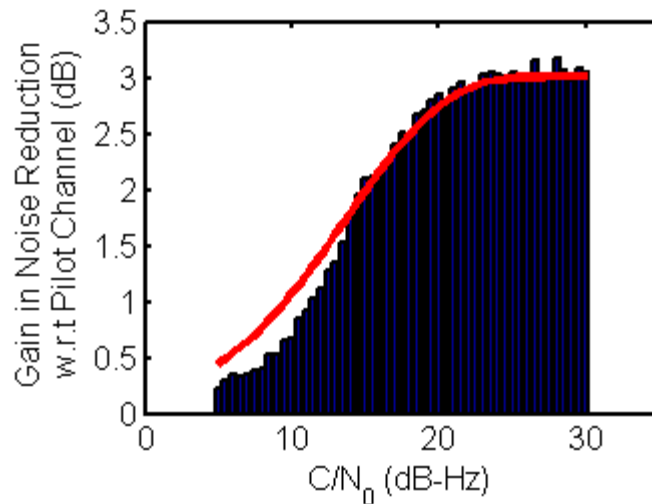


**Figure 3-10: Comparison of gain in noise variance reduction by using both the data and pilot channels as compared to using pilot channel alone**

Figure 3-11 compares the convergence percentage across  $C/N_0$  between the iterative ML estimator using the data channel alone, as described in Section 3.4.2, and the joint data/pilot iterative ML estimator. Convergence is declared based on conditions similar to those described in Section 3.4.2. The convergence percentage of the iterative MLE using both channels is greater than 90% even for  $C/N_0$  as low as 10 dB-Hz, which is a considerable improvement compared to that obtained from the iterative MLE using the data channel only. A word of caution regarding the interpretation of the results presented in Figure 3-8 and Figure 3-11 is in order. Due to the second constraint imposed in declaring convergence, that is the final estimate should be within  $1\sigma_{est} = \pm 10 \text{ dB}$ , any

estimate which falls outside this limit is also considered to have diverged even though the Newton-Raphson method converges to a positive amplitude estimate different from zero.

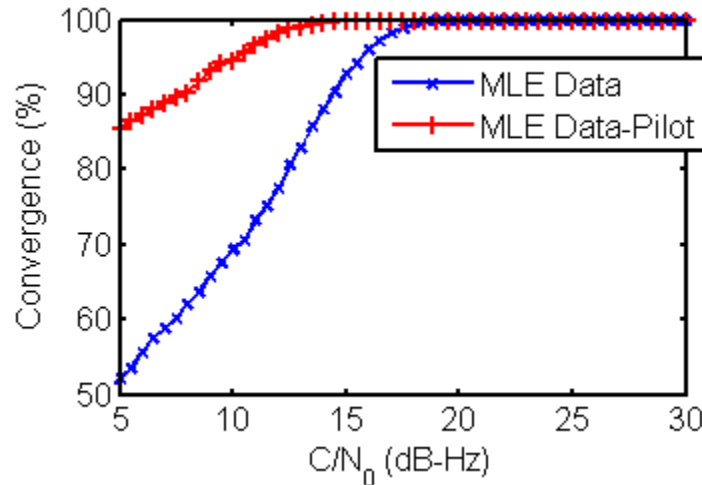


**Figure 3-11: Comparison of convergence percentage between iterative MLE using data channel alone and iterative MLE using both the data and pilot channels**

### 3.5 Implementation Aspects

To implement the above algorithm in practice, the following factors are of concern:

- i. the input to the  $C/N_0$  estimator is a complex signal (in-phase ( $I$ ) and quadrature ( $Q$ ) components of  $T_{coh}$  outputs);
- ii. non-zero phase and frequency errors in tracking degrade the effective  $C/N_0$ .

The data and pilot channel observations used in Section 3.4 to derive the ML estimators are assumed to be real. But in reality, due to phase tracking errors, the signal power is split across  $I$  and  $Q$ , and hence they are complex. A direct extension of the above algorithm is described in this section, where the operations in the real domain are transformed directly to the complex domain. Although optimality might be lost due to

this transformation, the results indicate satisfactory performance as compared to the standard estimators. Further, longer coherent summations on the pilot channel, as demanded by the MLE, makes the  $C/N_0$  estimates sensitive to frequency errors. To avoid this, the maximum coherent summation on the pilot channel is limited to  $L_{coh}$  ms.

The flow of the algorithm is described in Figure 3-12 for joint data/pilot MLE with approximation as well for joint data/pilot MLE with iteration. Initially, two quantities are derived from the 1 ms input blocks, one being a set of coherent summation outputs ( $y_{m,d}$  computed over every data bit period for the data channel and  $y_{m,p}$  computed over  $L_{coh}$  for pilot channel), and the other being the sum of squares of the 1 ms inputs. The *tanh* approximation is applied on the data channel coherent summation outputs ( $y_{m,d}$ ). The amplitude and net power (signal power + noise power) estimates from both data and pilot channels are averaged to obtain final estimates. These final estimates of amplitude and net power are used to compute the  $C/N_0$  estimate.

For the iterative joint data/pilot MLE, the amplitude estimate from the pilot channel alone and net power estimate, which is averaged across both channels, are used to initialize the iteration. Only the in-phase components of  $y_{m,d}$ , from the data channel, are used in the iteration module. Since only the in-phase components of data channel are used to compute the corrections for the amplitude estimate, carrier phase tracking errors are assumed to be low. However, for weak  $C/N_0$ , this implementation might introduce a further bias into the estimates due to degradation in carrier phase tracking errors. From the results described in Section 3.7, it was verified that the level of bias in estimates including this effect is considerably low until a  $C/N_0$  of 17 dB-Hz.

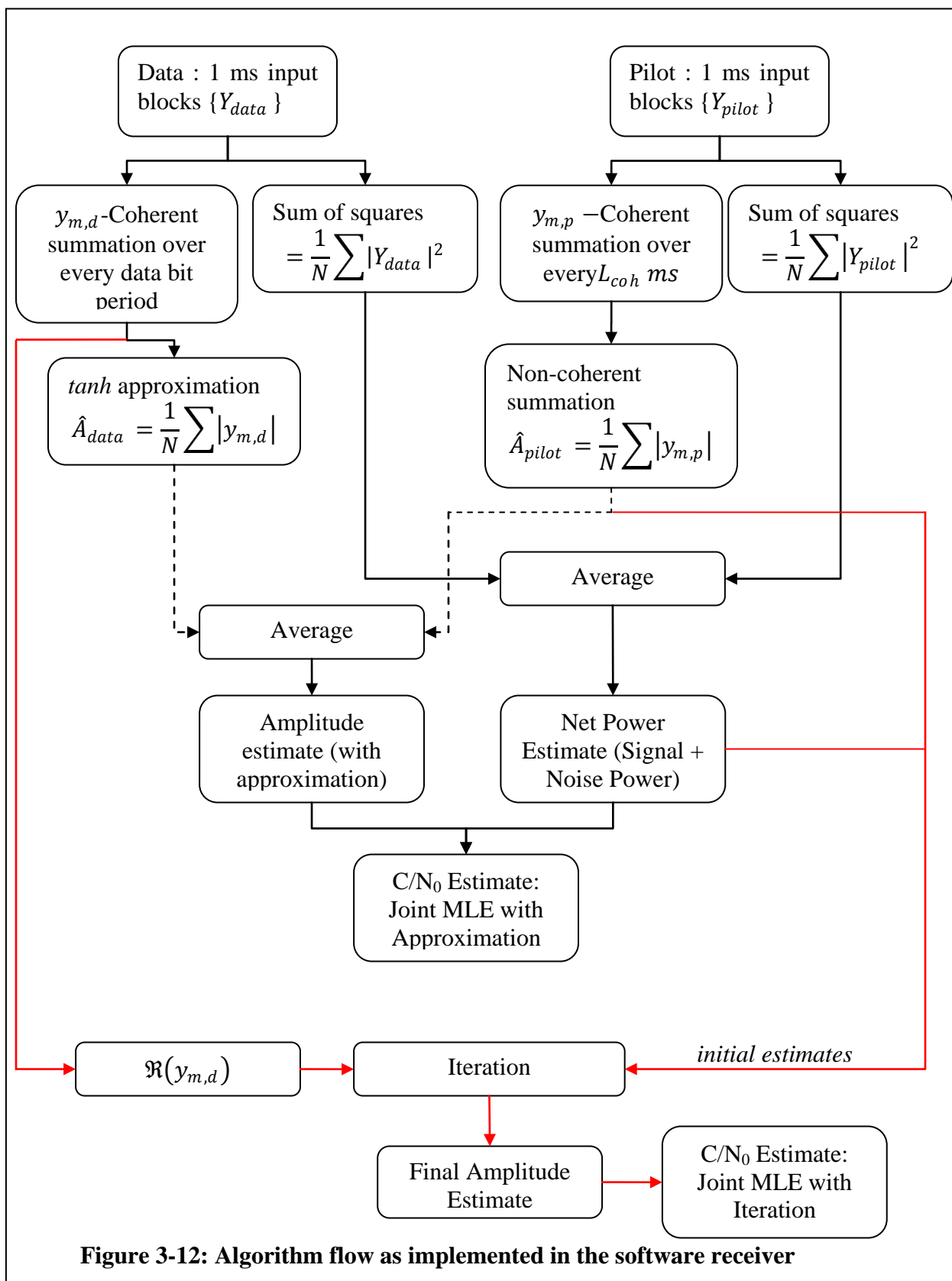


**Figure 3-12: Algorithm flow as implemented in the software receiver**

### 3.6 Test Methodology

For the analysis, a Spirent GSS7700 simulator was configured to generate L2C signals at a fixed signal power across the satellites in view. The signal power was reduced by 1.5 dB every 60 s. The initial power was fixed to produce a  $C/N_0$  of 35 dB-Hz. The choice of 35 dB-Hz was made in order to enable a stable reference  $C/N_0$  that would be without considerable bias. Two such data sets were collected and a total of 15 Satellite Vehicles (SVs) were included in the simulation. This gives, at a chosen  $C/N_0$  update rate of 500 ms,

$$60 \text{ s} \times 2 \text{ Hz} \times 15 \text{ PRN} = 1800 \text{ samples} \quad (3.62)$$

of  $C/N_0$  estimates for every level of attenuation, thus providing reliable results. The down-converted and digitized data was collected using a National Instruments (NI) RF front-end (NI PXI-5661 2006) at a sampling rate of 2.5 MHz (complex samples). This data was then post-processed with a modified version of the PLAN group's GSNRx software receiver (Petovello et al 2008). With a fixed architecture for tracking, the 1 ms accumulated correlator outputs from the prompt correlator were collected for further processing with MATLAB.

### 3.7 Results

The specifications of the estimator used are:

- i.  $T_{coh} = 1 \text{ ms}, K = 20$
- ii.  $C/N_0$  update rate of 500 ms,  $N = 500, M = 25$  data bit periods
- iii. Maximum coherent summation on pilot channel observations limited to  
 $L_{coh} = 100 \text{ ms}$
- iv. Iterations per estimate  $I = 10$

Figure 3-13 shows the average bias in measured  $C/N_0$  as compared to the reference  $C/N_0$  along with the  $\pm 1\sigma$  uncertainty. The ML estimator using both the data and pilot channels with the  $\tanh$  approximation becomes biased for  $C/N_0$  values less than  $24.5 \text{ dB} - \text{Hz}$  (bias greater than  $0.5 \text{ dB}$ ). The ML estimator using both the data and pilot channels with iteration stays much closer to the reference compared to the pilot channel only estimator. Bias in the estimates using the iterative ML estimator with both channels remains low until  $17 \text{ dB} - \text{Hz}$ . Only four of the 15 satellites were tracked for a  $C/N_0$  of  $15.5 \text{ dB} - \text{Hz}$ . Hence results for that point are not statistically significant. As mentioned in the implementation aspects (Section 3.5), it can be observed that the bias levels for the iterative procedure are significantly lower even though only the in-phase components of the data channel are used within the iteration module.

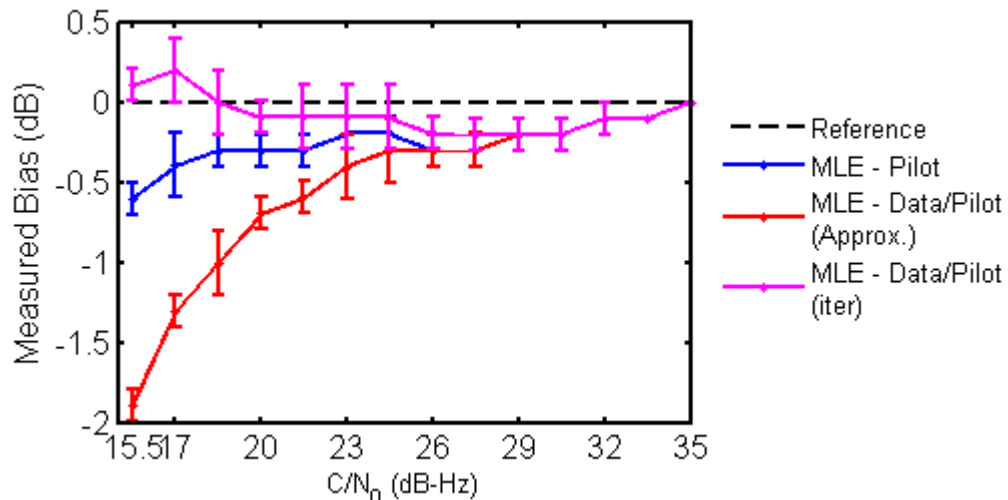


**Figure 3-13: Bias in estimates obtained from different estimators across  $C/N_0$**

Figure 3-14 compares the reduction in noise variance of the  $C/N_0$  estimates obtained by using both channels against using pilot channel alone. The CRLB bound on gain is given for reference. As mentioned previously, as the  $C/N_0$  drops below  $24.5$

dB – Hz, the joint data/pilot MLE with tanh approximation becomes significantly biased and, therefore, the CRLB bound is no longer valid for this estimator. Due to the significant bias in estimates at low  $C/N_0$ , the joint data/pilot MLE with approximation is not reliable for weak signals. In other words, although the noise variance reduction factor for the joint data/pilot MLE with approximation is higher than the iterative procedure for weak signals, significant bias in the estimates makes the joint data/pilot MLE with approximation unusable under such situations. Further, the gain is less than 3 dB for  $25 < C/N_0 < 35$  dB-Hz ( $\approx 2 - 2.5$  dB). A gain of 3 dB was predicted under ideal conditions, which are encountered only for  $C/N_0$  greater than 35 dB-Hz. The ML estimator which uses both the data and pilot channels and performs iterations to resolve for the non-linearity obeys the CRLB bound and continues to provide a gain even as the  $C/N_0$  drops to 17 dB – Hz.

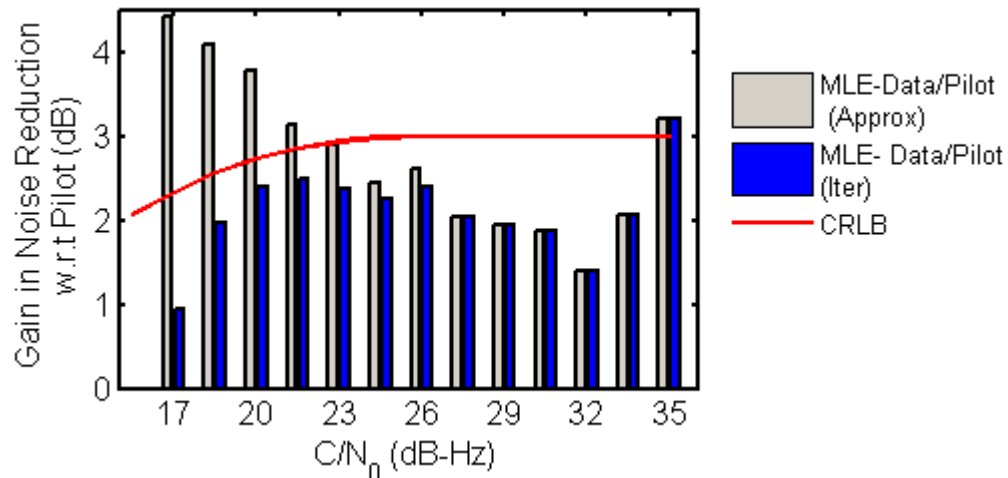


**Figure 3-14: Gain in noise variance reduction of data/pilot combined  $C/N_0$  estimation as compared to MLE which uses pilot channel only**

### 3.8 Summary

The theoretical analysis presented in this chapter gives the CRLB for the  $C/N_0$  estimation process using the data and pilot channels individually, as well as the CRLB for the case where both channels are used simultaneously. The bound on achievable gain, by using both channels, can be used as a reference to evaluate the performance of any joint data/pilot estimator. In this work, maximum-likelihood estimators that use both channels are derived. Although significant reduction in noise variance of the  $C/N_0$  estimates can be obtained by using both channels, the use of the tanh approximation introduces significant bias in the estimates. Hence, the joint data/pilot  $C/N_0$  estimation with approximation is unreliable for weak signals. The use of the Newton-Raphson method for an iterative solution of the ML equations was presented and divergence problems due to poor initial estimates were discussed. The novel joint data/pilot iterative ML solution was shown to provide a reliable  $C/N_0$  estimate with significantly less bias, improved convergence percentage, and reduced noise variance. The results indicate that the estimator is reliable down to 17 dB-Hz. For  $C/N_0$  values lower than 17 dB-Hz standard tracking loops lose lock and the  $C/N_0$  cannot be estimated.

## **CHAPTER FOUR: JOINT DATA/PILOT CARRIER FREQUENCY TRACKING**

Normally, carrier tracking is initiated with carrier frequency and code tracking. Carrier phase tracking is initiated after achieving frequency lock. Carrier frequency tracking is preferred at the initial stages over phase tracking to reduce the pull-in time and achieve a faster frequency lock.

This chapter gives a brief introduction to frequency discriminators commonly used for GPS L1 C/A signal tracking. Methods available in the literature for carrier frequency tracking of modernized GPS signals are discussed in brief, including the use of a pilot channel. The purpose of this chapter is to understand the issues and provide a detailed performance analysis of joint data/pilot frequency tracking using a weighted combination of discriminators. The analysis presented in this chapter is utilized as a precursor for designing joint data/pilot carrier phase tracking algorithms described in Chapters 5 and 6. The following are considered the contributions of this chapter:

- i. Detailed analysis of the issues in using the weighted combination of discriminators for joint data/pilot frequency tracking;
- ii. Application of a variance estimator, proposed by Moir (2001), to overcome one issue of weighted discriminator combination;
- iii. Evaluation of different possible weighted combinations of frequency discriminators based on their jitter performance and tracking threshold. Further, a  $C/N_0$  threshold is determined, above which weighted combinations of discriminators can provide a jitter reduction as compared to an FLL using the pilot channel only.

#### 4.1 FLL Theory

A description of frequency discriminators widely used in the context of GNSS signal tracking (Kaplan 2006) is provided in this section. The effect of thermal noise is not considered in the analysis presented in this section in order to better understand the working principles of a frequency discriminator. The GPS signal without a noise component at IF can be represented in analog form as

$$S(t) = A d(t)c(t - \tau_0) \exp(j(\omega_0 t + \phi_0)) \quad (4.1)$$

where  $A$  is the signal amplitude,  $d(t)$  is the navigation data bit,  $c(t)$  is the spreading code,  $\tau_0$  is the code phase delay, and  $\omega_0$  and  $\phi_0$  are the signal frequency and phase offsets. The  $\omega_0$  of a down-converted signal consists of two components: the known intermediate frequency ( $\omega_{IF}$ ), and the Doppler frequency due to user-satellite relative motion ( $\omega_d$ ). The uncertainty in the Doppler frequency is in the order of  $\pm 5$  kHz for static users. This is narrowed down to the size of a frequency bin by signal acquisition algorithms, where the frequency bin size is normally chosen as  $2/3T_{coh}$  (Van Dierendonck 1995).  $T_{coh}$  is the predetection interval, or the period over which the correlator output is coherently accumulated. This estimate of the Doppler frequency ( $\hat{\omega}_d$ ) from the acquisition stage, along with  $\omega_{IF}$ , is used to initiate the local carrier generator. The locally generated signal ( $S_r$ ) is given by

$$S_r(t) = c(t - \hat{\tau}) \exp(j(\hat{\omega}t + \phi_r)) \quad (4.2)$$

where  $\hat{\tau}$  is the code phase estimate and  $\hat{\omega} = \omega_{IF} + \hat{\omega}_d$  is the frequency estimate.  $\phi_r$  represents the initial phase offset of  $S_r(t)$ . The phase, frequency, and code phase errors ( $\Delta\phi$ ,  $\Delta\omega$ , and  $\Delta\tau$  respectively) are given as

$$\Delta\phi = \phi_0 - \phi_r, \quad \Delta\omega = \omega_0 - \hat{\omega}, \quad \Delta\tau = \tau_0 - \hat{t}. \quad (4.3)$$

The incoming signal is correlated with the reference signal and accumulated over  $T_{coh}$ . Let  $t_k - t_{k-1} = T_{coh}$  be the time interval over which the signal is coherently integrated. Then the accumulated correlator output at  $t_k$  is given by

$$Y_k = I_k + jQ_k = \frac{1}{T_{coh}} \int_{t_{k-1}}^{t_k} S(t) S_r^*(t) dt \quad (4.4)$$

where \* represents complex conjugation. The accumulated correlator output ( $Y_k$ ) can be represented in terms of its in-phase ( $I_k$ ) and quadrature ( $Q_k$ ) components. Assuming that the integration in Eq.(4.4) is performed within a data bit period, i.e.,  $d(t) = d_k$  ( $d_k \in \{-1, +1\}$ ) is constant over the interval  $t_{k-1} \leq t \leq t_k$ , and assuming perfect code synchronization ( $\Delta\tau = 0$ ), the accumulated correlator output is given by (Van Dierendonck 1995)

$$Y_k = A d_k \text{sinc}(\Delta f T_{coh}) \exp\left(j\left(\Delta\omega \left[t_{k-1} + \frac{T_{coh}}{2}\right] + \Delta\phi\right)\right) \quad (4.5)$$

where  $\text{sinc}(x) = \frac{\sin \pi x}{\pi x}$  is the normalized sinc function, and  $\Delta f = \frac{\Delta\omega}{2\pi}$  is the frequency error in units of Hz. To remove the amplitude term present in Eq. (4.5), normalization is necessary before feeding the accumulated correlator outputs to the frequency discriminators. This normalization is normally done with respect to  $|Y_k|$  for ease of implementation. The normalized correlator output ( $\bar{Y}_k$ ) is given by

$$\bar{Y}_k = d_k \exp\left(j\left(\Delta\omega \left[t_{k-1} + \frac{T_{coh}}{2}\right] + \Delta\phi\right)\right) \quad (4.6)$$

Similarly,  $\bar{Y}_{k-1}$  represents the previous accumulated correlator output, and is given by

$$\bar{Y}_{k-1} = d_{k-1} \exp\left(j\left(\Delta\omega\left[t_{k-1} - \frac{T_{coh}}{2}\right] + \Delta\phi\right)\right) \quad (4.7)$$

where  $d(t) = d_{k-1}$  for  $t_{k-2} \leq t \leq t_{k-1}$ . Further,  $\hat{\omega}$  and  $\omega_0$  are assumed to be constant over the integration intervals in Eq.(4.6) and Eq.(4.7), and hence  $\Delta\omega$  is assumed to be constant as well.

The cross product discriminator, which makes use of the current and previous accumulated correlator outputs to derive the frequency error estimate, is shown in Figure 4-1.

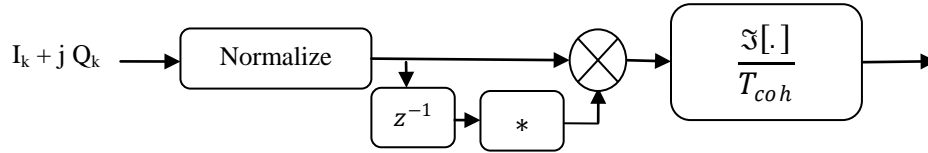


**Figure 4-1: Cross product frequency discriminator**

The discriminator output  $D_{cross}(t)$  is given by

$$D_{cross}(k) = \frac{\Im[\bar{Y}_k \bar{Y}_{k-1}^*]}{T_{coh}} \quad (4.8)$$

where  $\Im[.]$  represents the imaginary part. If the two accumulated correlator outputs belong to the same data bit period ( $d_k = d_{k-1}$ ), then the cross product discriminator output is

$$D_{cross}(k) = [2\pi \text{sinc}(2\Delta f T_{coh})] \Delta f = k_d(\Delta f, T_{coh}) \Delta f \quad (4.9)$$

where  $k_d(\Delta f, T_{coh})$  is the gain of the frequency discriminator and varies as a function of the frequency error and the predetection interval. Figure 4-2 shows a plot of the cross product discriminator gain as a function of input frequency error for three different choices of  $T_{coh}$ . For the frequency discriminator to provide a valid estimate of frequency

error, the gain has to be positive, i.e. the input frequency error should be within the main lobe of the *sinc* function in Figure 4-2 (Ling 1996). For example, if a predetection interval of 1 ms is chosen, the frequency pull in range of the cross product discriminator is  $\pm 500$  Hz, whereas it is limited to  $\pm 50$  Hz for a predetection interval of 20 ms. Thus, the maximum predetection interval chosen for carrier frequency tracking depends on the accuracy of the frequency estimate provided by the acquisition stage. Another important factor, which is evident from the gain curve, is the presence of zero-gain,  $k_d(\Delta f, T_{coh}) = 0$ , for non-zero frequency errors. This implies the possibility of false lock in carrier frequency tracking when  $k_d(\Delta f, T_{coh})$  approaches zero-gain. The tracking error variance of an FLL using cross product discriminator can be found in Natali (1986).

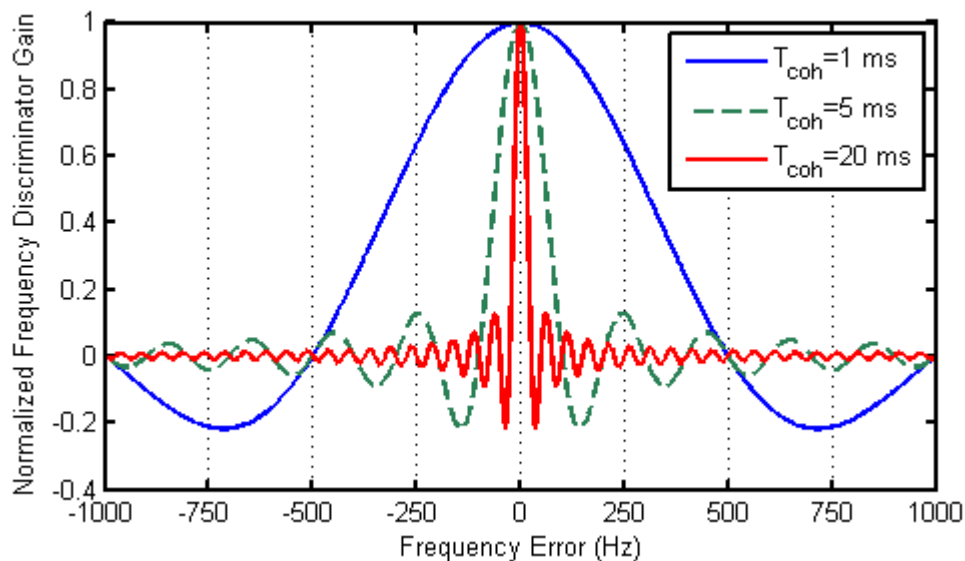


**Figure 4-2: Normalized cross product frequency discriminator gain**

Another possible frequency discriminator is the four-quadrant arctangent discriminator (ATAN2). The ATAN2 discriminator is given by

$$D_{ATAN2}(k) = \frac{\text{atan2}(\Im(\bar{Y}_k \bar{Y}_{k-1}^*), \Re(\bar{Y}_k \bar{Y}_{k-1}^*))}{T_{coh}} \quad (4.10)$$

ATAN2 provides unity gain as shown in Figure 4-3. ATAN2 is the maximum-likelihood estimator (MLE) for the phase from the differentiated accumulated correlator output ( $\bar{Y}_k \bar{Y}_{k-1}^*$ ), which corresponds to the frequency error in  $\bar{Y}_k$  (Kaplan 2006). For the same  $T_{coh}$ , the main lobe width of the ATAN2 discriminator gain curve is the same as that of the cross product discriminator. In other words, both cross product and ATAN2 frequency discriminators have a single-sided frequency pull-in range equal to half the pre-detection bandwidth ( $1/2T_{coh}$ ).

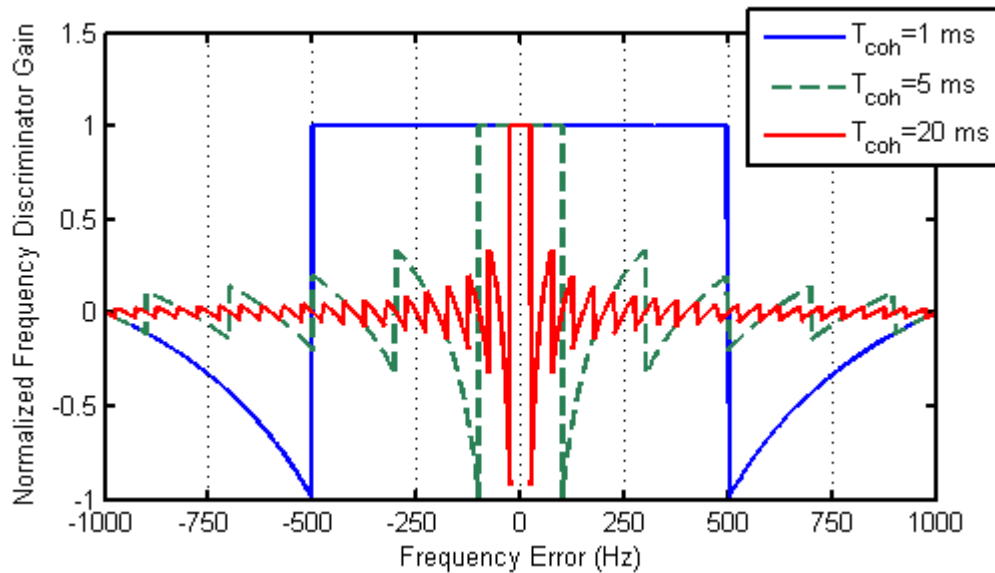


**Figure 4-3: Normalized four-quadrant arctangent (ATAN2) discriminator gain**

When the utilized accumulated correlator outputs belong to different data bit periods ( $d_k \neq d_{k-1}$ ), then the cross product discriminator output is given as

$$D_{cross}(k) = d_k d_{k-1} [2\pi \text{sinc}(2\Delta f T_{coh})] \Delta f. \quad (4.11)$$

To remove the effect of the data bit sign change ( $d_k d_{k-1}$ ), the cross product output ( $\Im[\bar{Y}_k \bar{Y}_{k-1}^*]$ ) is multiplied by the sign of the dot product output ( $\Re[\bar{Y}_k \bar{Y}_{k-1}^*]$ ) (Natali 1986). This is referred to as the cross product discriminator with decision feedback ( $D_{df}$ ), given by

$$D_{df}(k) = \frac{\text{sgn}(\Re[\bar{Y}_k \bar{Y}_{k-1}^*]) \Im[\bar{Y}_k \bar{Y}_{k-1}^*]}{T_{coh}} \quad (4.12)$$

where  $\text{sgn}(x)$  denotes the sign function that extracts the sign of a real number  $x$ , i.e.

$$\text{sgn}(x) = \begin{cases} -1 & x < 0 \\ 0 & x = 0 \\ +1 & x > 0 \end{cases} \quad (4.13)$$

For  $\text{sgn}(\Re[\bar{Y}_k \bar{Y}_{k-1}^*])$  to produce the exact effect of  $d_k d_{k-1}$ , the following condition must be met:

$$\begin{aligned} \text{sgn}[\Re[\bar{Y}_k \bar{Y}_{k-1}^*]] &= \text{sgn}[d_k d_{k-1} \cos(\Delta\omega T_{coh})] \\ &= d_k d_{k-1} \quad \text{if } |\Delta f| < \frac{1}{4T_{coh}}. \end{aligned} \quad (4.14)$$

Thus, the frequency pull-in range of  $D_{df}$  for a given predetection interval, as shown in Figure 4-4, is half that of  $D_{cross}$  and  $D_{ATAN2}$ . The noise performance of the cross product discriminator with decision feedback is given by Natali (1986).

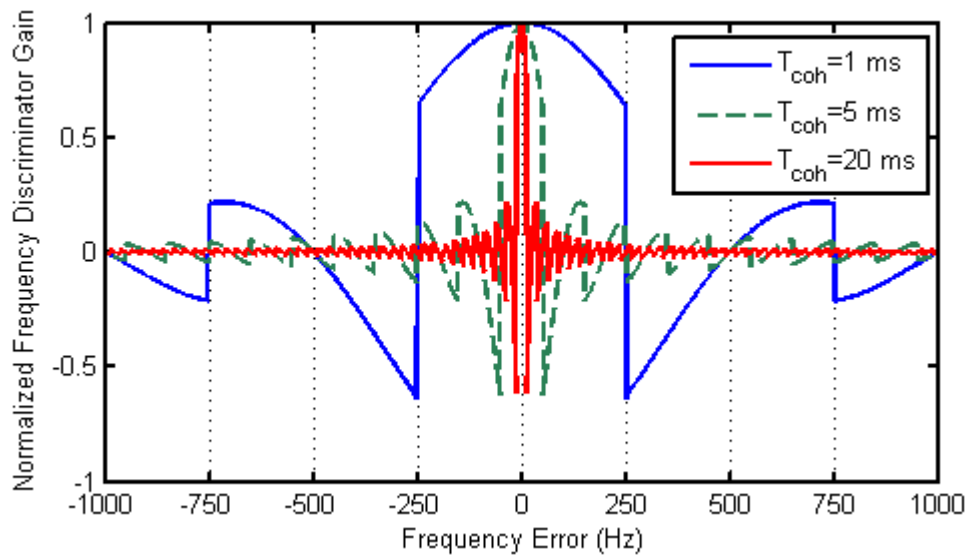


**Figure 4-4: Normalized cross product with decision feedback discriminator gain**

#### 4.2 Joint Data/Pilot Tracking

The frequency discriminators mentioned in Section 4.1 use information (accumulated correlator outputs) from either the data or pilot channel. However, both data and pilot channels undergo identical phase and frequency shifts. Further, the receiver noise processes corrupting the accumulated correlator outputs of data and pilot channels are statistically independent for the following reasons:

- i. Use of time-multiplexed data and pilot channels. For example, GPS-L2C signal carries time-multiplexed data (CM+CNAV) and pilot (CL) channels on a single carrier component.
- ii. Use of orthogonal carrier components for data and pilot channels. GPS-L5 signal carries data and pilot channels in phase quadrature.
- iii. Cross correlation properties of the spreading codes used in data and pilot channels. Noise that enters the data channel and pilot channel

accumulators are spread by their respective codes before accumulation. Hence, the noise cross-correlation between the accumulated correlator outputs of both data and pilot channels depends on the cross-correlation properties of the spreading codes (Van Dierendonck et. al. 1992).

Thus, frequency discriminators operating on the data and pilot channels evaluate estimates of the same frequency error, but those estimates are corrupted by independent noise processes. Hence, it is advantageous to combine the two frequency discriminator outputs.

A weighted combination of data and pilot discriminator outputs has been suggested by Tran & Hegarty (2002). The weights are calculated based on the noise variance of the discriminator outputs. Further, the weights should be normalized in order to preserve the frequency error in the combination. Let  $\sigma_D^2$  and  $\sigma_P^2$  be the noise variances of the data and pilot channel discriminator outputs. The weights  $w_D$  and  $w_P$  are calculated based on the following constraints:

$$w_D \propto \frac{1}{\sigma_D^2}, \quad w_P \propto \frac{1}{\sigma_P^2} \quad (4.15)$$

$$w_D + w_P = 1 \quad (4.16)$$

where  $w_D$  and  $w_P$  are the weights applied to the data and pilot channel discriminator outputs respectively. The weights  $w_D$  and  $w_P$  are computed as follows:

$$w_D = \frac{\sigma_P^2}{\sigma_D^2 + \sigma_P^2}, \quad w_P = \frac{\sigma_D^2}{\sigma_D^2 + \sigma_P^2}. \quad (4.17)$$

Other factors that need to be considered while combining data and pilot channels for frequency tracking are:

i. *Choice of discriminator on pilot channel* - Since the decision feedback discriminator operating on a data channel has a reduced frequency pull-in range as compared to other discriminators, the initial frequency error needs to be resolved within the frequency pull-in range of the decision feedback discriminator in order to enable reliable joint data/pilot tracking.

ii. *Discriminator gain variation* – Both cross product and decision feedback discriminators have the same gain for  $|\Delta f| < 1/4T_{coh}$  under moderate-to-high  $C/N_0$ . But ATAN2 provides a unity gain. This difference in gain needs to be accounted for during the combination. Since the interest of this work is in measuring the steady state noise variance of FLL, the gain from the cross product and decision feedback discriminators can be safely approximated as unity for  $|4 \Delta f T_{coh}| \ll 1$ .

iii. *Weight estimation* – The weight calculation in Eq. (4.17) depends on  $\sigma_D^2$  and  $\sigma_p^2$ . These variances vary with  $C/N_0$  and the choice of discriminators.  $C/N_0$  of the received signal changes with the altitude and elevation of the satellite, user environment, etc. The estimates from the ATAN2 discriminator used on the pilot channel are noisier than its theoretically predicted noise variance at low  $C/N_0$  (Julien 2005). Similarly, in the data channel, the decision feedback cross product discriminator introduces data-prediction errors due to the effect of thermal noise in the decision feedback process (Natali 1986). This data-prediction error increases as the  $C/N_0$  drops. Thus, fixing the weights based on theoretical equations is not valid for low  $C/N_0$ . There is a need to compute  $\sigma_D^2$  and  $\sigma_p^2$  “on the fly” in order to weight the discriminator outputs based on their variance.

### 4.3 On-The-Fly Variance Estimation

In this work, the variance estimation loop as proposed by Moir (2001) is used to estimate the noise variance at the discriminator output. The block diagram of the variance estimation loop (Figure 4-5) and a brief analytical explanation of its functioning are repeated here for completeness.

The variance estimation loop, as shown in Figure 4-5, has two closed loops arranged in sequence. The first loop accepting a zero-mean input signal ( $f_i(t)$ ), whose variance needs to be estimated, produces an output signal ( $y(t)$ ) with variance inversely equal to that of the input i.e.,  $E[y^2(t)] \approx \frac{1}{E[f_i^2(t)]}$ . The second loop is used to compute  $E[f_i^2(t)]$  by computing the inverse of  $E[y^2(t)]$ . Thus, the loops together serve as a variance estimator.

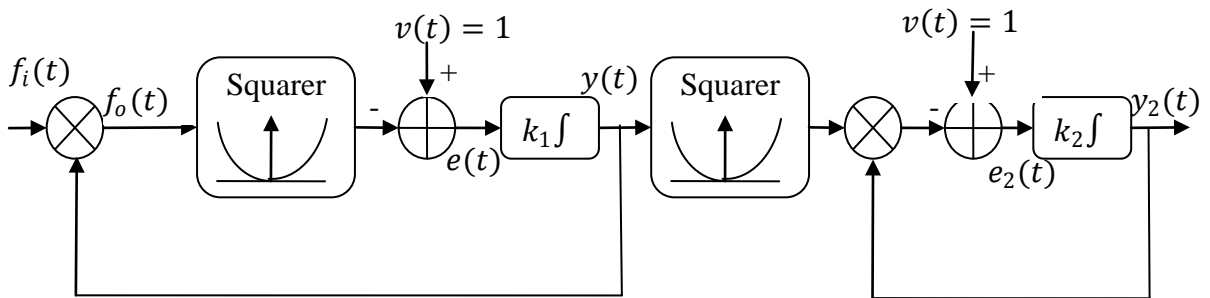


**Figure 4-5: Block diagram of Variance Estimation Loop (Moir 2001)**

The other input to the loops includes a scaling factor,  $v(t)$ , for the noise variance to be estimated. This is set to unity as no scaling is required. The operation of the loops can be explained as follows: the closed-loop system response of the first loop is given as

$$\frac{1}{k_1} \frac{dy(t)}{dt} = v(t) - (f_i(t)y(t))^2 \quad (4.18)$$

where  $k_1$  is the gain of the integrator. For  $k_1 \gg 1$ ,

$$v(t) \approx (f_i(t)y(t))^2 = f_o^2(t) \quad (4.19)$$

where  $f_o(t)$  is the multiplier output as shown in Figure 4-5. With the assumption that  $y(t)$  is statistically independent of  $f_i(t)$ ,  $E[f_o^2(t)]$  is given by

$$E[f_o^2(t)] = E[f_i^2(t)] E[y^2(t)] \approx E[v^2(t)] = 1 \quad (4.20)$$

$$E[f_i^2(t)] \approx \frac{1}{E[y^2(t)]}. \quad (4.21)$$

From Eq.(4.21), the variance of the input signal is inversely related to the mean-square value of  $y(t)$ . The second loop is used to replace the division in Eq. (4.21) and hence, accepts  $y^2(t)$  as the input and gives the output signal as  $y_2(t) = E[f_i^2(t)]$ , which is the variance estimate.

The discriminator output ( $D(k)$ ) is fed as an input signal to the variance estimation loop. To meet the requirements of the variance estimator, the mean of the input signal should be removed. This is accomplished by using an exponential filter with a weight ( $\beta$ ):

$$\mu(k) = \beta\mu(k-1) + (1-\beta)D(k). \quad (4.22)$$

For this application,  $\beta = 0.95$  was found to fit well, based on trial and error. This estimated mean is removed from  $D(k)$  before it is fed to the variance estimation loop.

The variance estimation loop, implemented at the output of frequency discriminators, is validated with live as well as simulated signals, the simulated signals being generated by a Spirent GPS simulator (GSS7700). Figure 4-6 shows the output of the variance estimation loop for a sample run on a data set collected from the Spirent GPS simulator. The simulator is configured to generate a 35 dB-Hz L2C signal at start and the signal power is reduced in known steps of 1.5 dB every minute. The data is 1-bit

quantized complex samples (1 bit I and 1 bit Q) collected at a sampling rate of 2.5 MHz. The receiver is configured to use a predetection interval of 5 ms, an FLL noise bandwidth ( $B_n$ ) of 4 Hz, and a DLL noise bandwidth of 2 Hz. The FLL and DLL are allowed to run over the entire available data set without switching to phase tracking mode. The decision-directed cross product discriminator is used in the data channel, and ATAN2 is used in the pilot channel. As shown in Figure 4-6, the measured standard deviations of the discriminator outputs on both data and pilot channels are identical for  $C/N_0$  greater than 32 dB-Hz. So, the discriminator outputs, corresponding to this  $C/N_0$  range, are weighted equally in the data/pilot combination. For weak signals ( $C/N_0 < 32$  dB-Hz), ATAN2 shows a larger standard deviation in the estimate as described in Section 4.2, and hence will be weighted less in the combination. Further, Figure 4-6 shows the ability of the variance estimation loop to respond to the changing  $C/N_0$ , thus allowing on-the-fly

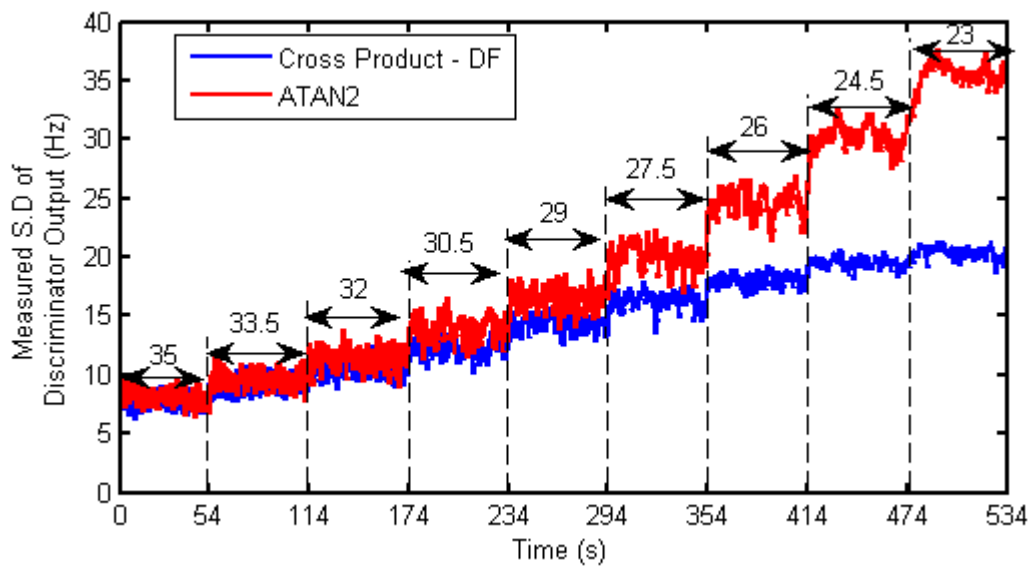


**Figure 4-6: Measured standard deviations of data and pilot channel frequency discriminator outputs. Corresponding  $C/N_0$  for each time interval is given in dB-Hz above the arrows.**

weight computations for optimum combination.

## 4.4 Results

### 4.4.1 Numerical Simulation

#### 4.4.1.1 Scenario Description

A numerical simulation is run in order to compare the performance attained by using different discriminators. The input signal (data and pilot channel) is generated with a constant frequency offset ( $\Delta f$ ) of 20 Hz, and an acceleration offset of  $1 \text{ Hz/s}^2$ . The former is an arbitrary frequency offset to allow the FLL to gain lock, and the latter is to test the ability of the FLL to track a signal with maximum frequency rate as faced by a static GPS receiver (Tsui 2000). Four different FLL implementations are allowed to track the input signal simultaneously. The implementations differ by the choice of discriminator:

- i. data channel only with  $D_{df}$ ,
- ii. pilot channel only with  $D_{cross}$ ,
- iii. standard discriminator combination with  $D_{df}$  and  $D_{cross}$ , and
- iv. Costas discriminator combination with  $D_{df}$  on both data and pilot channels.

#### 4.4.1.2 Test Methodology

The noise bandwidth of all the implementations is fixed to 4 Hz for fair comparisons and the loop filters designed in the analog domain are implemented using bilinear transformations. The predetection interval is set to 5 ms. Since this is a numerical simulation, instantaneous values of original input frequency and acceleration are known. These are compared with the frequency estimates used by the local oscillator in order to

measure the average frequency error of each predetection interval. A total of 3000 such frequency error values, measured in steady state, are then used to compute the frequency jitter due to thermal noise ( $\sigma_{thermal}$ ) and the steady-state error ( $\Delta f_{ss}$ ). As defined by Kaplan (2006), frequency lock is declared if the frequency jitter ( $\sigma_{net}$ ) satisfies the condition

$$3\sigma_{net} = 3\sigma_{FLL} + \Delta f_{ss} \leq \frac{1}{4T_{coh}} \text{ (Hz)} \quad (4.23)$$

where the threshold of  $\frac{1}{4T_{coh}}$  corresponds to the pull-in range of the cross product discriminator with decision feedback ( $D_{df}$ ). Although the pull-in range of the cross product discriminator ( $D_{cross}$ ) is twice as that of  $D_{df}$ , this threshold is chosen based on the minimum pull-in range in the combination. For statistical reliability of the results,  $\sigma_{thermal}$  and  $\Delta f_{ss}$  are averaged across 100 such independent runs of the FLL for each considered  $C/N_0$ . For each run, the FLL transient is allowed to settle, and the errors are measured at steady state. Only those points that have a probability of frequency lock of at least 75% for a given  $C/N_0$  are used in the analysis. The frequency jitter is measured for a  $C/N_0$  in the 15 to 40 dB-Hz range.

#### 4.4.1.3 Analysis of Results

Figure 4-7 shows the simulation results. For  $C/N_0$  greater than 33 dB-Hz, the performance of  $D_{cross}$  on the pilot channel and  $D_{df}$  on the data channel are the same. Data bit predictions are more reliable under this situation; hence, there is no significant difference in performance. Under these  $C/N_0$  conditions, the standard and Costas discriminator combination provides a 3 dB noise variance reduction.

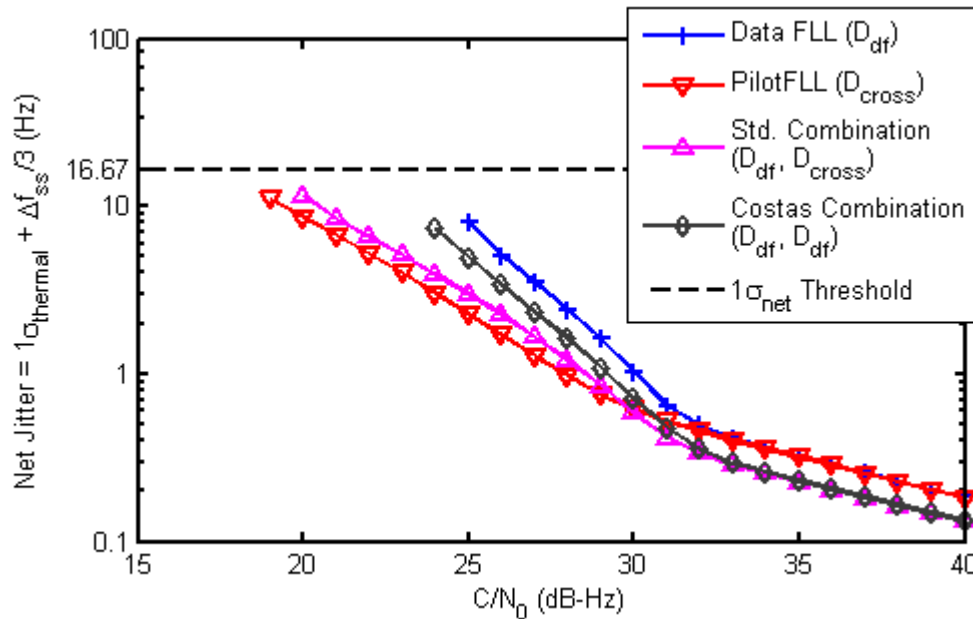


**Figure 4-7: Comparison of frequency jitter across different implementations to track data and pilot channels**

For  $C/N_0$  lower than 33 dB-Hz, increased noise is introduced by the data bit decision process (Natali 1986). This is observed on the curve corresponding to the FLL on the data channel ( $D_{df}$ ). The Costas discriminator combination, which suffers from the same drawback, continues to provide nearly a 3 dB noise variance reduction with respect to  $D_{df}$ . The standard discriminator combination shows a slightly degraded performance in comparison with the pilot channel only for low  $C/N_0$ . The reason for this degradation in performance is explained by analyzing the noise performance of  $D_{df}$  used in the combination.

The  $D_{df}$  relies on a differential data bit decision ( $sgn(\Re[.])$ ) to account for the effect of the data bit presence. The noise ( $\epsilon(t)$ ) introduced by the data bit decision part of the discriminator can be given by a model approximated to the first order as (Natali 1986):

$$\epsilon(t) = E[\epsilon(t)] + \epsilon_1(t) = (1 - 2P_e) + \epsilon_1(t) \quad (4.24)$$

$$P_e = \frac{1}{2} \exp\left(-\frac{C}{N_0} T_{coh}\right) \quad (4.25)$$

where  $P_e$  is the probability of data bit error ( $P_e$ ),  $E[\epsilon(t)] = (1 - 2P_e)$  accounts for the change in discriminator gain due to data bit errors, and  $\epsilon_1(t)$  accounts for the noise introduced by faulty decisions. The autocorrelation function ( $R_{\epsilon_1}(\tau)$ ) of  $\epsilon_1(t)$  is given by (Natali 1986):

$$R_{\epsilon_1}(\tau) = \begin{cases} 2P_e \left[ 2(1 - P_e) - \left| \frac{\tau}{T_{coh}} \right| \right] & 0 < \tau < T_{coh} \\ 2P_e(1 - 2P_e) \left[ 2 - \left| \frac{\tau}{T_{coh}} \right| \right] & T_{coh} < \tau < 2T_{coh} \\ 0 & otherwise \end{cases} \quad (4.26)$$

Although the difference in noise variance at the discriminator output of  $D_{df}$  and  $D_{cross}$  in a standard combination is accounted for by the weighting approach, the change in gain across  $D_{df}$  and  $D_{cross}$  at lower  $C/N_0$ , as given by  $E[\epsilon(t)]$  in Eq.(4.24), is unaccounted for in the combination. Hence, a difference in performance is observed.

In terms of the minimum  $C/N_0$  required for tracking, as observed from Figure 4-7, the pilot channel has a frequency tracking threshold that is 6 dB lower than the data channel. The standard discriminator combination performs quite close (1 dB difference in minimum required  $C/N_0$ ) to the pilot-channel-only frequency tracking, whereas the Costas discriminator combination performs close to the data-channel-only frequency tracking.

## 4.4.2 Validation of Results with Live Signals

### 4.4.2.1 Test Methodology

To confirm the result shown in Figure 4-7, live data from SVN 48/ PRN 07 was collected. SVN 48 is an IIR-M satellite transmitting the L2C signal along with the L1 C/A signal. In this case, true Doppler values will not be available to compute the frequency jitter as before. The data collection setup shown in Figure 4-8 is used to overcome this difficulty. Live signals are collected when the satellite is at an elevation greater than  $60^{\circ}$ . This ensures a high  $C/N_0$  signal (greater than 40 dB – Hz). The signal from the antenna/LNA assembly is then passed through a power splitter. One output of the power splitter is treated as a reference signal and the other output is passed through a digital attenuator. Both channels are then amplified independently, and the down-converted IF samples are logged synchronously using a National Instruments (NI) front-end at a sampling rate of 5 MHz (NI PXI-5661 2006). As described in Chapter 2, the results of signal acquisition are then passed to a modified version of GSNRx<sup>TM</sup> for signal

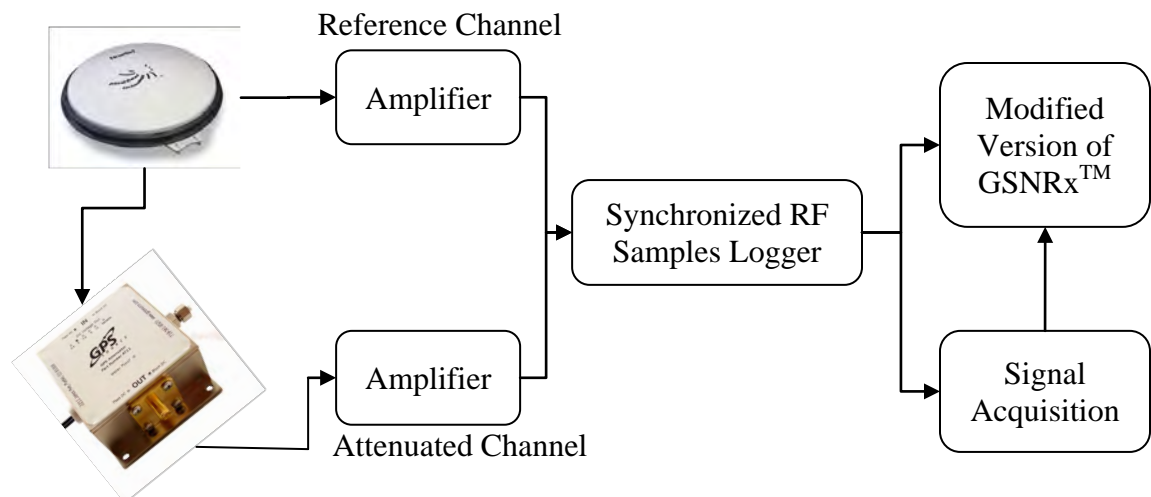


**Figure 4-8: Block diagram of data collection and processing setup**

tracking (Petovello et al 2008).

The attenuation level on the digital attenuator is gradually increased in known steps at known intervals. The time interval between every attenuation level change is fixed at approximately 60 seconds. For  $C/N_0$  less than 18 dB-Hz, this interval is increased to 120 seconds for reliable analysis. Attenuation is increased in steps of 2 dB, from an initial attenuation of 9 dB, with respect to the reference channel. Since the attenuator is present only after the LNA in the RF chain, the effect of these attenuation levels on signal  $C/N_0$  is given by the Friis formula, as described in Chapter 2. Hence,  $C/N_0$  estimates measured in the receiver are used in the results. The  $C/N_0$  estimates from the attenuated and reference channel are shown in Figure 4-9. Joint data/pilot MLE with iteration as described in Chapter 3 is used for  $C/N_0$  estimation.

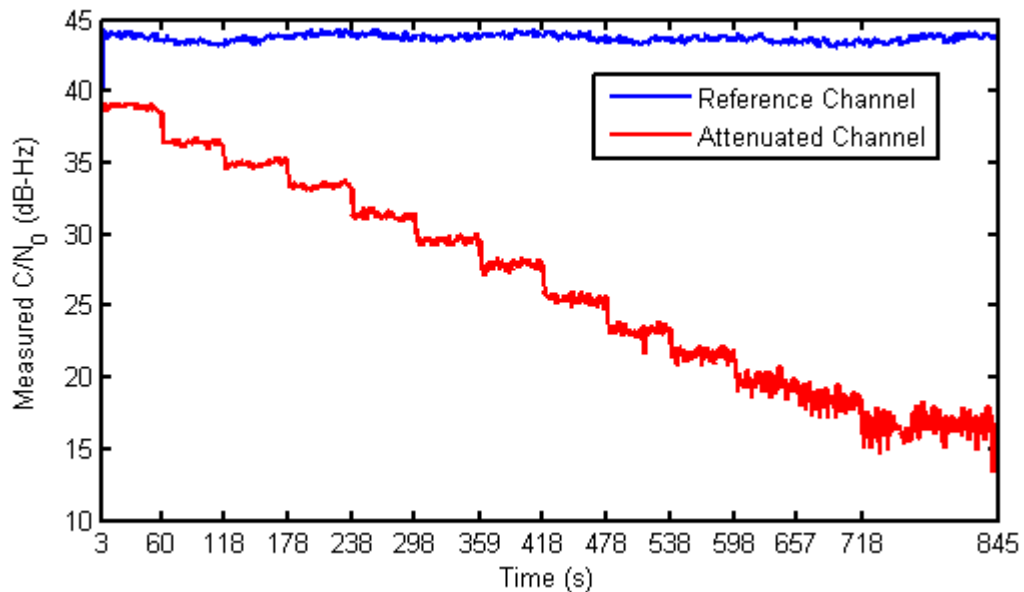


**Figure 4-9: Measured  $C/N_0$  of reference and attenuated channels**

Further, a minimum possible noise bandwidth is chosen for carrier phase tracking of the reference channel (Muthuraman et. al. 2008). This ensures minimum noise

variance in the Doppler estimates without losing lock. Later, GSNRx<sup>TM</sup> is configured to track the attenuated channel with a FLL and DLL over the entire length of the data set. The noise bandwidth of the FLL used is fixed to 4 Hz, and a predetection interval of 5 ms is adopted. These values are similar to those used in the numerical simulation performed above. A first-order polynomial is fitted to the Doppler estimates from the reference channel for every 60-second interval. A first order fit is sufficient for Doppler estimates, as the scenario under consideration is static and the dynamics experienced are only due to the satellite motion. The polynomial fitting is necessary as the phase tracking on the reference channel is updated at the end of every CM code period (20 ms), whereas in FLL tracking of the attenuated channel, the update is performed every 5 ms. Polynomial fitting helps in providing a smooth reference for Doppler estimates. The error in Doppler estimates of the attenuated channel is derived by comparing it with the reference. The frequency jitter is computed using Eq. (4.23), and the result is plotted in Figure 4-10.

#### 4.4.2.2 Analysis of Results

The results follow the same trend as obtained with the numerical simulation. The performance obtained by using  $D_{df}$  on the data channel is similar to that of  $D_{cross}$  on the pilot channel for  $C/N_0$  greater than 33 dB-Hz. Further, under these  $C/N_0$  conditions, both the standard discriminator combination and the Costas discriminator combination provide approximately 3 dB gain. Similarly, the Costas discriminator combination continues to provide a jitter reduction as compared to an FLL running on the data channel ( $D_{df}$ ), and provides a degraded performance for  $C/N_0$  less than 33 dB-Hz as compared to either a standard discriminator combination or  $D_{cross}$  running on the pilot channel only. Both the Costas discriminator combination and data-channel-only FLL lose lock for  $C/N_0$  less than

25 dB-Hz. By contrast, the standard discriminator combination performs closely to  $D_{cross}$  in terms of the minimum  $C/N_0$  required to maintain frequency tracking.

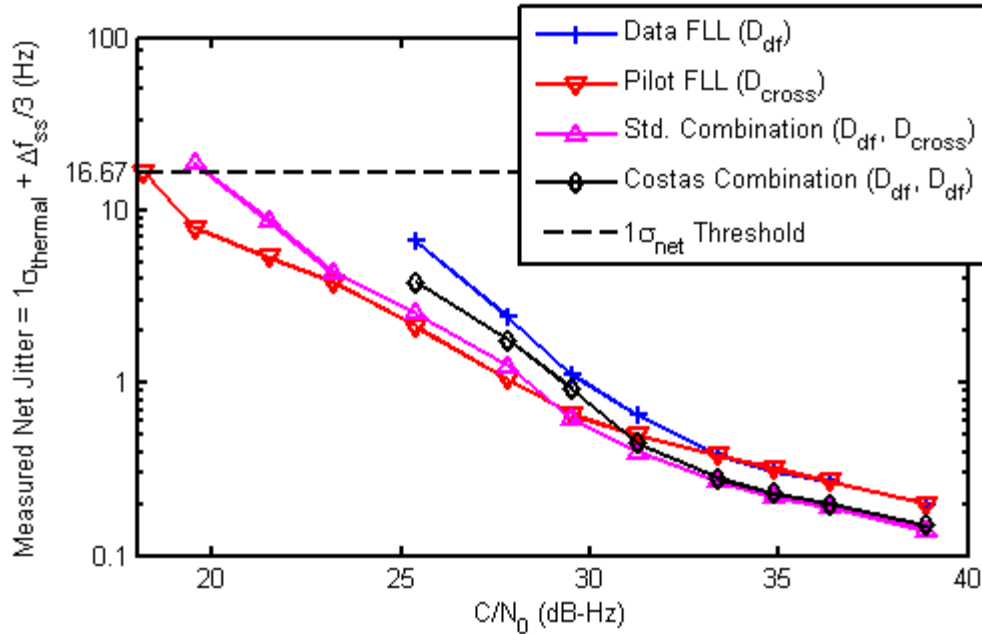


**Figure 4-10: Frequency jitter comparison across different discriminator implementations with live data for  $B_n = 4$  Hz and  $T_{coh} = 5$  ms**

Thus, in conclusion, weighted combinations of discriminators are proven to be useful for reducing the net frequency jitter only for  $C/N_0$  greater than 33 dB-Hz. This result depends on the choice of  $B_n$  and  $T_{coh}$ . For  $C/N_0$  lower than 33 dB-Hz, it is better to use a cross product discriminator on the pilot channel alone. Further, using only the pilot channel for carrier frequency tracking helps reduce the frequency tracking threshold by 6 dB, as compared to that of an FLL using only the data channel. When a standard discriminator combination is employed without an option to switch to pilot-channel-only FLL tracking for lower  $C/N_0$ , it has been shown that the degradation in  $\sigma_{net}$  is minimal for  $C/N_0$  less than 30 dB-Hz.

## CHAPTER FIVE: METHODS FOR JOINT DATA/PILOT CARRIER PHASE TRACKING

Joint data/pilot tracking is not straight-forward, most of all for carrier phase tracking. The inherent advantages of using a pure phase locked loop (PLL) on the pilot channel alone risk to be lost when including the data channel in the loop design. One of the advantages of using a pure PLL is its ability to track weaker signals, corresponding to a lower tracking threshold (Kaplan 2006). Tracking threshold is defined as the minimum required  $C/N_0$  to track the signal reliably. Reliable carrier phase tracking of a signal is declared when the tracking jitter stays within a threshold, which is given by one fourth of the phase pull-in range of the discriminator in use (Kaplan 2006). The  $3\sigma_{PLL}$  rule can be stated as

$$3\sigma_{PLL} = 3\sqrt{\sigma_{thermal}^2 + \sigma_v^2 + \theta_A^2} + \Delta\phi_{ss} \leq \frac{1}{4}(\text{Phase pull - in range}) \quad (5.1)$$

where  $\sigma_{thermal}^2$  is the tracking jitter due to thermal noise,  $\sigma_v^2$  is the variance induced by vibrations,  $\theta_A^2$  is the oscillator jitter induced by the Allan variance, and  $\Delta\phi_{ss}$  is the error due to dynamic stress. The motivation of this chapter is to design tracking algorithms which use both data and pilot channels to improve the tracking performance without a significant loss in tracking sensitivity. The components of tracking jitter induced by the oscillator ( $\sigma_v^2$  and  $\theta_A^2$ ) are not considered in the design of joint data/pilot tracking algorithms, as their impact will be similar on both single channel (data or pilot) and joint data/pilot tracking. Hence, neglecting these contributions to the tracking jitter, Eq. (5.1) becomes

$$\sigma_{PLL} = \sigma_{thermal} + \frac{\Delta\phi_{ss}}{3} \leq \frac{1}{12}(\text{Phase pull - in range}). \quad (5.2)$$

The following are considered contributions of this thesis toward the design of joint data/pilot tracking algorithms:

- i. A detailed analysis of joint data/pilot carrier phase tracking algorithms using a weighted combination of discriminators;
- ii. Two novel methods for combining data and pilot channel information for carrier phase tracking without significantly compromising the advantages gained by using a pure PLL;
- iii. An adaptive noise bandwidth tuning algorithm, whose design is carried out using both analog and digital design procedures;
- iv. A detailed performance analysis of the proposed methods.

The chapter starts with an overview of carrier phase discriminators and provides a brief review of the existing literature for joint data/pilot tracking. A justification for choosing the weighted combination of discriminators for joint data/pilot tracking will be provided, along with the issues associated with these types of loops. As an extension of the weighted discriminator combination architecture, a way to use four-quadrant arctangent discriminators on both data and pilot channels will be given, with emphasis on the possible advantages of such a combination. The above algorithms were proposed as modifications of the standard tracking architecture described in Chapter 2. The standard tracking architecture is further extended to include an adaptive bandwidth tuner that selects the loop bandwidth depending on the noise and dynamic conditions. Another possibility, based on the use of an extended Kalman filter (EKF), for joint data/pilot tracking, will be presented.

## 5.1 Phase Discriminator Overview

As described in Chapter 2, a standard tracking architecture consists of a phase discriminator (or phase error estimator), a loop filter and a numerically controlled oscillator (NCO). The choice of phase discriminator makes the loop a Costas loop (for the data channel) or a pure PLL (for the pilot channel). Discriminators used in a Costas loop are insensitive to the presence of data bits with a  $\pm\pi$  ambiguity in phase tracking. Costas loop discriminators also have a reduced phase-pull-in region as compared to pure PLL phase discriminators. Examples of Costas discriminators are given in Table 5-1 (Kaplan 2006).

**Table 5-1: Costas Loop Discriminators**

Discriminator Type	Output Phase Error
$Q \times I$	$\sin(2\Delta\phi)$
$Q \times \text{Sign}(I)$	$\sin(\Delta\phi)$
$\frac{Q}{I}$	$\tan(\Delta\phi)$
$ATAN\left(\frac{Q}{I}\right)$	$\Delta\phi$

Pure PLL phase discriminators can operate only on dataless channels (pilot channels), as they are sensitive to the data bits. Rather, they have an extended pull-in region that aids weak signal tracking. Pure PLL tracking has a 6 dB higher tracking sensitivity with respect to Costas loops (Kaplan 2006). A typical pure PLL phase discriminator is the four quadrant arctangent (ATAN2).

In this work, ATAN and ATAN2 will be used as Costas and the pure PLL discriminators, respectively. The motivations for this choice are as follows:

- i. ATAN is the maximum-likelihood phase estimator for data channel observations; similarly, the ATAN2 is the maximum-likelihood phase estimator on pilot channel observations.
- ii. The two discriminators have a linear relationship between input phase error and control signal provided to the loop.
- iii. Both discriminators have equal gain in the  $\pm \frac{\pi}{2}$  input phase error range. This helps avoiding biases in the estimates when a weighted combination of their output is used.

On the other hand, both ATAN and ATAN2 discriminators require the highest computational burden and are normally implemented in hardware receivers using lookup tables (Kaplan 2006). In this work, tracking is performed in post-processing, using a software receiver. Hence, a direct implementation of the arctangent discriminator is used.

## 5.2 Literature Review

Different methods have been proposed in the literature to effectively exploit the pilot channel available in new GNSS signals. Data-pilot combinations can be performed at different stages in a receiver, mostly after accumulating the correlator outputs. One possible option is to combine the data and pilot channel accumulated correlator outputs based on the maximum power constraint (Mongrédien et al 2006), as

$$Y_{k,dp} = \begin{cases} Y_{k,pilot} + Y_{k,data} , & |Y_{k,pilot} + Y_{k,data}| \geq |Y_{k,pilot} - Y_{k,data}| \\ Y_{k,pilot} - Y_{k,data} , & |Y_{k,pilot} - Y_{k,data}| > |Y_{k,pilot} + Y_{k,data}| \end{cases} \quad (5.3)$$

where  $Y_{k,data}$  and  $Y_{k,pilot}$  are the complex accumulated correlator outputs at the  $k^{\text{th}}$  instant on the data and pilot channels, respectively. The combined accumulated correlator output,  $Y_{k,dp}$ , will be used for further processing in the tracking channel. Here the data bit

is accounted for by the hard decision approach, whose reliability is limited by the bit-error-rate (BER) at lower  $C/N_0$ .

Another possible option is allowing the data and pilot channel accumulated correlator outputs to pass through their respective discriminators and use a weighted combination of discriminator outputs as the estimate of error, as described in Chapter 4 (Hegarty 1999). Weights, inversely proportional to the discriminator output noise variance, are used and hence the resulting phase combination is optimal in the sense that the variance of the discriminator output after combination is minimized. However, as for the carrier frequency tracking considered in Chapter 4, this method is not straightforward to implement and the following issues are of concern:

- i. Identical predetection intervals ( $T_{coh}$ ) will be assumed across channels in order to reduce the implementation complexity of the algorithm. However, an alternative option to overcome this limitation is given in Tran & Hegarty (2002) and Ries et al (2002).
- ii. The second limitation arises from the choice of the discriminators. As described in Section 5.1, only Costas discriminators account for the data bit presence. So the obvious option is to use a Costas discriminator on both channels. However, the inherent advantages of using a pure PLL are lost in such a formulation. The other possible option is to use a Costas discriminator on the data channel and a pure PLL discriminator on the pilot channel. The critical problem to be addressed in this case is the difference in the discriminator pull-in regions. The phase pull-in range of a Costas discriminator is  $\pm \frac{\pi}{2}$ , whereas a pure PLL discriminator has a pull-

in range of  $\pm\pi$ . Methods to detect and/or compensate for phase jumps in the data channel, due to the presence of dynamics or low  $C/N_0$ , can be found in Ries et al (2002), Tran & Hegarty (2002) and Julien (2005). Here again the performance depends on the reliability of the decision algorithms for low  $C/N_0$ .

- iii. Further, the noise variance of the arctangent discriminators (ATAN and ATAN2 ) deviates considerably (Julien 2005) from the theoretical values at low  $C/N_0$ , thus rendering any pre-calculated weights to be incorrect. In this work, as described in Chapter 4, this problem is solved by using on-the-fly weight estimation.

The methods available in the literature for joint data/pilot tracking were mostly evaluated for their tracking performance under moderate-to-high  $C/N_0$  (above 25 dB-Hz), where the data bit decision errors are minimal and the results are in favor of the combination. However, Ries et al (2002) and Macabiau et al (2003) suggested tracking the pilot channel alone using a pure PLL for weak signal environments. This choice is justified by the fact that it is important to continue tracking the signal even when the  $C/N_0$  drops, and any advantage in tracking jitter reduction should be considered only after the tracking sensitivity specifications are met.

### **5.3 Motivation and Proposed Methods**

The purpose of this chapter is to design joint data/pilot tracking algorithms, which provide reduced tracking jitter without losing the advantages of pilot channel only tracking (using a simple pure PLL) in terms of tracking sensitivity. Toward attaining this

goal, two different methods are proposed and analyzed for their performance under weak signal conditions. They are:

- i. Utilizing four-quadrant arctangent discriminators on both data and pilot channels, after accounting for the data bit presence on data channel. An adaptive noise bandwidth tuner is also used to adjust the loop parameters depending on thermal noise and dynamic conditions.
- ii. Using a Kalman filter based tracking architecture for joint data/pilot tracking.

The first method is proposed as an extension to the weighted discriminator combination approach described in Section 5.2, and hence uses the standard tracking architecture (discriminator, loop filter and NCO). The second method uses a Kalman filter to estimate the tracking errors directly from the accumulated correlator outputs. The tracking sensitivity and tracking jitter, which are the parameters of interest in this work, depend on the choice of noise bandwidth for the standard tracking architecture. In the case of a Kalman filter based architecture, the Kalman gain is computed by making use of the estimated  $C/N_0$ ,  $T_{coh}$  and predicted trajectory (dynamics). Thus, it can be considered an equivalent of adaptive noise bandwidth tuning based on thermal noise level and dynamic stress (O'Driscoll & Lachapelle 2009). Hence, to achieve similar performance with the two architectures, a novel yet computationally simple adaptive noise bandwidth algorithm is proposed and integrated with the standard tracking architecture. The design procedures are carried out in both the analog and digital domains, and a detailed performance analysis is provided.

## 5.4 Methods for Joint Data/Pilot Tracking

### 5.4.1 Method 1: Weighted Discriminator Combination with ATAN2 Discriminator on Both Channels

The arctangent discriminators ATAN (Costas) and ATAN2 (PLL) provide unity gain over the linear regions corresponding to input phase errors of  $\pm \frac{\pi}{2}$  and  $\pm \pi$ , respectively. But as the  $C/N_0$  decreases, the linear operating regions gradually start to degrade around their respective boundaries. This is due to the phase wrapping effect of these discriminators. As a result, the estimates become biased and also perform poorly in terms of output noise variance (Kay 1993). Under such situations, the larger the phase pull-in region/linear region, the better the chances of maintaining signal lock. Thus utilizing an ATAN2 discriminator on the data channel as well helps in reducing the bias in estimates and maintaining signal tracking. However, to use an ATAN2 discriminator on the data channel, it is necessary to account for the effect of data bit sign changes. This is accomplished by comparing the phase error estimates of the data channel with those of the pilot channel and applying a correction whenever the phase error estimate ( $\Delta\hat{\phi}_{data}$ ) on the data channel falls outside the region defined by  $(\Delta\hat{\phi}_{pilot} \pm \frac{\pi}{2})$ . The reduction of the bias in the estimates is shown in Figure 5-1 with a numerical simulation for different true phase errors ( $\Delta\phi$ ) across  $C/N_0$ . The bias degradation by using ATAN2 on the data channel (after data bit correction) is better than that of ATAN on the data channel alone. This improvement is significant for weak signals ( $C/N_0 < 25$  dB-Hz) and as  $\Delta\phi$  increases.

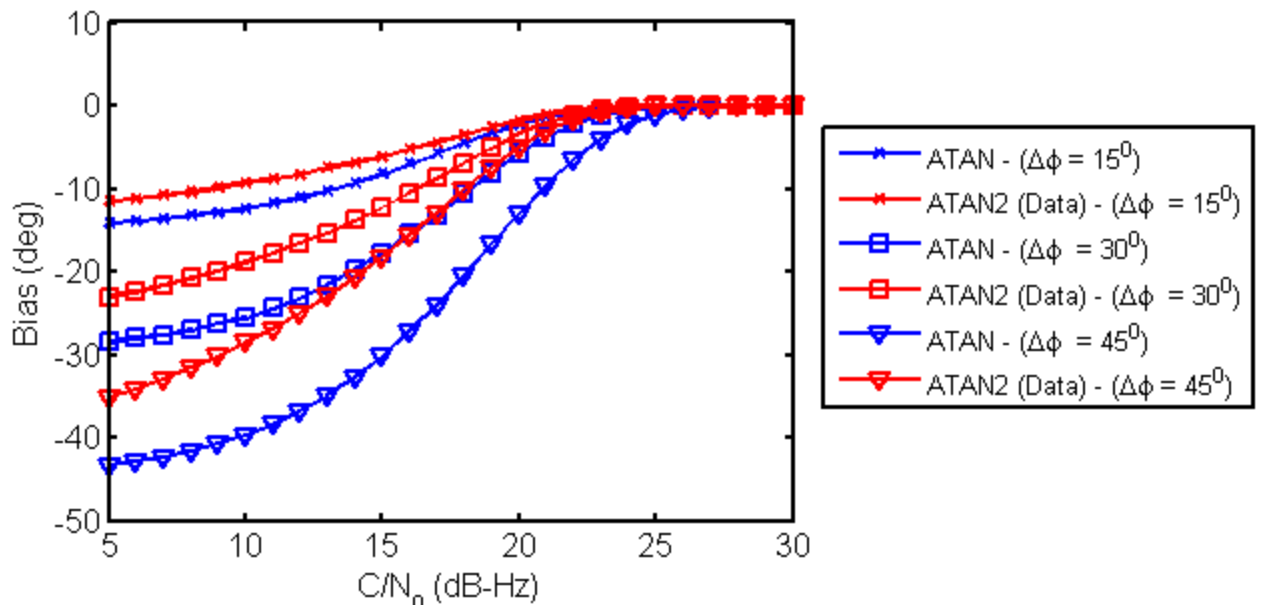


**Figure 5-1: Bias in phase error estimate using ATAN and ATAN2 (with correction for data bits) on the data channel for phase errors ( $\Delta\Phi$ ) (i)  $15^\circ$  (ii)  $30^\circ$  (iii)  $45^\circ$**

#### 5.4.2 Method 2: Kalman Filter based Joint Data/Pilot Tracking

Kalman filter (KF) based tracking has gained the attention of the navigation community (Psiaki & Jung 2002, Petovello & Lachapelle 2006, Mongrédien et al 2007) for its improved tracking performance and for the possibility to specify the noise and signal models. A Kalman filter for tracking is normally designed to accept the accumulated correlator outputs of the early, prompt, and late channels as input and to estimate the following five states as follows:

- i.  $A$  – signal amplitude
- ii.  $\Delta\tau$  – code phase error
- iii.  $\Delta\phi$  – carrier phase error
- iv.  $\Delta\omega$  – carrier frequency error
- v.  $a$  – carrier frequency drift.

In this work the standard models for state space and observations, as described in Petovello & Lachapelle (2006), are used. Design details are provided in Appendix A. A KF can be designed to accept pilot channel observations alone, and its estimates can be used to track both data and pilot channels. It is also possible to combine the accumulated correlator outputs across both channels before feeding the result to the KF. In these two cases, the observation model does not change as compared to the standard KF model described in the literature for GPS signals. This was demonstrated for the L5 signal by Mongrédien et al (2007). A similar approach can be found in Ziedan (2005) for the L2C and L5 signals. The main difference is that the former uses a hard decision based on the maximum power combining approach, whereas the latter uses ML estimation of possible data bit combinations across the predetection interval, which is chosen to be greater than 20 ms. In both methods, the KF is not used to weight the data and pilot channel observations. Thus, the performance of these techniques under weak signal environments relies on the method used to combine the accumulated correlator outputs. Any degradation in this combination will significantly degrade the performance of KF based tracking.

In this work, the data and pilot channel accumulated correlator outputs are directly passed to the Kalman filter as independent observations. This allows the KF to weight the data channel observations against that of the pilot channel. In the proposed method, the model for standard KF tracking remains the same, except for two changes: (i) the number of observations is increased to 12 (real and imaginary parts of early, prompt, and late channel accumulated correlator outputs from data and pilot channels) and (ii) the observation covariance matrix is updated accordingly.

The Kalman filter based tracking architecture described in this section makes use of the  $C/N_0$  estimates and the estimated trajectory (dynamics) in order to choose the Kalman gain. To obtain fair performance measures across standard and Kalman filter based tracking architectures, the noise bandwidth of the standard tracking architecture needs to be adaptively tuned based on the signal dynamics and thermal noise level.

## **5.5 Adaptive Bandwidth Tuning**

This section provides the design procedures for adaptive bandwidth tuning of a second order PLL. The choice of a second order system is for mathematical ease and the proposed algorithms can be extended to third order PLLs using numerical techniques. In a third order PLL the error due to dynamics is from the jerk rather than phase acceleration as in the case of a second order PLL. In a conventional GNSS receiver, the loop filter is designed in the analog domain and digitally implemented using the bilinear transform technique (Kaplan 2006). The same procedure is followed in the first stage of this work. Limitations of this technique are highlighted. In the second stage, the design is carried out directly in the digital domain by carefully modeling the effect of thermal noise and dynamic stress. The algorithm proposed for bandwidth tuning is general, and can be used for single channel processing. A simple extension, required to include the weighted discriminator combination is also given.

### **5.5.1 Design in the Analog Domain**

In the proposed algorithm the PLL noise bandwidth is chosen depending on the thermal noise and dynamic stress. The thermal noise for an arctangent PLL is given by (Kaplan 2006)

$$\sigma_{thermal, APLL} = \sqrt{\frac{B_{n,APLL}}{(C/N_0)_r} \left(1 + \frac{1}{2T_{coh}(C/N_0)_r}\right)} \quad (5.4)$$

where  $B_{n,APLL}$  is the noise bandwidth,  $(C/N_0)_r$  is the  $C/N_0$  expressed in linear units, and  $T_{coh}$  is the predetection interval (Kaplan 2006). Similarly, the error ( $\Delta\phi_{ss,APLL}$ ) due to acceleration stress on a second order PLL is given by (Gardner 2005)

$$\Delta\phi_{ss,APLL} = \frac{a}{\omega_n^2} \quad (5.5)$$

where  $a$  is the acceleration stress and  $\omega_n$  is the undamped natural frequency of the second order system under consideration. Ignoring the other sources of phase jitter, the goal is to choose a value for  $B_{n,APLL}$  that minimizes the tracking jitter,  $\sigma_{APLL}$ , as defined in Eq. (5.2). Hence, the noise bandwidth estimate ( $\hat{B}_{n,APLL}$ ) is obtained as

$$\hat{B}_{n,APLL} = \min_{B_n} (\sigma_{APLL}) = \min_{B_n} \left( \sigma_{thermal,APLL} + \frac{\Delta\phi_{ss,APLL}}{3} \right). \quad (5.6)$$

Loop stability is imposed as a constraint on the minimization defined in Eq. (5.6).

For loop stability, poles of the system ( $H(s)$ ) should lie in the left half of the s-plane, with  $H(s)$  defined as

$$H(s) = \frac{2\eta\omega_n s + \omega_n^2}{s^2 + 2\eta\omega_n s + \omega_n^2} \quad (5.7)$$

where  $\eta$  is the damping factor. The poles are  $-\eta\omega_n \pm j\omega_n\sqrt{1-\eta^2}$ . Assuming  $\eta = 0.707$ , which is suitable for most tracking applications, a second order PLL is stable for all positive values of  $\omega_n$  (Gardner (2005), Kaplan (2006)). This can be verified using the Routh stability criterion as well. For a given  $\eta$  and  $\omega_n$ , the noise bandwidth  $B_{n,APLL}$  is given by (Gardner 2005)

$$B_{n,APLL} = \frac{\omega_n}{2} \left( \eta + \frac{1}{4\eta} \right) = \gamma \omega_n \quad (5.8)$$

where  $\gamma = 0.5303$  for  $\eta = 0.707$ . Hence, for stability, it is sufficient to ensure that the adaptive algorithm chooses a positive value for noise bandwidth.

Upon minimizing the cost function defined in Eq. (5.6) using the first derivative test, the noise bandwidth estimate is found to be

$$\hat{B}_{n,APLL} = \sqrt[5]{16 a^2 \frac{\gamma^4}{9\beta}} \quad (5.9)$$

where  $\beta = \frac{1}{(C/N_0)_r} \left( 1 + \frac{1}{2T_{coh}(C/N_0)_r} \right)$ . A positive estimate of noise bandwidth ensures that the second derivative test for minima is met (since  $\beta$ ,  $a$  and  $\gamma$  are all non-zero positive quantities).

When  $C/N_0$  approaches infinity,  $\beta$  approaches zero, which makes  $\hat{B}_{n,APLL}$  approach  $\infty$ . This is expected. But for the other condition, as  $a$  approaches zero, the noise bandwidth estimate also approaches zero. This violates the stability criterion. One way to overcome this is by setting a hard minimum value on the allowed range of the noise bandwidth estimate. In this work, the hard minimum is fixed as  $\hat{B}_{n,APLL} \geq 0.25$  Hz.

So far in the formulation, the dynamic stress ( $a$ ) is assumed to be a known value, but in real-world applications it needs to be estimated. A solution to estimate the effect of dynamic stress is to use a filtered version of the phase discriminator output. This is based on the fact that phase acceleration will produce a non-zero mean term at the discriminator output, as described by Eq. (5.5). This is demonstrated in the following with the aid of a numerical simulation. A Doppler trajectory corresponding to a vehicle making turns at fixed intervals is simulated as shown in Figure 5-2. A second order PLL is allowed to

track the signal with a constant noise bandwidth and the discriminator outputs are plotted. A moderate  $C/N_0$  of 35 dB-Hz was assumed for this scenario. As observed from Figure 5-2, the change in Doppler trajectory is reflected clearly at the output of phase discriminator and this can be used as information about the dynamic stress level to adjust the noise bandwidth. A filter with a narrow-bandwidth is used to reduce the noise at the discriminator output. To distinguish this filter from the loop filter of the PLL, it will be referred to as the dynamic error filter.

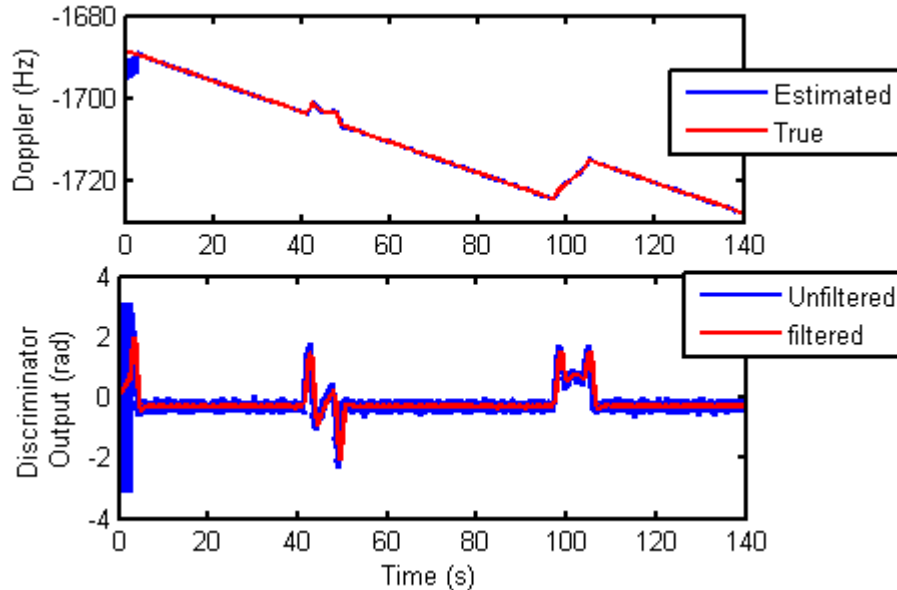


**Figure 5-2: Effect of dynamic stress on discriminator outputs**

The magnitude of the effect of dynamic stress as measured by the dynamic error filter depends on the noise bandwidth used by the PLL, as described in Eq. (5.5). Hence, appropriate scaling by  $\omega_n^2$  is required to account for the effect of noise bandwidth. Figure 5-3 shows the  $\omega_n^2$  scaled outputs of the dynamic error filter running on two independent implementations of the PLL tracking the reference Doppler trajectory described in Figure 5-2. The PLLs differ only by the noise bandwidth, one configured to use 1.5 Hz and the

other to use 5 Hz. The output of the dynamic error filter on each PLL is scaled by the respective  $\omega_n^2$  and is plotted against the reference in Figure 5-3. As shown in the figure, scaling removes the noise bandwidth dependence in the measurement of the dynamic stress.

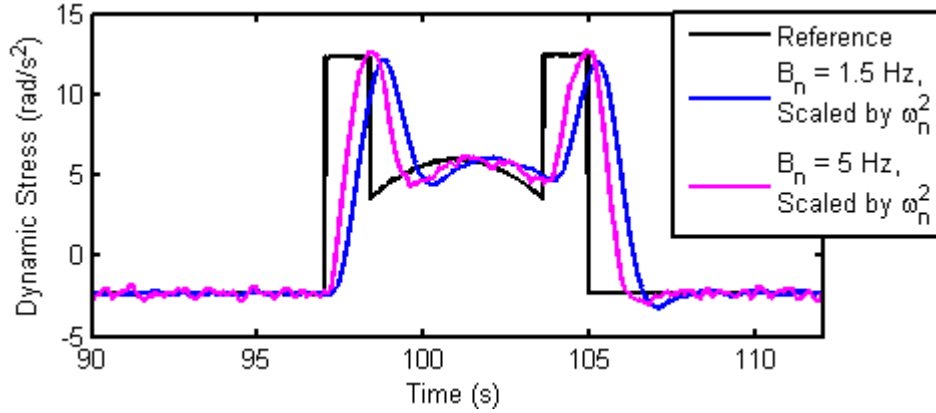


**Figure 5-3: Dynamic stress measured by two independent PLL with different noise bandwidth is scaled by their respective  $\omega_n^2$  and plotted against the true reference.**

The numerical simulations described above were carried out with constant noise bandwidth in order to demonstrate the ability to measure the dynamic stress. When this is integrated into the PLL and the noise bandwidth is adapted using the scaled dynamic error filter outputs and the  $C/N_0$  estimates, care should be taken to account for the effect of changing noise bandwidth on the dynamic error filter's input and output. This is explained in the following paragraph by better describing the proposed algorithm.

Let the phase discriminator output at the  $k^{\text{th}}$  instant be denoted by  $\Delta\hat{\phi}_k$ . Then the output of the dynamic error filter ( $\Delta\hat{\phi}_{ss}$ ) is calculated as

$$\Delta\hat{\phi}_{ss}(k) = \sum_{n=0}^2 c_n \Delta\hat{\phi}_{k-n} + \sum_{n=1}^2 d_n \Delta\hat{\phi}_{ss}(k-n) \quad (5.10)$$

where  $c_n$  and  $d_n$  are the filter coefficients. Assume that the noise bandwidth of the loop filter is constant over the time instants corresponding to the inputs  $\Delta\hat{\phi}_k$ ,  $\Delta\hat{\phi}_{k-1}$ , and  $\Delta\hat{\phi}_{k-2}$ . Then, the flow of the algorithm is given as follows:

- i. The estimate of the dynamic stress ( $a$ ) at time  $k$  is given by  $\Delta\hat{\phi}_{ss}(k) \cdot \omega_n^2(k)$ , where  $\omega_n(k)$  corresponds to the undamped natural frequency at time  $k$ .
- ii. The estimate of noise bandwidth, given  $a$  and  $C/N_0$ , at the time instant  $(k + 1)$  can be calculated using Eq. (5.9).
- iii. The update of  $\omega_n(k + 1)$  can be obtained based on the new noise bandwidth estimate.
- iv. The next estimate of error due to dynamic stress,  $\Delta\hat{\phi}_{ss}(k + 1)$ , should be computed after scaling the previous inputs ( $\Delta\hat{\phi}_k$ ,  $\Delta\hat{\phi}_{k-1}$ ) and outputs ( $\Delta\hat{\phi}_{ss}(k)$ ,  $\Delta\hat{\phi}_{ss}(k - 1)$ ) of the dynamic error filter to account for the changing  $\omega_n$  (or  $B_n$ ). The scaling factor ( $SF$ ) is given by

$$SF_{k+1} = \frac{\omega_n^2(k)}{\omega_n^2(k + 1)}. \quad (5.11)$$

The above scaling has been empirically found to aid in reducing the magnitude by which the transient of the noise bandwidth estimates shoots up. Thus, it reduces the risk of using a very high noise bandwidth during the transients.

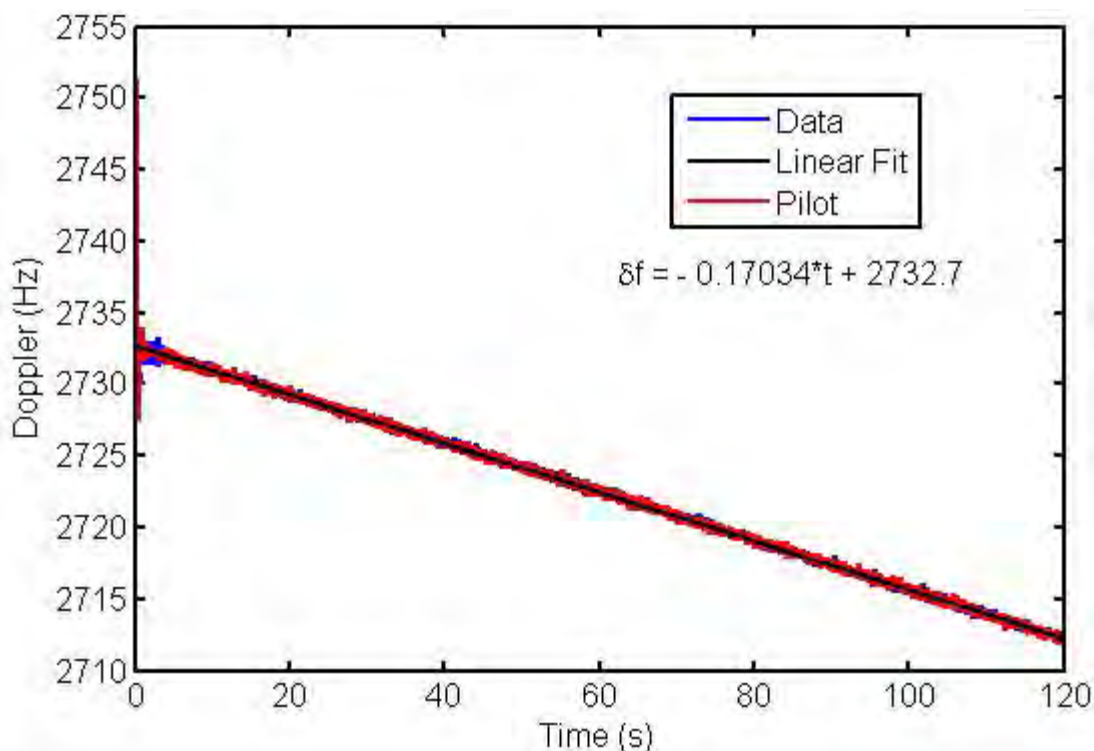
### 5.5.2 Algorithm Validation

The algorithm is initially validated using numerical simulations and then with live L2C signals transmitted by IIR-M satellites. For validation of the adaptive noise bandwidth algorithm, live signals under clear sky conditions are used. Under this condition, the dynamic stress is only due to the satellite motion. Since a second order

PLL is sensitive to acceleration stress, the goal is to verify whether the noise bandwidth estimated by the algorithm matches the theoretically predicted noise bandwidth. The theoretically predicted noise bandwidth or reference is obtained by directly using an average of the  $C/N_0$  estimates and the acceleration stress, computed using a first-order fit of the estimated Doppler, in the noise bandwidth estimate described by Eq. (5.9).

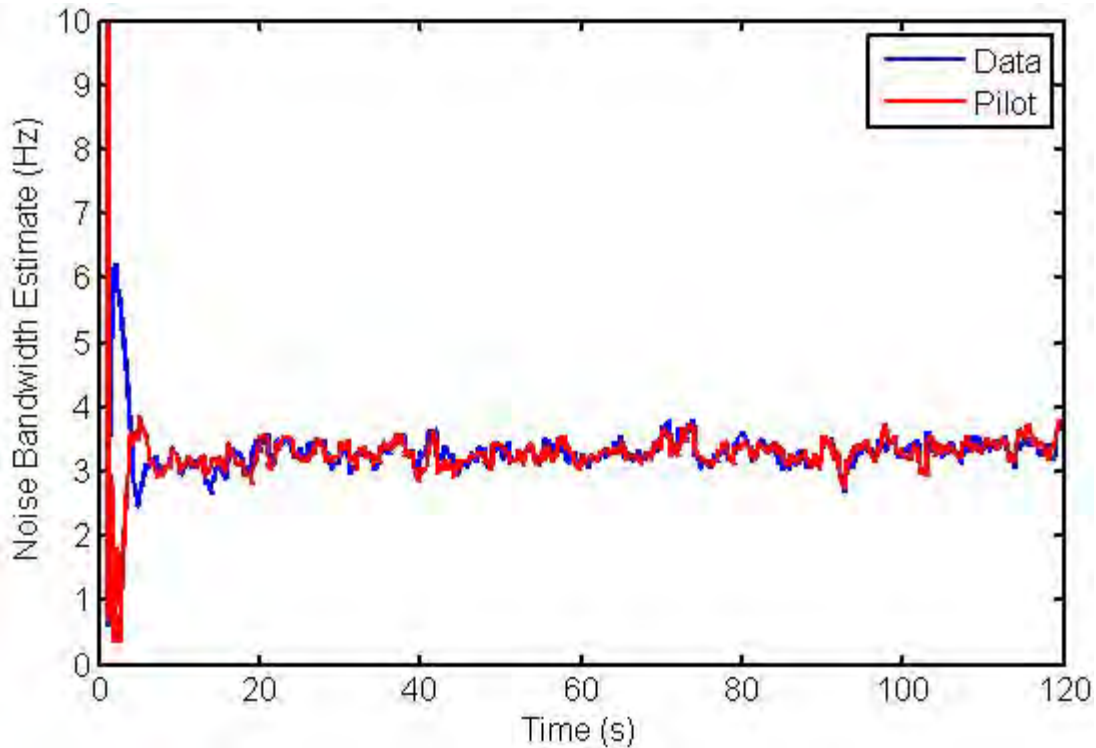
Figure 5-4 shows the Doppler plot obtained for PRN 31 at a  $C/N_0$  of 32 dB-Hz over a period of 120 s along with a linear fit of the obtained estimates. The linear fit provides a rough estimate of the acceleration (approximately  $0.17 \text{ Hz/s}^2$ ). Using this information in Eq. (5.9), the noise bandwidth should be set to approximately 3 Hz.

Figure 5-5 shows the time series for the noise bandwidth estimated by the proposed algorithm running independently on data and pilot channels. The obtained



**Figure 5-4: Doppler Estimate for PRN 31 with a linear fit of the obtained estimates.**

bandwidth agrees with the value expected from the linear fit. In Figure 5-5, a constant noise bandwidth of 10 Hz at the initial stages is the result of PLL being initiated after achieving carrier frequency lock using a FLL with a constant noise bandwidth of 10 Hz.



**Figure 5-5: Noise bandwidth estimates ( $B_{n,APLL}$ ) obtained using the adaptive noise bandwidth algorithm for PRN 31**

### 5.5.3 Issues

The performance of the method described in Section 5.5.1 degrades under two conditions:

- i. Low  $C/N_0$ : Under low  $C/N_0$  conditions, theoretical models for tracking jitter due to thermal noise (Eq. (5.4)) fail because of the non-linear nature of the arctangent discriminator.
- ii. Large value for the product of noise bandwidth and update rate ( $B_n T_{coh}$ ): Since the design is carried out in the analog domain, for large  $B_n T_{coh}$  values, the

bilinear transform fails to correctly map the analog filter to the digital domain. Thus, unstable digital loops will be obtained under such conditions. Kazemi & O’Driscoll (2008) have shown that using digital techniques for the loop filter design allow stable operation even under these extreme conditions.

Further, digital techniques allow accurate modelling of the cost function described in Eq. (5.2). Thus, a design in the digital domain can aid in better choice of noise bandwidth for a given condition.

#### 5.5.4 All-Digital Adaptive Bandwidth Tracking Design

The linear model of the digital phase-locked loop (DPLL) system along with the proposed adaptive noise bandwidth algorithm is shown in Figure 5-6. The phase of the incoming signal is given by  $\phi_r$  and the phase of the locally generated carrier is denoted by  $\phi_0$ . The phase error  $\Delta\phi = \phi_r - \phi_0$  is subjected to the discriminator gain,  $G_d$ , (unity gain for arctangent discriminators). The noise corrupting the discriminator output is given by  $n_{\Delta\phi}$ . Two coefficients which determine the loop filter response are given by  $k_1$  and  $k_2$ . For bandwidth adaptation, the effect of thermal noise and dynamic stress on the

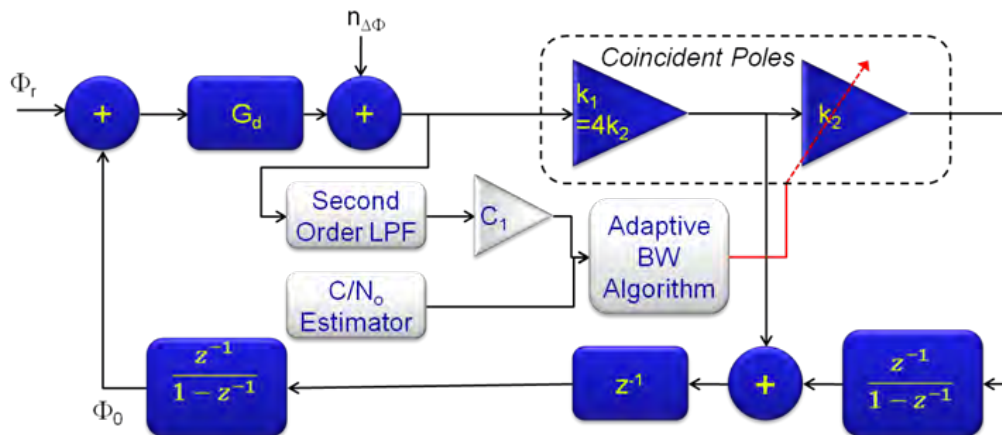


**Figure 5-6: Linear model of DPLL with the proposed adaptive noise bandwidth algorithm**

system needs to be derived as a function of the two coefficients  $k_1$  and  $k_2$ .

#### 5.5.4.1 Expression for Dynamic Stress Error

The transfer function ( $H_2(z)$ ) of the system represented in Figure 5-6 is given by (Gardner 2005)

$$H_2(z) = \frac{\phi_0(z)}{\phi_r(z)} = \frac{k_1 z^{-1}[1 - z^{-1} + k_2 z^{-1}]}{(1 - z^{-1})^2 + k_1 z^{-1}[1 - z^{-1} + k_2 z^{-1}]} \quad (5.12)$$

and the error transfer function,  $E_2(z)$ , is given by

$$\begin{aligned} E_2(z) &= \frac{\phi_r(z) - \phi_0(z)}{\phi_r(z)} = \frac{\Delta\phi(z)}{\phi_r(z)} = 1 - H_2(z) \\ &= \frac{(1 - z^{-1})^2}{(1 - z^{-1})^2 + k_1 z^{-1}[1 - z^{-1} + k_2 z^{-1}]} \end{aligned} \quad (5.13)$$

Further, a second order system is sensitive to acceleration stress ( $a$ ), which is given by

$$\phi_r[n] = \frac{aT_{coh}^2}{2} n^2 u[n] \quad (5.14)$$

and its Z-transform is given by

$$\phi_r(z) = \frac{a T_{coh}^2 z^{-1} (1 + z^{-1})}{2 (1 - z^{-1})^3}. \quad (5.15)$$

The steady state value of an arbitrary transfer function  $X(z)$  is computed using the final value theorem (Oppenheim & Schafer 1999) as

$$\lim_{n \rightarrow \infty} x[n] = \lim_{z \rightarrow 1} (1 - z^{-1})X(z). \quad (5.16)$$

Using this relationship, the steady state error of a system described by  $H_2(z)$  due to a dynamic stress given by  $\phi_r(z)$  is computed as

$$\Delta\phi_{ss,DPLL} = \lim_{z \rightarrow 1} (1 - z^{-1})\phi_r(z)E_2(z) = \frac{aT_{coh}^2}{k_1 k_2}. \quad (5.17)$$

#### 5.5.4.2 Expression for Tracking Jitter due to Thermal Noise

In order to derive an expression for  $\sigma_{thermal, DPLL}^2$ , the variance ( $\sigma_{n_{\Delta\phi}}^2$ ) of the noise ( $n_{\Delta\phi}$ ) at the output of the discriminator needs to be modelled. An arctangent discriminator is used in this thesis. The noise variance of an arctangent discriminator is given by (Crosta 2009)

$$\sigma_{n_{\Delta\phi}}^2 = \frac{\pi^2}{3} e^{-\frac{A^2}{2}} + \frac{A}{2\sqrt{2\pi}} \int_{-\pi}^{+\pi} \phi^2 e^{-\frac{A^2}{2} \sin^2 \phi} \cos(\phi) \left[ 1 + \operatorname{erf} \left( A \frac{\cos \phi}{\sqrt{2}} \right) \right] d\phi \quad (5.18)$$

where  $A$  is the amplitude of the signal normalized with respect to the noise variance of the accumulated correlator outputs and  $\operatorname{erf}$  is the error function given by

$$\operatorname{erf}(x) = \frac{2}{\sqrt{\pi}} \int_0^x e^{-t^2} dt. \quad (5.19)$$

For ease of implementation and in order to avoid the numerical computation of the integral in Eq. (5.18), at each bandwidth update (i.e., every 20 ms), a curve interpolating the variance defined by Eq. (5.18) is used. The proposed interpolation is based on the CRLB for phase estimation: a cubic spline is used to account for the difference with respect to  $\sigma_{n_{\Delta\phi}}^2$ . The CRLB derivation is provided in Appendix C and provides a good approximation for  $\sigma_{n_{\Delta\phi}}^2$  for  $C/N_0$  greater than 25 dB-Hz. Thus, the expression for the interpolated model ( $\tilde{\sigma}_{n_{\Delta\phi}}^2$ ) is given as

$$\tilde{\sigma}_{n_{\Delta\phi}}^2 = \begin{cases} \frac{1}{2 \left( \frac{C}{N_0} \right)_r T_{coh}}, & (C/N_0)_{dB-Hz} \geq 25 \\ f(z) + \frac{1}{2 \left( \frac{C}{N_0} \right)_r T_{coh}}, & (C/N_0)_{dB-Hz} < 25 \end{cases} \quad (5.20)$$

where  $f(z)$  is a cubic fit of the difference between the actual variance and CRLB under weak  $C/N_0$  conditions. Figure 5-7 shows the agreement between the interpolated model, Monte Carlo simulation and Eq. (5.18).

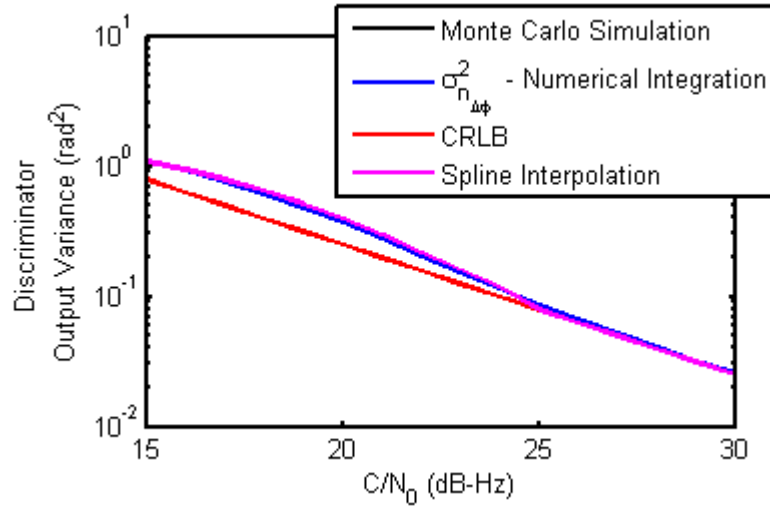


**Figure 5-7: Comparison of fit of different models for noise variance at the output of arc tangent discriminator**

Having derived a model for the discriminator output noise variance, the next step is to derive an expression for the tracking jitter due to thermal noise ( $\sigma_{thermal,DPLL}^2$ ). Since the noise  $n_{\Delta\phi}$  is white with variance,  $\sigma_{n_{\Delta\phi}}^2$ , the autocorrelation function ( $R_{n_{\Delta\phi}}$ ) and the power spectrum density ( $S_{n_{\Delta\phi}}$ ) are given by

$$R_{n_{\Delta\phi}}(\tau) = \sigma_{n_{\Delta\phi}}^2 \delta(\tau) \quad (5.21)$$

$$S_{n_{\Delta\phi}}(\omega) = \sigma_{n_{\Delta\phi}}^2. \quad (5.22)$$

Given the power spectrum density ( $S_{n_{\Delta\phi}}$ ) of the input and the system transfer function ( $H_2(z)$ ), the noise variance at the output of the system, or the tracking jitter due to thermal noise, is given by

$$\begin{aligned}
\sigma_{thermal, DPLL}^2 &= \mathcal{Z}^{-1} \left[ H_2(z) H_2(z^{-1}) S_{n_{\Delta\phi}}(\omega) \right] \\
&= \frac{\sigma_{n_{\Delta\phi}}^2}{2\pi j} \int_{|z|=1} H_2(z) H_2(z^{-1}) z^{-1} dz.
\end{aligned} \tag{5.23}$$

The integral in the Eq. (5.23) and the noise bandwidth ( $B_{n, DPLL}$ ) of the system are related as (Gardner 2005)

$$2B_{n, DPLL} T_{coh} = \frac{1}{2\pi j} \int_{|z|=1} H_2(z) H_2(z^{-1}) z^{-1} dz. \tag{5.24}$$

Hence, the expression for  $\sigma_{thermal, DPLL}^2$  can be rewritten as

$$\sigma_{thermal, DPLL}^2 = 2B_{n, DPLL} T_{coh} \tilde{\sigma}_{n_{\Delta\phi}}^2 \tag{5.25}$$

where  $B_{n, DPLL}$  is the noise bandwidth of the second order DPLL, given by (Gardner 2005)

$$B_{n, DPLL} = \frac{k_1}{4T_{coh}} \frac{1 + \frac{k_2}{k_1} - \frac{k_2}{2}(3 - k_2)}{1 - k_2 - \frac{k_1}{4}(2 - k_2 + k_2^2)}. \tag{5.26}$$

#### 5.5.4.3 Model Validation

The model derived is initially validated using numerical simulations. This section describes the scenario set for the simulation and compares the obtained results with the derived model based on the design in both the analog and digital domains. The parameters used for the scenario are as follows:

- i.  $T_{coh} = 20$  ms
- ii.  $B_n$  (design noise bandwidth) is chosen in the 0.5 to 30 Hz range, in steps of 0.5 Hz

- iii. For every  $B_n$  under consideration, 50 independent runs of PLL (both digital and analog designs) are simulated.  $B_{n,DPLL}$  and  $B_{n,APLL}$  are set to be equal to the chosen  $B_n$ .  $B_{n,APLL}$  is mapped to the loop filter coefficients using a bilinear transform.  $B_{n,DPLL}$  is used to compute the coefficients  $k_1$  and  $k_2$  of the digital loop filter design using Eq. (5.26) and a constraint for identical poles ( $k_1 = 4k_2$ ). The tracking jitter due to thermal noise is averaged across independent runs, provided that the measured tracking jitter for at least 75% of the runs stays with the tracking threshold, which in this case is  $30^0$  (one-fourth of the phase pull-in range of the ATAN2 discriminator as, shown by Eq (5.2)).

Figure 5-8 shows the measured tracking jitter due to thermal noise against the model for both APLL and DPLL implementations. The measured thermal jitter for the digital design closely matches the model defined in Eq. (5.25) and remains stable for

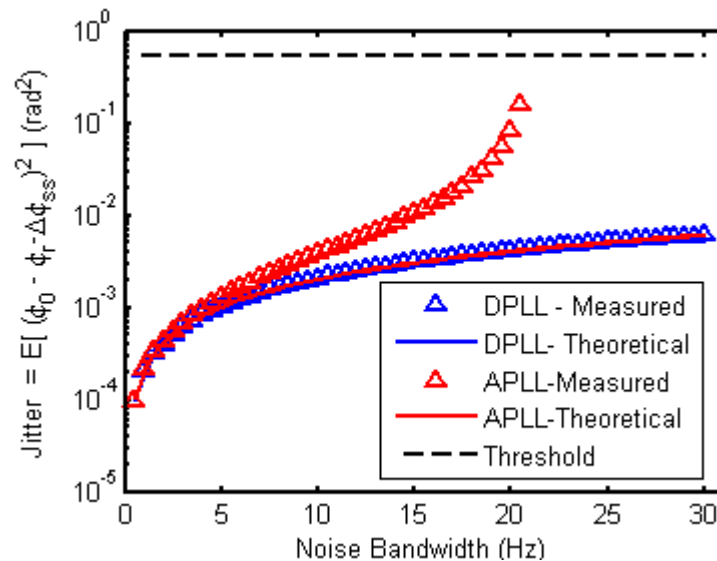


**Figure 5-8: Comparison of measured tracking jitter due to thermal noise for APLL and DPLL with their respective models for a  $C/N_0$  of 37 dB-Hz**

large values of noise bandwidth. On the other hand, the measured jitter for APLL significantly deviates from the model described in Eq. (5.4), and becomes unstable for large values of  $B_n$  as the assumption of  $B_{n,APLL}T_{coh} \ll 1$  is no longer valid. The deviation in the case of APLL can be measured by calculating the true noise bandwidth after the bilinear transform has been applied using Eq. (5.26).

The results for a  $C/N_0$  of 20 dB-Hz are shown in Figure 5-9. The model for the DPLL matches the measured thermal jitter, whereas the measured thermal jitter for APLL deviates from the theoretical model.

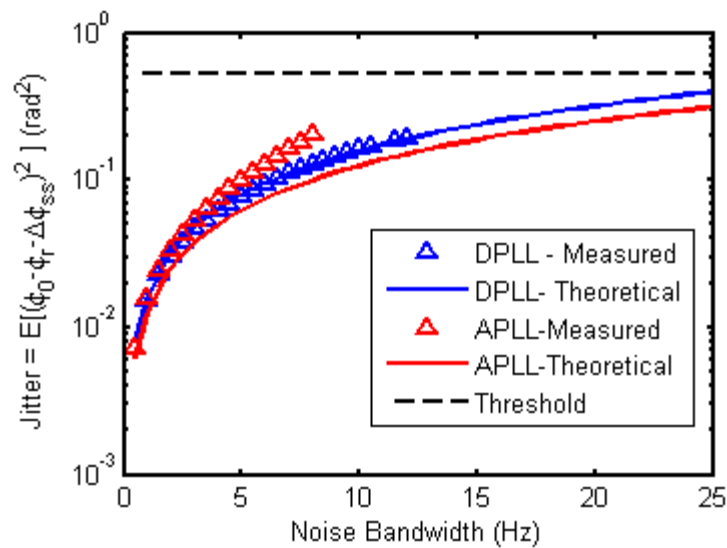


**Figure 5-9: Comparison of measured tracking jitter due to thermal noise for APLL and DPLL with their respective models for a  $C/N_0$  of 20 dB-Hz**

#### 5.5.4.4 Stability Constraints and Noise bandwidth Estimate for DPLL

Conditions for the stability of a second order DPLL are (Gardner 2005)

$$k_2 < 1 \text{ and } k_1 < \frac{4}{2 - k_2}. \quad (5.27)$$

The above conditions ensure that the poles of the closed loop system ( $H_2(z)$ ) lie within the unit circle ( $|z| = 1$ ). The poles are given by

$$z_{poles} = 1 - \frac{k_1}{2} \pm \sqrt{1 - \left(\frac{4k_2}{k_1}\right)}. \quad (5.28)$$

To reduce the dimensionality of the problem, an extra constraint of coincident poles is imposed. For the poles to be coincident, the condition  $k_1 = 4k_2$  should be met. Substituting this constraint, the conditions for stability reduce to

$$0 < k_2 < 1. \quad (5.29)$$

Hence, the noise bandwidth estimate should minimize a cost function ( $C_{DPLL}$ ), similar to Eq. (5.6), under the constraint defined in Eq. (5.29). In other words, since the relationship between  $k_1$  and  $k_2$  is fixed, the value of  $k_2$  that minimizes  $C_{DPLL}$  should be chosen as

$$\hat{k}_2 = \min_{k_2} \left( \sigma_{n_{\Delta\phi}} \sqrt{\frac{5k_2 - 6k_2^2 + 2k_2^3}{2 - 6k_2 + 2k_2^2 - 2k_2^3}} + \frac{aT_{coh}^2}{12k_2^2} \right). \quad (5.30)$$

Although the minimum can be found by solving the equation  $\frac{\partial C_{DPLL}}{\partial k_2} = 0$ , this approach is quite complex. Hence, the solution is obtained by using a gradient descent algorithm with a pre-defined step size ( $B_{n,step} = 0.25$  Hz), which results in the following recursion:

$$\hat{B}_{n,DPLL}[n] = \min_{B_n} \left\{ \sqrt{2(\hat{B}_{n,DPLL}[n-1] \pm B_{n,step})T_{coh}\sigma_{n_{\Delta\phi}}^2} + \frac{\Delta\phi_{ss,DPLL}}{3} \right\}. \quad (5.31)$$

#### 5.5.4.5 Validation of Adaptive Noise Bandwidth Algorithm

The adaptive noise bandwidth algorithm is validated using numerical simulations. The parameters for the simulation are identical to those described in section 5.5.4.3.

Additionally, the incoming signal is subjected to an acceleration stress of  $1 \text{ Hz/s}^2$ . This is the maximum acceleration stress due to satellite motion that a static receiver needs to handle (Tsui 2000). Figure 5-10 shows a plot of the theoretical and measured cost functions across different design noise bandwidth values for a  $37 \text{ dB-Hz } C/N_0$ . The figure also gives the noise bandwidth as estimated by the adaptive bandwidth algorithm running on the APLL and DPLL. As expected, as the noise bandwidth increases, the measured cost function of the APLL deviates significantly from the theoretical model, whereas the digital model fits well with the measured cost function. Further, it can be observed that the adaptive noise bandwidth algorithm on both the APLL and the DPLL chooses the minimum of the cost function.

Similarly, Figure 5-11 shows the plot of the measured cost function against the theoretical model for a  $C/N_0$  of  $20 \text{ dB-Hz}$ . Here, again, the noise bandwidth estimated by

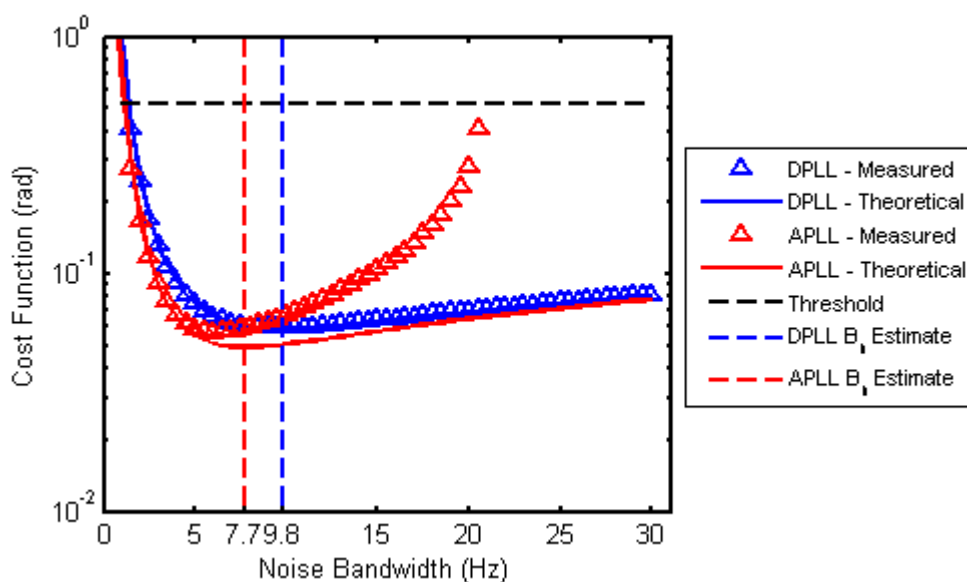


**Figure 5-10: Cost function (theoretical and measured) for the design in the analog (APLL) and digital domain (DPLL) along with the noise bandwidth estimated by the proposed algorithm for a  $C/N_0$  of  $37 \text{ dB-Hz}$ .**

the adaptive algorithm corresponds to the minimum of the curves. Since the APLL failed to obtain a stable lock on the signal, the corresponding estimated noise bandwidth is not plotted in Figure 5-11.

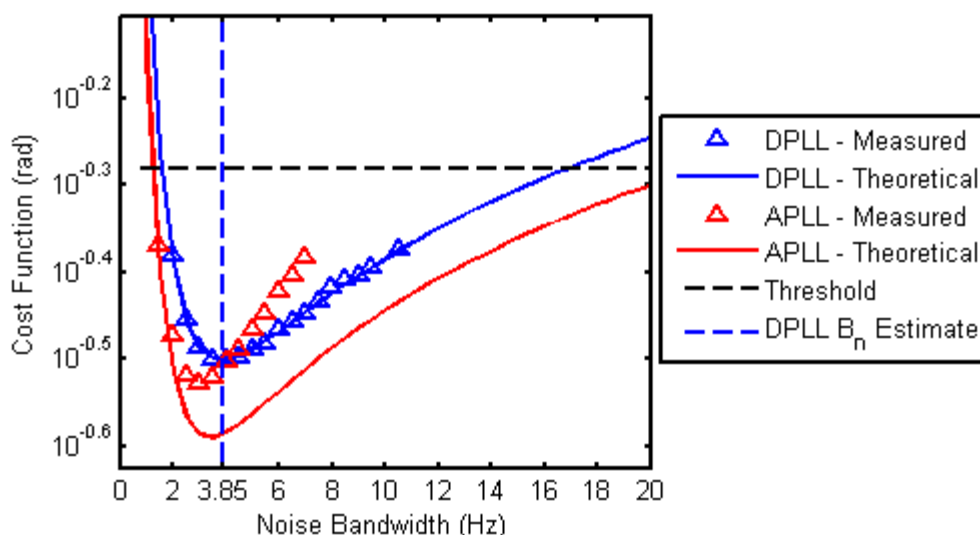


**Figure 5-11: Cost function (theoretical and measured) for the APLL and DPLL design along with the noise bandwidth estimated by the proposed algorithm for a  $C/N_0$  of 20 dB-Hz.**

Having validated the noise bandwidth estimate against the minimum of the curves corresponding to the cost function under two different  $C/N_0$  conditions, a new test setup is used to obtain the noise bandwidth estimate and cost as a function of input  $C/N_0$ . In this setup, independent runs of the PLL with the adaptation algorithm integrated are used to track an incoming signal with a fixed acceleration stress of  $1 \text{ Hz/s}^2$ . The update rate of the PLL is fixed to 20 ms. Figure 5-12 shows the noise bandwidths estimated using the proposed algorithm as a function of the input  $C/N_0$  for both APLL and DPLL. Theoretical curves in the figure are obtained by computing the optimum noise bandwidth using the true  $C/N_0$  and dynamic stress ( $a$ ) values. Measured values are obtained by averaging the noise bandwidth estimate across independent runs of the PLL. The theoretically predicted

values match the design noise bandwidth selected by the proposed algorithm across  $C/N_0$ . For APLL, the true noise bandwidth values corresponding to the chosen design noise bandwidths are also plotted. As described before, the deviation of the true from the design values increases with increasing noise bandwidth values.

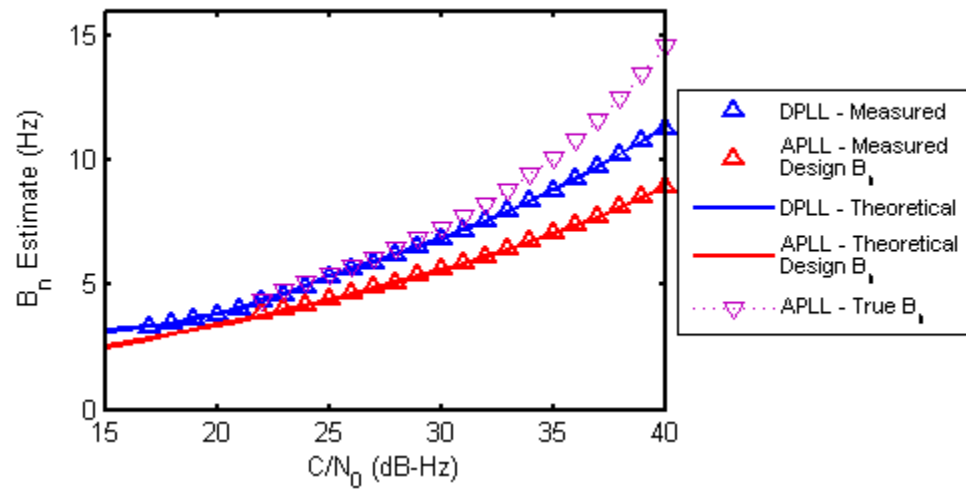


**Figure 5-12: Comparison of actual and theoretically predicted noise bandwidth estimates**

Figure 5-13 shows the values assumed by the measured and theoretical cost functions corresponding to the noise bandwidth chosen by the algorithm, as given in Figure 5-12. For the APLL, the theoretical curve is obtained by using the model described in Section 5.5.1. As observed from the figure, for moderate-high  $C/N_0$  conditions where a large noise bandwidth (design) value is chosen by the adaptation algorithm the model does not match well with the measured cost function. This is due to the difference between design and actual loop bandwidth. Similarly, under low  $C/N_0$  conditions, since the effect of discriminator non-linearity was not included in the APLL design, the model fails even though the design noise bandwidth values are small. However, when the true  $B_n$  values and the model for discriminator output variance ( $\tilde{\sigma}_{n_{\Delta\phi}}^2$ )

are used in the computation of cost using Eq. (5.25) a close match can be obtained for the APLL as well. Thus, the digital implementation serves mainly to aid in accurate modelling and a proper choice of the noise bandwidth.

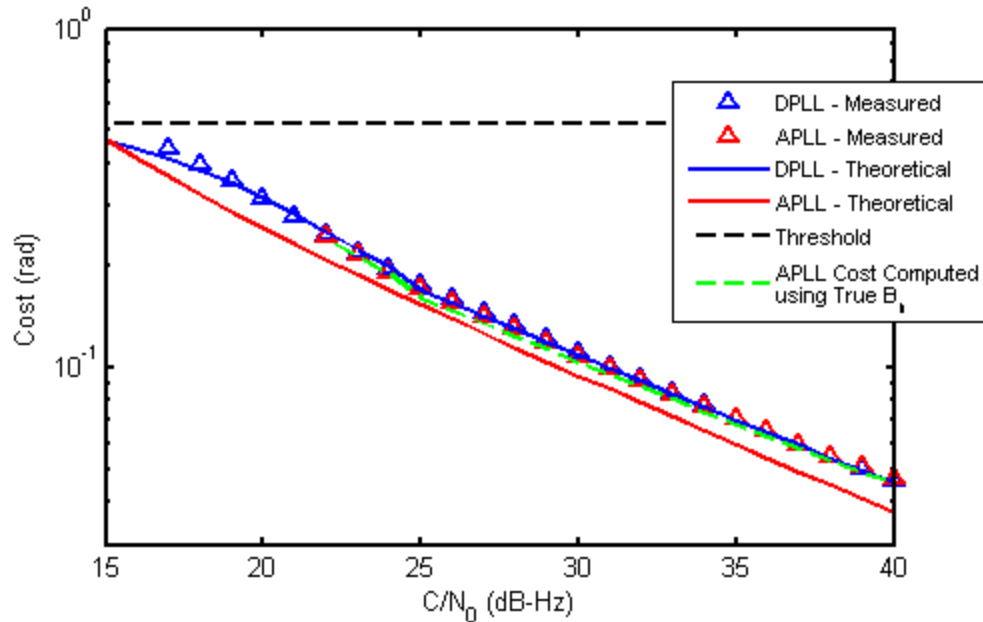


**Figure 5-13: Comparison of theoretical and measured cost functions of the APLL and the DPLL with the adaptive bandwidth algorithm**

Sections 5.5.1 through 5.5.4 discussed the design of an adaptive noise bandwidth algorithm for a single channel. The following section extends the above algorithm to include the weighted discriminator combination.

### 5.5.5 Extension to Weighted Discriminator Combination

In order to extend the adaptive noise bandwidth algorithm designed in the digital domain to include the weighted combination of discriminators described in Section 5.4.1, the noise variance at the output of the weighted combination of discriminators needs to be modelled. The discriminators used in the combination include ATAN2 in the pilot channel, and ATAN2 with correction for the data bit sign in the data channel. Hence, the

noise variance ( $\sigma_{w,n_{\Delta\phi}}^2$ ) at the output of the weighted combination of the discriminators is given by

$$\sigma_{w,n_{\Delta\phi}}^2 = w_d^2 \sigma_{ATAN2,data}^2 + w_p^2 \sigma_{ATAN2}^2 \quad (5.32)$$

where  $w_d$  and  $w_p$  are the weights used on the data and pilot channels respectively,  $\sigma_{ATAN2}^2$  is the noise variance at the output of the four-quadrant arctangent discriminator whereas  $\sigma_{ATAN2,data}^2$  is the variance of the data discriminator output. The model for  $\sigma_{ATAN2}^2$  is derived in Section 5.5.4.2 and is given by  $\tilde{\sigma}_{n_{\Delta\phi}}^2$  (Eq. (5.20)). Figure 5-14 plots the difference between  $\sigma_{ATAN2,data}^2$  and  $\sigma_{n_{\Delta\phi}}^2$  and a cubic fit for the same.

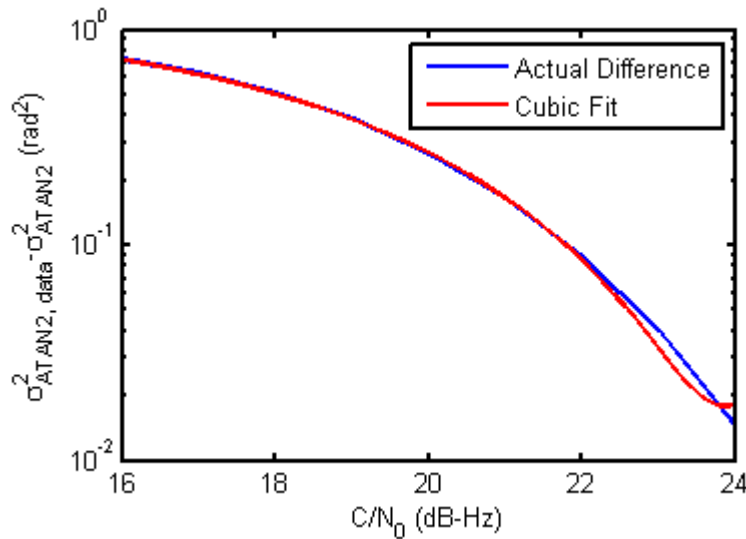


**Figure 5-14: Difference between the noise variance of the phase discriminator outputs on the data and pilot channels.**

This difference is due to the errors introduced by the data bit correction and is significant only for  $C/N_0$  lower than 24 dB-Hz (i.e. a difference of more than  $10^{-2}$  rad<sup>2</sup>).

Hence, the model for  $\sigma_{ATAN2,data}^2$  is given as

$$\sigma_{ATAN2,data}^2 = \begin{cases} \tilde{\sigma}_{n_{\Delta\phi}}^2 & \frac{C}{N_0} \geq 24 \text{ dB} - \text{Hz} \\ \tilde{\sigma}_{n_{\Delta\phi}}^2 + f_D(z) & \frac{C}{N_0} < 24 \text{ dB} - \text{Hz} \end{cases} \quad (5.33)$$

where  $f_D(z)$  is the cubic fit for the difference.

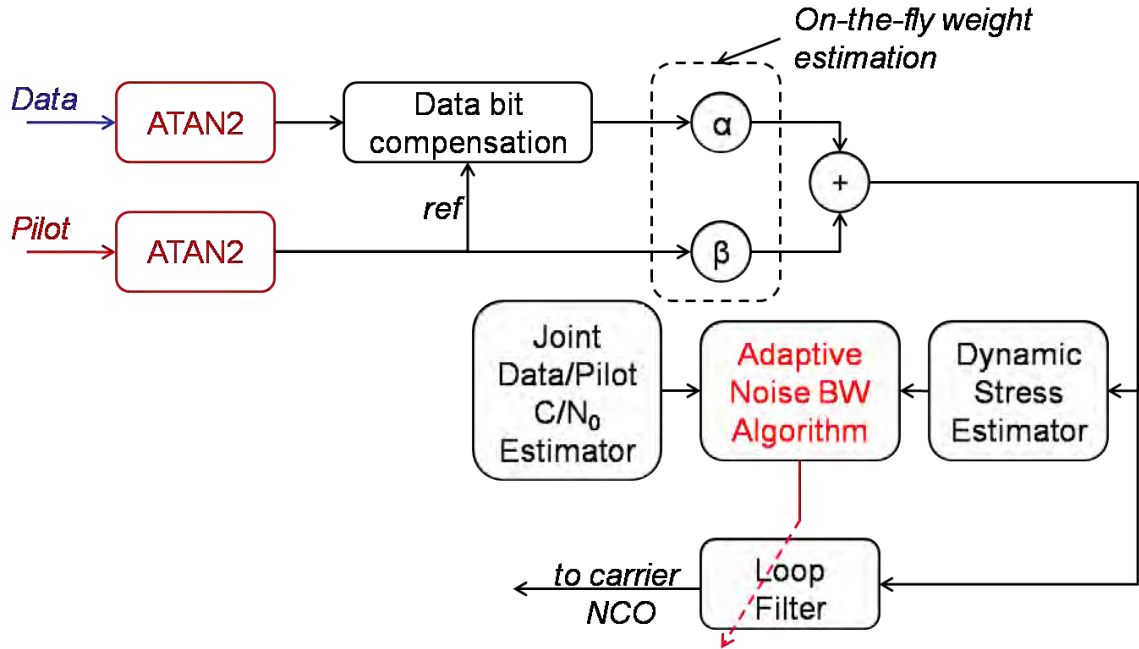


**Figure 5-15: Block diagram of the proposed method for joint data/pilot carrier phase tracking**

Figure 5-15 shows a block diagram of the proposed method for joint data/pilot carrier phase tracking along with the proposed adaptive noise bandwidth algorithm. Thus, in the standard tracking architecture which uses a weighted combination of discriminators, the information about weights, phase error estimate, and measured  $C/N_0$  are passed on to the adaptive noise bandwidth tuning algorithm. The weights, along with the information about measured  $C/N_0$ , are used to derive  $\sigma_{ATAN2}^2$ ,  $\sigma_{ATAN2,data}^2$  and  $\sigma_{w,n_{\Delta\phi}}^2$ . From this information, the tracking jitter due to thermal noise is computed using Eq. (5.25). The discriminator outputs are passed through the dynamic error filter in order to

obtain the effect of dynamic stress on the system,  $\Delta\phi_{ss,DPLL}$ . Finally, a noise bandwidth that minimizes the cost function ( $C_{DPLL}$ ) is estimated and the loop filter coefficients are updated accordingly every  $T_{coh}$ .

A detailed performance analysis of the proposed algorithms using live and hardware simulated signals is presented in Chapter 6.

## **CHAPTER SIX: ADAPTIVE BANDWIDTH DATA/PILOT CARRIER PHASE TRACKING RESULTS**

In this chapter, the performance of the single channel and joint data/pilot tracking methods proposed in Chapter 5 are assessed. This chapter is organized into two sections, each describing the motivation, the test setup, methodology and the results obtained. The goal of the first section is to quantify the tracking threshold of the different methods under static conditions. From the results, it emerges that there is no significant degradation in tracking threshold when using the proposed data/pilot tracking algorithm as compared to the use of the pilot channel alone with a pure PLL. In the second section, the advantages of using data/pilot tracking versus single channel tracking are analyzed under dynamic conditions.

### **6.1 Tracking Sensitivity**

This section quantifies the tracking threshold for the single channel and data/pilot tracking algorithms described in Chapter 5. The tracking methods which will be compared include the APLL and DPLL described in Chapter 5. Both designs incorporate the proposed adaptive noise bandwidth algorithm. Specifically, the following methods to track the signal are considered:

- i. *APLL – Data* - APLL using data channel alone with an arctangent (ATAN) discriminator
- ii. *APLL – Pilot* - APLL using pilot channel alone with an ATAN2 discriminator
- iii. *APLL – Joint (Costas)* - APLL using weighted combination of discriminators, where an ATAN discriminator is used on both channels

- iv. *APLL – Joint (ATAN2)* - APLL using weighted combination of discriminators, where an ATAN2 is used on both channels after sign compensation on the data channel
- v. *DPLL – Pilot* - DPLL using pilot channel alone with an ATAN2 discriminator
- vi. *DPLL – Joint (ATAN2)* - DPLL using weighted combination of discriminators, where ATAN2 is used on both channels
- vii. *KF – Joint* - Kalman filter based joint data/pilot tracking

The following subsection describes the test setup used to quantify the tracking threshold of the different methods listed above.

### 6.1.1 Test Setup

Live GPS L2C signals are used to analyse the performance of the proposed algorithms. Figure 4-8 shows a block diagram representing the setup adopted for the data collection. A static receiver under weak signal conditions is used for this test. The received signal is split into two channels. One of the channels is subjected to attenuation using an external attenuator whereas the second is not attenuated. The former will be referred to as the attenuated channel and the latter as the reference channel. In order to obtain good reference signals, the data is collected when the IIR-M satellites are at an elevation of 60 degree or higher. This ensures a  $C/N_0$  of 40 dB-Hz or higher for the reference channel. The attenuation level of the external attenuator is gradually increased in known steps at known time intervals. Since the external attenuator is present in the RF chain after the LNA, the effect of attenuation on the  $C/N_0$  is given by the Friis formula. Rather than modelling this effect, the received  $C/N_0$  measured by the receiver is used.

Both channels are down-converted, digitized and synchronously logged using a National Instruments (NI) PXI-5561 RF front-end (NI PXI 5661 2006) at a sampling rate of 5 MHz (complex samples).

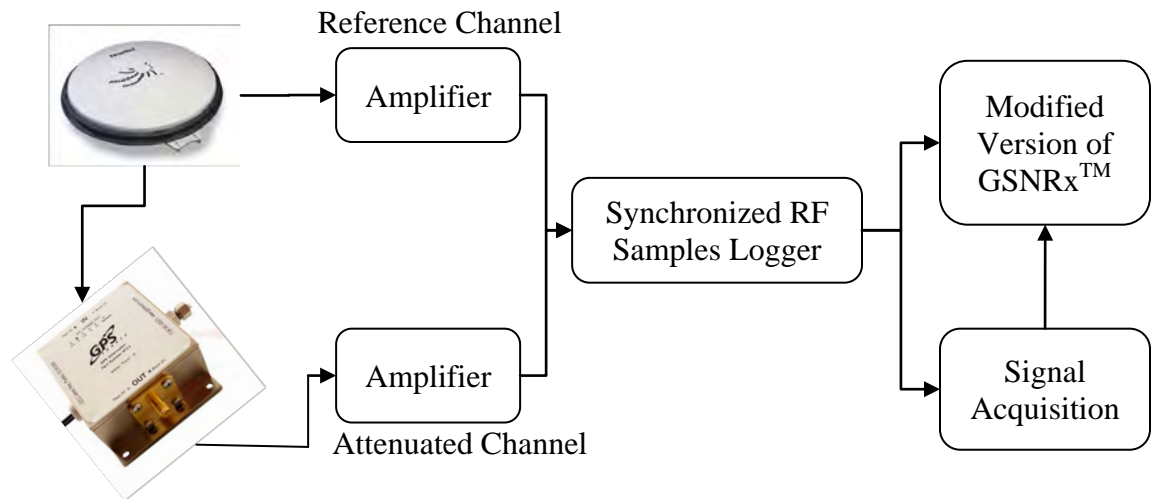


**Figure 6-1: Block diagram of data collection and processing setup**

The collected data is processed using a modified version of the PLAN Group's GNSS software navigation receiver (GSNRx<sup>TM</sup>) (Petovello et al 2008). The software receiver outputs Doppler estimates (loop filter outputs) at each loop update, which is typically set to be equal to the data bit period (20 ms). Unlike numerical simulations, for live signals, the true input signal phase is not available for the computation of the bias in the phase estimates. So, only the tracking jitter due to thermal noise is used to evaluate the tracking threshold of the different algorithms. The tracking jitter is measured using the Doppler estimates as follows: the Doppler estimates from the reference channel are used to remove the deterministic component due to satellite motion from the Doppler estimates of the attenuated channel. This gives the error in the Doppler estimates. This error is then passed through an NCO model, and the standard deviation at its output is

measured. This corresponds to the tracking jitter due to thermal noise ( $\sigma_{thermal}$ ). Phase lock is declared when the following conditions are met: (i) the  $1\sigma$ -tracking jitter stays within a threshold of  $30^\circ$  and (ii) the Doppler estimated from the attenuated channel follows that of the reference channel (visual). In order to keep the noise contribution from the reference channel negligible, only those satellites whose  $C/N_0$  in the reference channel is at least 10 dB higher than that in the attenuated channel are considered. For example, Figure 6-2 shows the plot of  $C/N_0$  on the reference and attenuated channels. The reference  $C/N_0$  for this satellite was approximately 44 dB-Hz. In this case, the analysis results from the attenuated channel are obtained only for time intervals corresponding to  $C/N_0$  less than 34 dB-Hz, which is at least 10 dB lower than the reference.

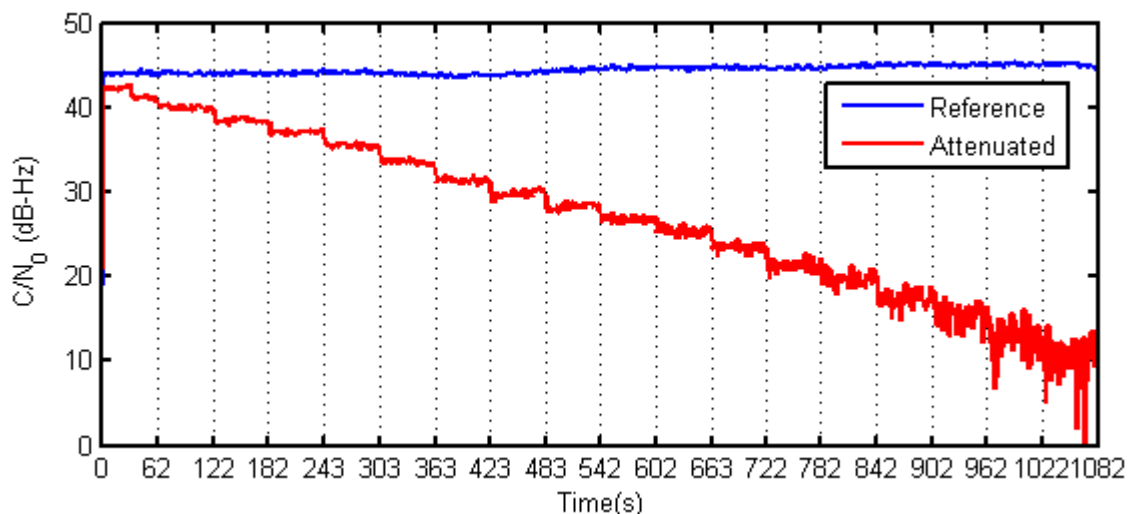


**Figure 6-2: Sample plot of measured  $C/N_0$  on reference and attenuated channels**

Figure 6-3 shows a plot of noise bandwidth estimates obtained using analog and digital implementations of independent pilot and data/pilot tracking. Average  $C/N_0$  corresponding to every 60 second time interval is plotted for reference. In both analog and digital implementations, while using a weighted combination of discriminators (joint

data/pilot tracking), the effect of thermal noise is reduced as compared to pilot-only tracking. Hence, the joint data/pilot tracking algorithms choose a larger noise bandwidth to reduce the effect of the dynamic stress due to satellite motion.

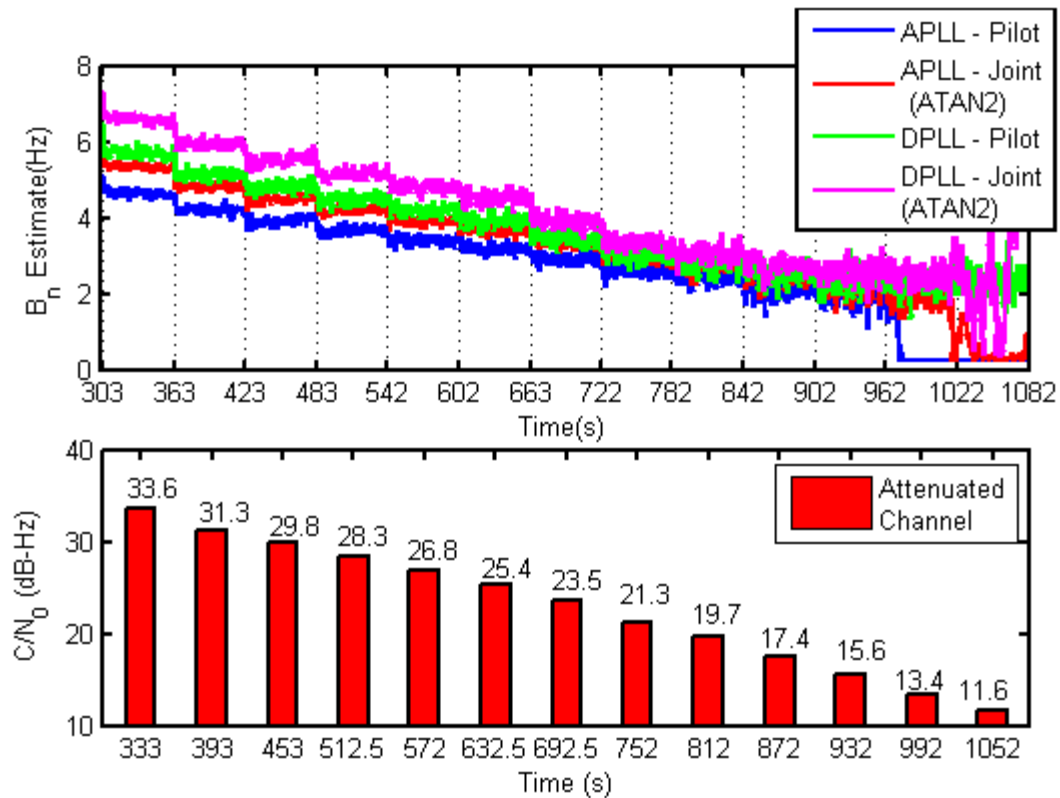


**Figure 6-3: Noise bandwidths selected by the adaptive bandwidth algorithms for single channel and data/pilot tracking.**

Across all implementations, as  $C/N_0$  approaches the tracking threshold, the noise bandwidth chosen by the algorithm converges to zero and a hard minimum of 0.25 Hz is chosen to avoid this condition. This effect can be clearly observed for the *APLL-Pilot* in Figure 6-3.

### 6.1.2 Results

The tracking threshold results presented in this section are averaged across 10 satellites in 4 data sets collected during different time periods. The standard deviation of

the measured tracking threshold is also plotted to show the uncertainty levels. Figure 6-4 shows a comparison of tracking thresholds across different independent and data/pilot carrier phase tracking algorithms. For independent tracking of data or pilot channel using APLL, as expected, the data channel only (*APLL-Data*) tracking loses lock earlier than pilot only tracking (*APLL-Pilot*), which is due to the lower phase pull-in range of the Costas loops. The difference in tracking thresholds between the two is approximately 6 dB, in agreement with the literature (Kaplan 2006).

The following is observed while using a weighted combination of discriminators in an APLL:

- i. the use of a weighted combination of Costas discriminators (*APLL-Joint (Costas)*) reduces the tracking threshold by approximately 3 dB as compared to independent data channel tracking. However, the advantages of using *APLL-Pilot* are lost in this combination.
- ii. the use of a weighted combination of ATAN2 discriminators (*APLL-Joint (ATAN2)*) allows the loop to maintain lock for almost the same level of attenuation as a pure PLL on the pilot channel (*APLL-Pilot*).

The advantage in using a digital design (DPLL) against APLL in independent pilot only tracking is approximately 1 dB in terms of tracking threshold.

The proposed joint data/pilot tracking algorithms namely, (i) the weighted combination of ATAN2 discriminators with design in digital or analog domains and (ii) the Kalman filter based joint data/pilot tracking, are able to maintain lock within 1 dB of the tracking threshold of *DPLL-Pilot*. It should be noted that, for joint data/pilot tracking using a Kalman filter, the tracking threshold and jitter performance depends on the

accuracy of the system and observation noise model. This includes accurately predicting the effect of the clock, variations in signal amplitude, and expected variations in dynamics. These quantities are often not readily available and are mostly equipment and environment specific. The values used in this case are fixed initially from Brown & Hwang (1997) for the clock parameters and the KF based implementation available in GSNRx™ for the other parameters. Later, they are fine tuned empirically on a trial-and-error basis. The exact values used are given in Appendix-A for completeness.

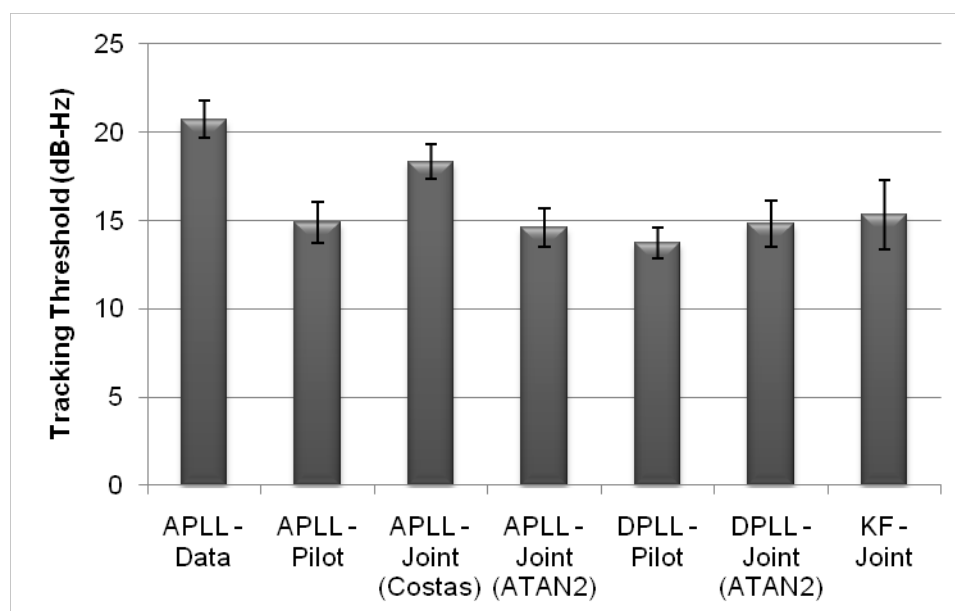


**Figure 6-4: Performance comparison of carrier phase tracking methods based on tracking threshold**

It has been shown that with careful design, it is possible to use joint data/pilot tracking algorithms without significant losses in terms of tracking threshold as compared to a pure-PLL on the pilot channel alone. The main advantage of joint data/pilot tracking with adaptive noise bandwidth is the ability to use a larger noise bandwidth as compared to independent tracking for a given  $C/N_0$ , as shown in Figure 6-3. This is exploited to

highlight the advantages of joint data/pilot tracking in environments with user dynamics and under weak signal environments.

## 6.2 Dynamic Scenarios

### 6.2.1 Scenario 1: User Dynamics under Weak Signal Conditions

The purpose of this test is to highlight the advantage of using data/pilot tracking with respect to single channel tracking under dynamic conditions. For this purpose, a receiver moving along a rectangular path is simulated using the Spirent GSS7700 hardware simulator. The velocity profile is shown in Figure 6-5. A maximum velocity of 3 m/s is chosen for the straight paths in the rectangular track and the receiver slows down at the corners and accelerates back to 3 m/s as it comes out. The velocity magnitude was chosen to imitate pedestrian dynamics.

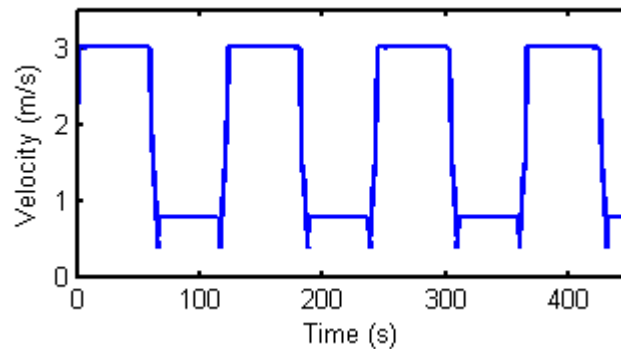


**Figure 6-5: Velocity profile of the receiver simulated using the Spirent hardware simulator**

At each turn in the trajectory, a sudden change in Doppler is observed, as shown in Figure 6-6. A PLL is not able to instantaneously follow this change, and a bias will be generated in the Doppler estimates. The goal of this test is to compare the bias in Doppler estimates for the single channel and data/pilot tracking methods at these turns. Under good  $C/N_0$  conditions, the adaptive noise bandwidth algorithm on both methods can

increase the noise bandwidth such that there is no significant difference in measured bias between them. So the test scenario is configured to observe the ability of the algorithms to maintain lock at these turns under conditions where  $C/N_0$  of the received signal is close to the tracking threshold.

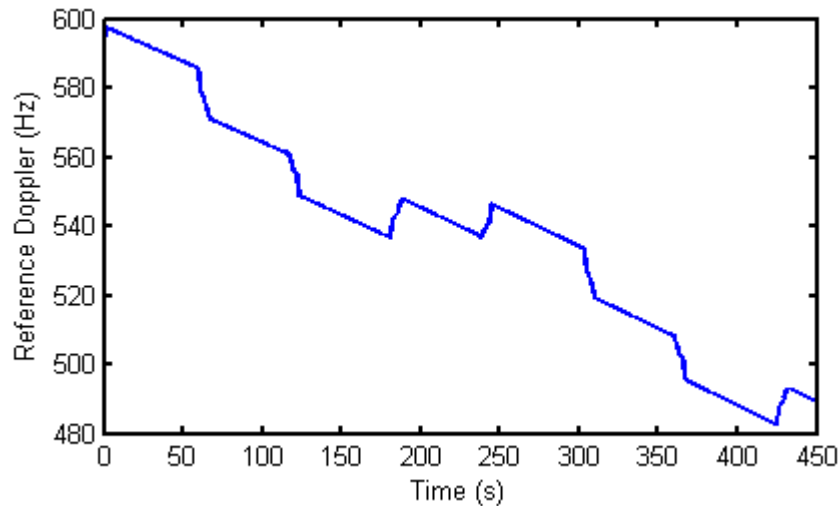


**Figure 6-6: Sample of true Doppler obtained from the Spirent hardware simulator corresponding to a rectangular trajectory**

The  $C/N_0$  profile shown in Figure 6-7 is chosen for this test. The scenario starts with a  $C/N_0$  of 32 dB-Hz across all satellites in order to acquire and start tracking the signals. On one of the straight legs in the user trajectory, shown in Figure 6-8, the signal power is gradually reduced in steps of 1 dB per second down to approximately 16 dB-Hz. The signal power is further dropped by 1 dB after allowing the vehicle to take a few turns. In this way, the  $C/N_0$  is set to equal the average tracking threshold of the DPLL-ATAN2 algorithm. It should be noted that the tracking threshold quantified in Section 6.1.2 is for a static receiver. Under dynamic conditions, the tracking threshold is expected to degrade further. Hence, the need for analysis under different  $C/N_0$  levels near the

tracking threshold. The time instants at which the  $C/N_0$  levels are changed and the user trajectory information are provided in Figure 6-8.

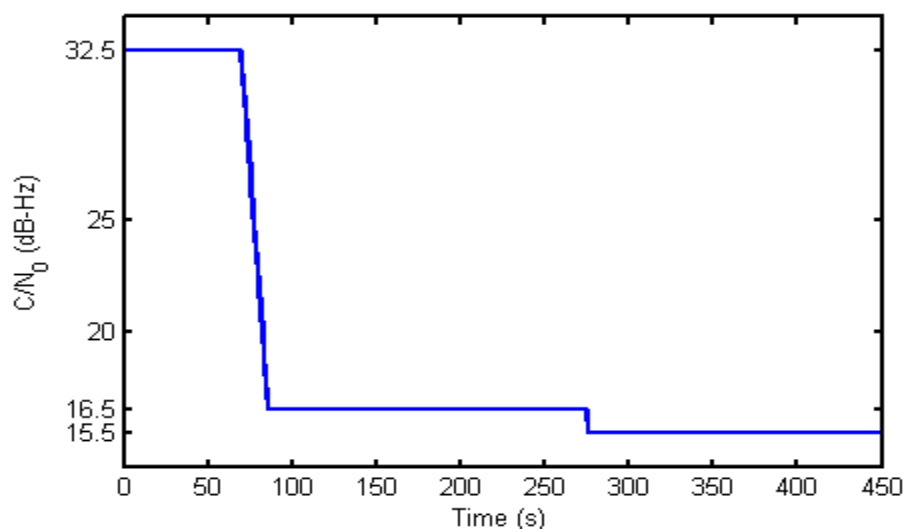


**Figure 6-7:  $C/N_0$  profile chosen for the test under user dynamics**

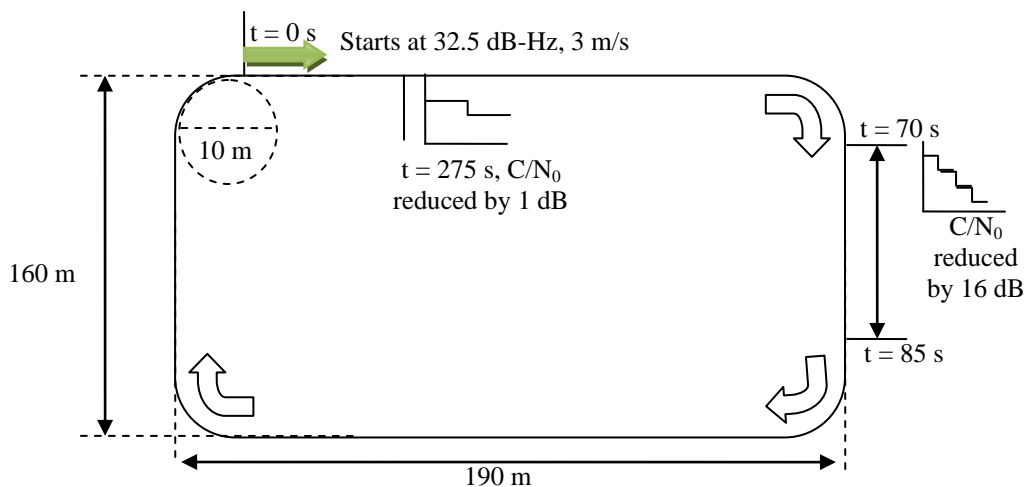


**Figure 6-8: User trajectory with  $C/N_0$  level information**

#### 6.2.1.1 Test Methodology

The setup adopted for the data collection is similar to the one shown in Figure 4-8. In this case, only one channel without any additional attenuation is collected. The data collected is processed using DPLL-ATAN2 and DPLL-Pilot independently. Only the

digitally designed tracking loops are used in this analysis. The Doppler estimates obtained from the two methods are then post-processed to extract the bias where the true Doppler values logged by the simulator are used as reference. This is subtracted from the Doppler estimates to obtain the error. The error also contains the effect of the receiver clock drift. An approximate value of the receiver clock drift is computed by averaging the difference between Doppler estimates and the reference over the initial time period corresponding to relatively high  $C/N_0$ . This is then used to remove the effect of clock drift from the Doppler estimate errors. The effect of any unaccounted clock drift is the same for single channel and data/pilot tracking and the main interest is to obtain a relative performance measure in terms of ability to maintain lock and Doppler bias. Finally, the bias is extracted by using a moving average filter to reduce the effect of thermal noise.

#### *6.2.1.2 Results*

Figure 6-9 shows a sample plot of the measured Doppler bias, the reference Doppler trajectory of the corresponding satellite, and the noise bandwidth used by the single channel (DPLL – Pilot) and data/pilot tracking (DPLL-Joint (ATAN2)) methods. The  $C/N_0$  for the results in Figure 6-9 was approximately 15.5 dB-Hz. When the user makes a turn, the Doppler frequency significantly changes and the adaptive noise bandwidth algorithm increases the loop noise bandwidth accordingly. The quantity by which the noise bandwidth can be increased during each turn depends on the  $C/N_0$  level and the step size used in the gradient descent algorithm. Under identical environment and step size configuration, the data/pilot tracking algorithm is able to choose a larger noise bandwidth as compared to single channel tracking. This is because the joint data/pilot tracking algorithm can operate in the presence of higher thermal noise since it uses

information from both data and pilot channels. This feature helps in maintaining phase lock with reduced bias in the estimated Doppler. This will be further demonstrated in the following section.

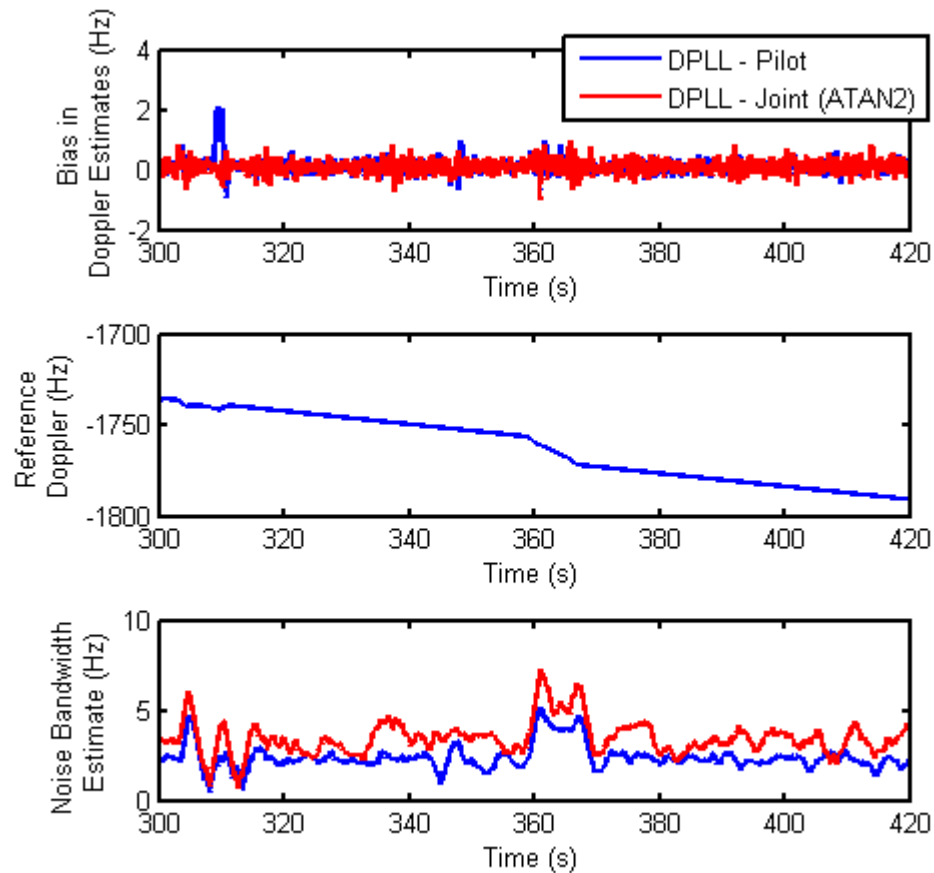


**Figure 6-9: Sample plot of noise bandwidths chosen by single channel and data/pilot tracking**

Figure 6-10 and Figure 6-11 shows sample results obtained for several satellites. The time period corresponding to 85 to 275 seconds marked in the figure corresponds to a  $C/N_0$  of 16.5 dB-Hz. Single channel tracking loses lock after facing a turn due to the dynamic stress under the chosen  $C/N_0$  condition. This behaviour is observed across multiple PRNs. In contrast, joint data/pilot tracking is able to maintain lock throughout

this time interval across all the satellites in view and loss of lock occurs only when the  $C/N_0$  is further dropped by 1 dB to 15.5 dB-Hz.

Figure 6-11 (a)-(b) provides similar results for different satellites in view. Further, as shown in Figure 6-11 (a)-(b), the bias in Doppler estimates is significantly reduced in the data/pilot tracking method as compared to single channel tracking.

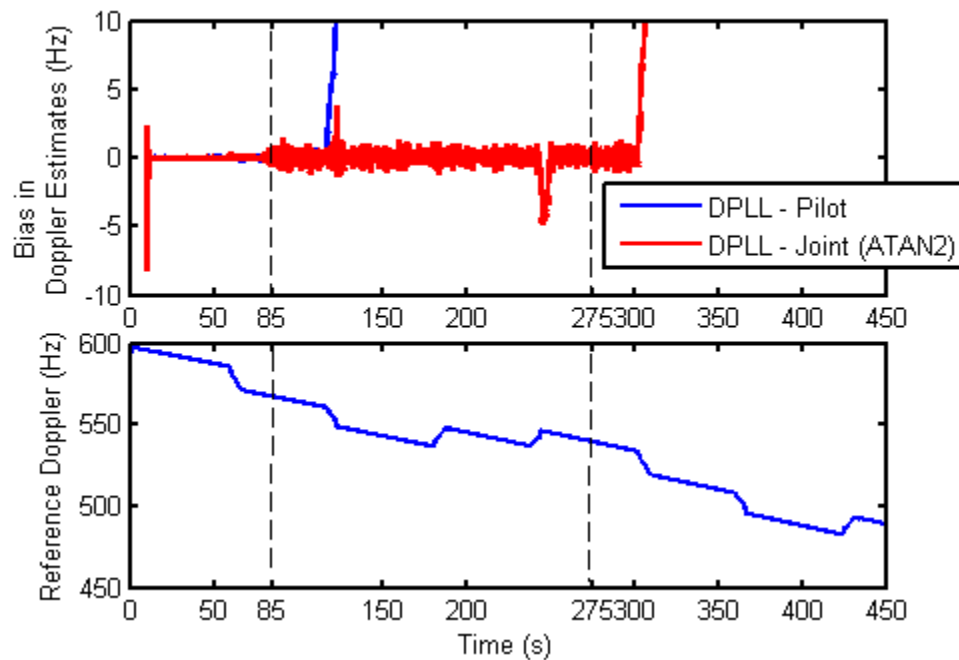
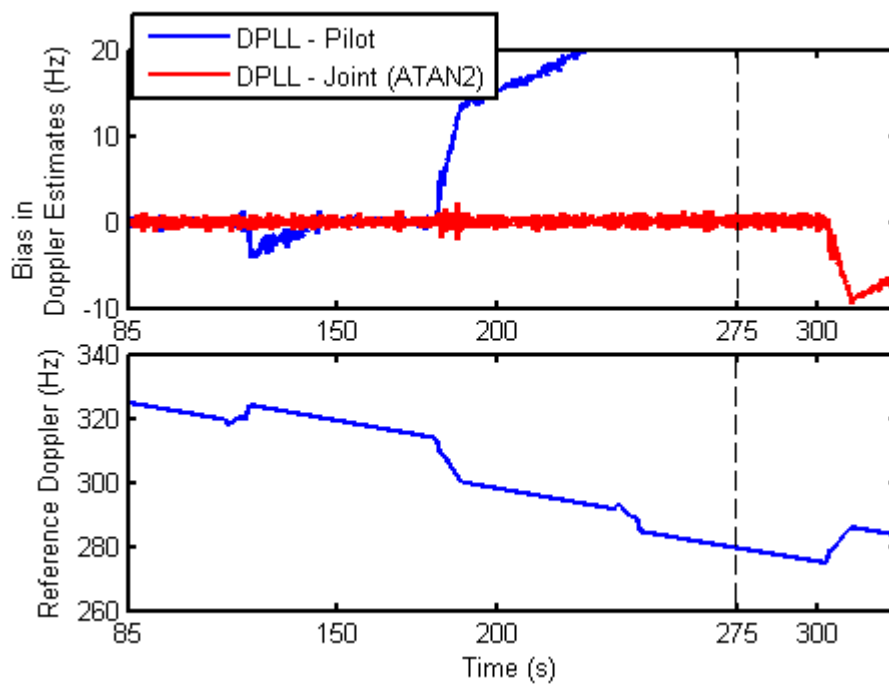
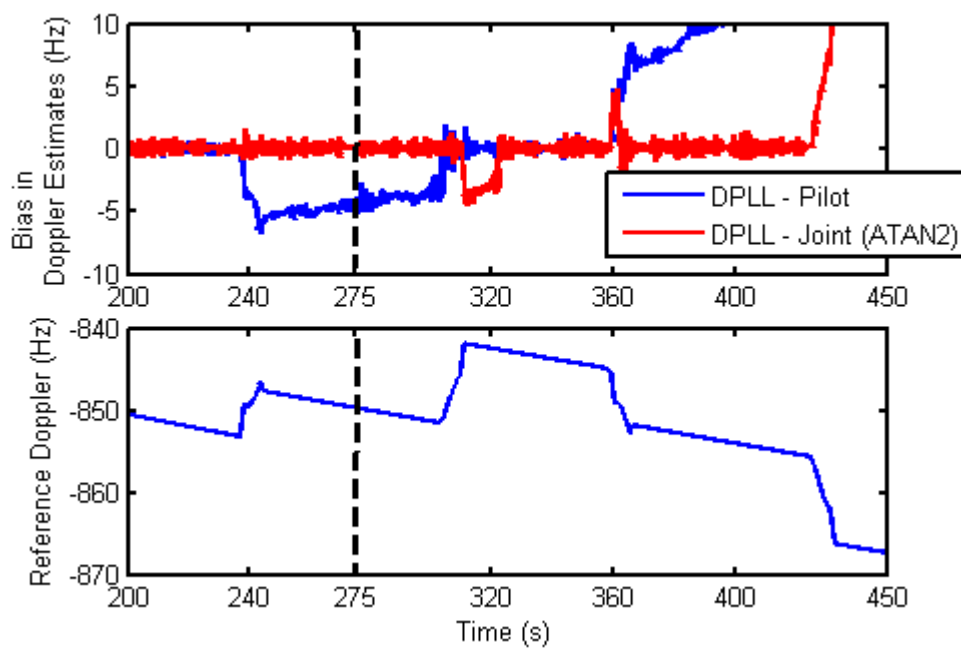


**Figure 6-10: Ability of the single channel and data/pilot tracking methods to maintain lock under (i) 85-275 s corresponding to 16.5 dB-Hz and (ii) 275-450 s corresponding to 15.5 dB-Hz. (PRN 04)**



(a) PRN 18



(b) PRN 19

**Figure 6-11: Comparison of single channel tracking with data/pilot tracking in dynamics conditions under  $C/N_0$  close to their tracking threshold**

### 6.2.2 Scenario 2: Test under Dynamics with Different Acceleration Stress

The goal of this test is to evaluate the ability of the pilot-only and joint data/pilot tracking methods to maintain lock under different acceleration stress. The scenario is configured to start with a stationary vehicle under open sky conditions (approximately 40 dB-Hz), which helps the receiver to acquire and start tracking the signal. After a fixed time interval, the vehicle gradually accelerates to a velocity of 17 m/s (approximately 61 km/h) and makes 90 degree turns with increasing acceleration (in steps of 0.5 g) at known intervals (Sokolova 2009). Two different trajectories, one with a step shape as shown in Figure 6-12, and the other with a rectangular shape similar to the one described in Figure 6-8 are simulated.

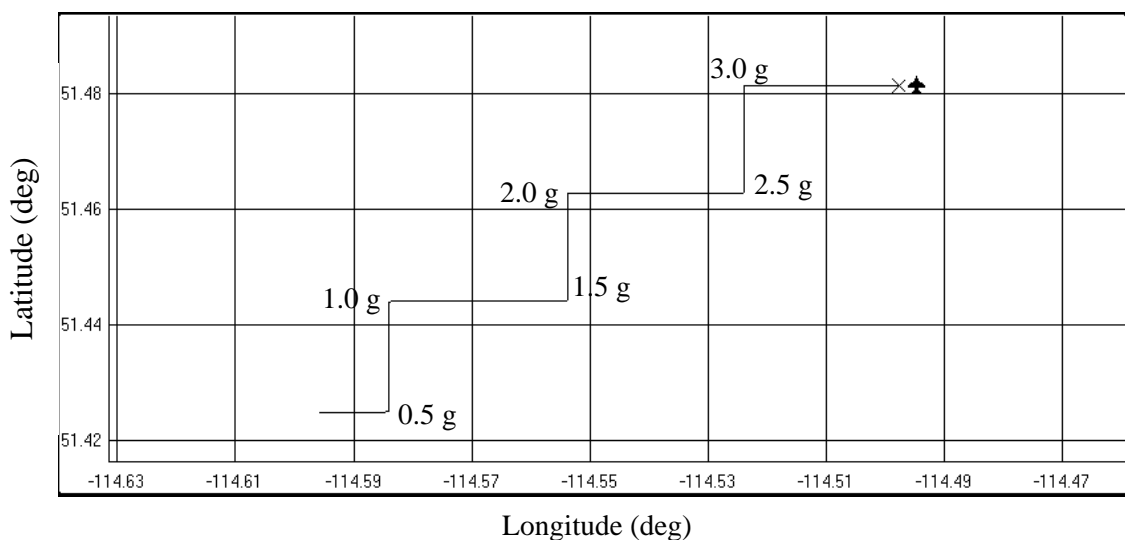


**Figure 6-12: Vehicle Trajectory with increasing acceleration stress**

The data collection setup and test methodology are identical to those of the previous scenario described in Section 6.2.1. In addition to the performance analysis based on Doppler bias and ability to maintain lock, this section also provides the  $C/N_0$  as

estimated by the receiver.  $C/N_0$  estimates drop when there is a bias in Doppler or under loss-of-lock. Thus, they can also be used to analyse the tracking performance.

### 6.2.2.1 Results

Depending on the user-satellite relative motion, the effect of user dynamics varies across different satellites. For satellites at zenith, both the joint data/pilot and pilot-only tracking methods were able to maintain lock through all turns i.e., a maximum acceleration stress of 3 g. Figure 6-13 shows the noise bandwidth estimates for one such satellite corresponding to the scenario with a rectangular trajectory. As described in the previous scenario, joint data/pilot tracking is able to operate with a larger noise

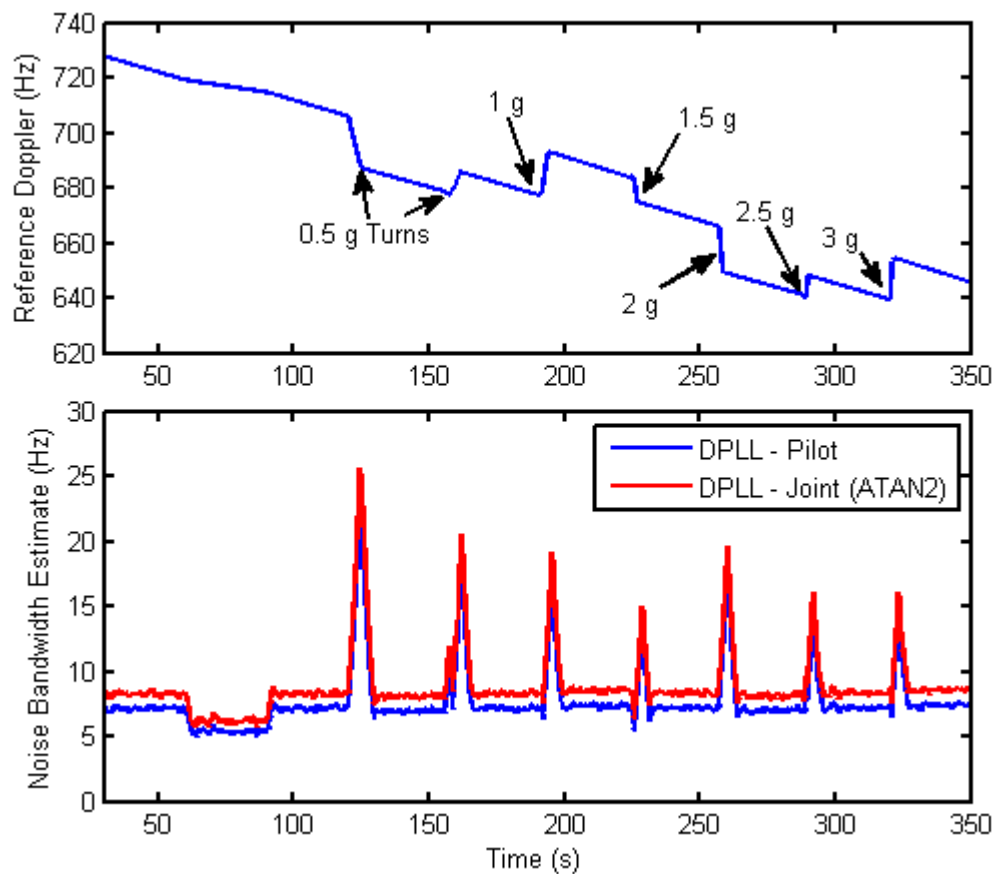


**Figure 6-13: Comparison of noise bandwidth estimate used by joint data/pilot and pilot-only tracking loops**

bandwidth as compared to pilot-only tracking.

For satellites at an elevation angle around 45 degrees, joint data/pilot tracking loses lock while making a turn with an acceleration of either 2.5 or 3 g, depending on the satellite. In contrast, pilot-only tracking loses lock when subjected to an acceleration stress of 2 g on most satellites across both the trajectories. A sample plot of the Doppler bias and measured  $C/N_0$  is shown in Figure 6-14.

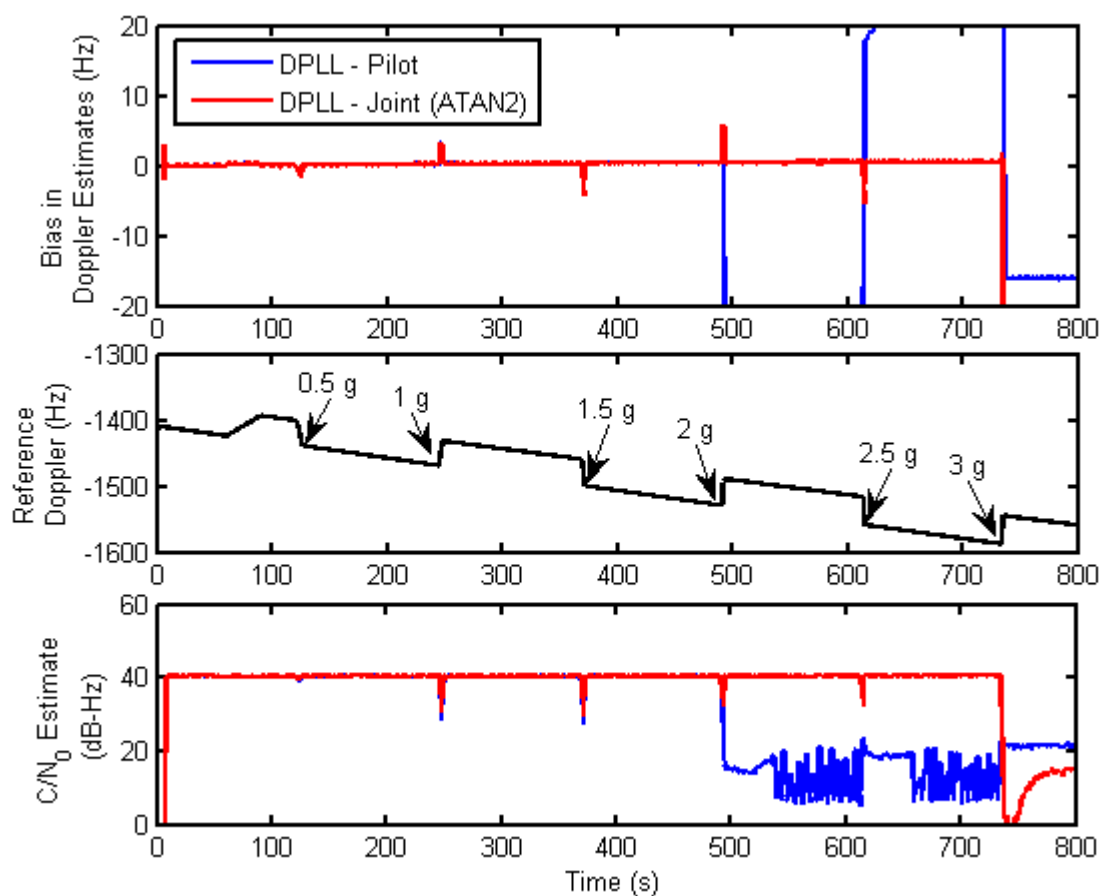


**Figure 6-14: Sample plot of bias in Doppler estimates and measured  $C/N_0$  for satellites away from zenith (elevation angle around  $45^\circ$ ) corresponding to the step trajectory**

For satellites close to the horizon, the limit of acceleration stress that the tracking loops can bear degraded by almost 1 g i.e., joint data/pilot tracking loses lock under an

acceleration stress of 1.5-2 g whereas pilot-only tracking loses lock when subjected to an acceleration stress of 1 g. Significant differences in the bias in Doppler estimates were observed while tracking a reference frequency trajectory as shown in Figure 6-15. This type of reference trajectory, with small spikes, is observed when the Doppler due to satellite motion is relatively high compared to that of the user motion.

In summary, the joint data/pilot method helps tracking a signal under higher levels of acceleration stress relative to pilot channel only tracking.

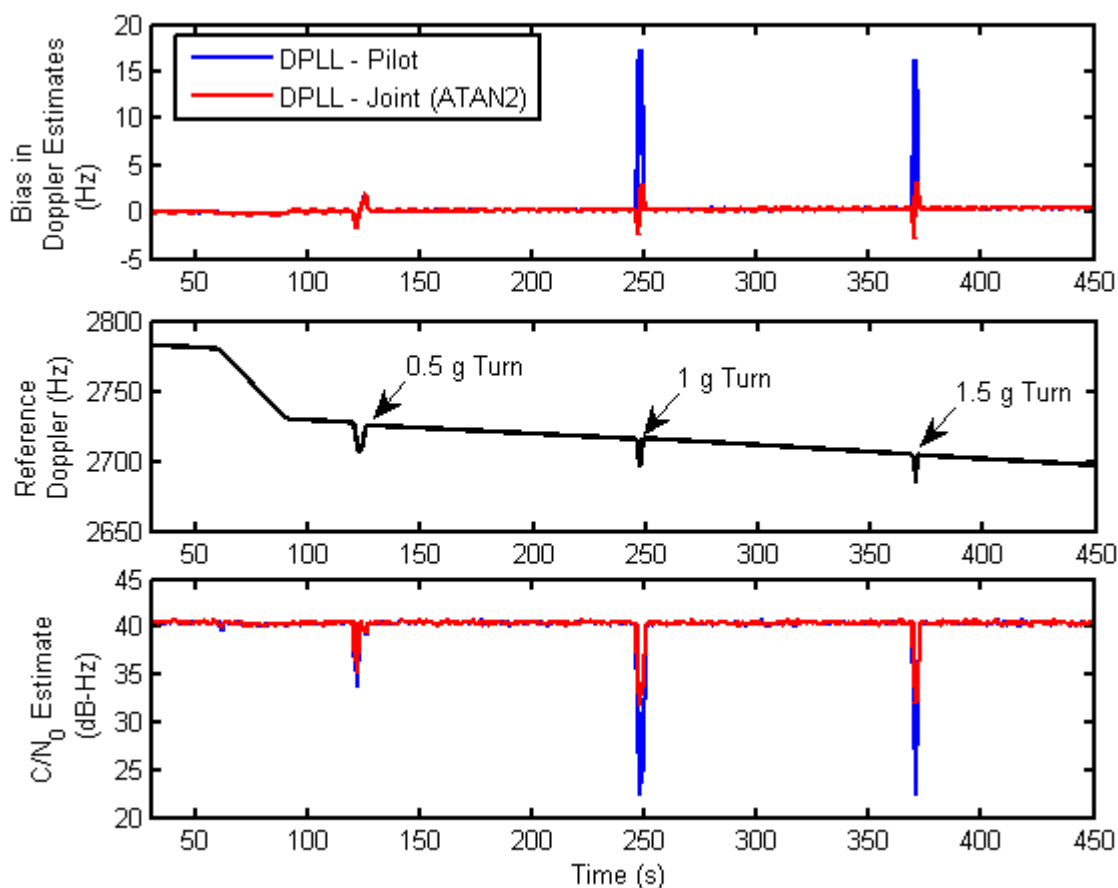


**Figure 6-15: Comparison of bias in Doppler estimates and measured  $C/N_0$  for a reference frequency trajectory with spikes due to acceleration stress (step trajectory)**

### 6.3 Summary

The tracking threshold of the proposed data/pilot tracking methods has been shown to be close (approximately 1 dB) to that of pure PLL tracking. Thus, there is no considerable degradation in using data/pilot tracking over single channel tracking. The advantage in using both channels over single channel for tracking is the ability to collect power from both channels and thus to use a larger noise bandwidth in the presence of dynamics. This helps in tracking the signal under such dynamics. In particular, this advantage has been demonstrated for an environment with user dynamics under severely attenuated conditions as well as one with increasing acceleration stress under open sky conditions. It has been shown that using the data/pilot tracking method helps in maintaining lock, reduce the bias in Doppler estimates, and reduce the time taken to regain phase lock.

## CHAPTER SEVEN: CONCLUSIONS AND RECOMMENDATIONS

This chapter summarizes the contributions of this thesis toward the goal of efficiently making use of both data and pilot channels in order to improve the performance of signal tracking and  $C/N_0$  estimation algorithms in the context of modernized GNSS signals. Finally, recommendations for possible future work that can complement the presented results are provided.

### 7.1 Conclusions

The purpose of this thesis, as stated in Chapter 1, was to

- i. identify issues with joint data/pilot tracking;
- ii. analyse the impact of those issues;
- iii. propose methods to overcome the identified issues;
- iv. analyse the performance of the proposed methods against pilot-channel-only tracking.

In order to establish a reliable metric to analyse the performance of the tracking algorithms, the problem of reliable  $C/N_0$  estimation was also addressed.

#### 7.1.1 Reliable $C/N_0$ Estimation

A comprehensive theoretical analysis of  $C/N_0$  estimation was provided, with emphasis on using both the data and the pilot channels. The CRLB derived for  $C/N_0$  estimation helped in understanding the following aspects:

- i. the noise variance reduction achievable in using both the data and the pilot channels for  $C/N_0$  estimation gradually diminishes for signals weaker than 25 dB-Hz;

- ii. the CRLB for  $C/N_0$  estimation using correlator outputs accumulated over shorter predetection intervals ( $T_{coh}$ ) is shown to be lower than the one using observations with longer  $T_{coh}$ ; a choice of  $T_{coh} = 1$  ms with the knowledge of 20 observations per data bit was shown to avoid information loss as compared to the use of  $T_{coh} = 20$  ms where the data bit sign reverses with every observation.

The bounds presented in this thesis can be used as a reference in the performance analysis of any joint data/pilot  $C/N_0$  estimator. Further, a maximum-likelihood (ML) estimator that uses both data and pilot channels was derived. The approximation used in deriving the ML estimators was shown to degrade in performance for signals weaker than 25 dB-Hz, and the degradation being manifested as a bias in the estimates. Hence, the joint data/pilot estimator with approximation is unreliable for weak signals. An iterative solution was proposed to overcome this issue and a detailed analysis was presented. The proposed joint data/pilot iterative ML estimator has been demonstrated to be reliable for estimating  $C/N_0$  down to 17 dB-Hz. For lower  $C/N_0$  values, standard tracking loops (with constant noise bandwidth) lose lock, and the  $C/N_0$  cannot be estimated. However, as is evident from the numerical simulation results, the estimator is less biased even for  $C/N_0$  lower than 17 dB-Hz.

### **7.1.2 Joint Data/Pilot Carrier Frequency Tracking**

The purpose of Chapter 4 was to outline issues related to joint data/pilot carrier frequency tracking, to provide a detailed performance analysis of said tracking, and to use the knowledge gained to design methods for joint data/pilot carrier phase tracking.

One of the issues in joint data/pilot frequency tracking is the increase in noise variance of the frequency error estimates under weak  $C/N_0$  conditions, due to the non-linear nature of the discriminators used. An application of on-the-fly variance estimators (Moir 2001) to compute the weights was demonstrated to overcome this issue. Finally, a performance analysis was presented for two differently-weighted discriminator combinations, with emphasis on performance under weak  $C/N_0$  conditions. The Costas discriminator combination, which uses cross product discriminators with decision feedback ( $D_{df}$ ) on both the data and pilot channels, was shown to suffer from significant degradation in tracking threshold. The only advantage of the Costas discriminator combination is in operation under moderate-to-strong signal conditions. Further, using identical discriminators on both data and pilot channels allows one to assign equal weights in the combination eliminating extra computational burden from the weight computation algorithm. The discriminators used by the standard discriminator combination on the data and pilot channels are different. The analysis provided in this thesis used a cross product ( $D_{cross}$ ) discriminator on the pilot channel and a cross product with decision feedback ( $D_{df}$ ) discriminator on the data channel. With proper weighting, the standard discriminator combination was shown to acquire and maintain frequency lock over the same levels of attenuation as an FLL running solely on the pilot channel. However, under weak  $C/N_0$  conditions, some degradation in frequency jitter was observed by using a standard discriminator combination as compared to pilot-channel-only tracking. This was explained as the effect of the change in discriminator gain due to data bit decision errors in  $D_{df}$ , which were unaccounted for in the design.

The results obtained in this chapter demonstrated the importance of the discriminator linearity region and appropriate weighting in joint data/pilot tracking, which is utilized in the design of methods in the subsequent chapters.

### **7.1.3 Joint Data/Pilot Carrier Phase Tracking**

Chapter 5 discusses problems specific to joint data/pilot carrier phase tracking. Two different methods were proposed to overcome problems arising in joint data/pilot phase tracking. One method is an extension of the weighted discriminator combination available in the literature for standard tracking architecture, whereas the other utilizes a Kalman filter-based architecture.

For joint data/pilot tracking with a weighted discriminator combination, utilizing ATAN2 discriminators on both data and pilot channels was shown to help in reducing the bias in the estimates under weak  $C/N_0$  conditions, mitigating the impact of the reduced phase pull-in range of Costas discriminators. In order to use an ATAN2 discriminator on the data channel, a data bit decision process as explained in Chapter 5 has been used. This process introduces noise due to an increase in data bit decision errors under weak  $C/N_0$  conditions. This has been accounted for in the computation of weights in the combination (using on-the-fly weight computation), as well as in the cost function of the noise bandwidth adaptation algorithm. Further, the design of the PLL in the digital domain helped in accurately predicting the effect of thermal noise and dynamic stress for a given scenario. These design considerations led to a more stable design of joint data/pilot tracking with adaptive noise bandwidth. From the results presented in Chapter 6, it is evident that the proposed method suffers no significant loss (less than 1 dB) in tracking sensitivity as compared to pilot-channel-only tracking.

A second approach for joint data/pilot tracking is provided using a Kalman filter (KF). The tracking sensitivity performance of KF-based joint data/pilot tracking in a static environment has been demonstrated to be similar to that of the previous method. In summary, both proposed methods demonstrated the ability to maintain lock over the same level of attenuation as a pure PLL on the pilot channel. Through comparison of the two proposed methods, it became apparent that the method based on the standard architecture is able to provide performance similar to a KF-based architecture for a static receiver, with less computational burden.

Chapter 6 also highlights the advantage of using a joint data/pilot over a single channel tracking for scenarios with user dynamics in severely attenuated conditions and increasing acceleration stress under open sky conditions. Since joint data/pilot tracking methods can make use of the power from both data and pilot channels, the effect of tracking jitter due to thermal noise is reduced as compared to single channel tracking. Thus, joint data/pilot tracking methods can use a larger noise bandwidth in the presence of dynamics. The results obtained in Chapter 6 under dynamic scenarios with a user taking several turns demonstrate the advantages of joint data/pilot tracking in reducing the bias in Doppler estimates, the time taken to regain phase lock, and, most importantly, to maintain phase lock under these conditions.

In summary, the proposed joint data/pilot phase tracking algorithms can help in utilizing both data and pilot channel information, without significantly losing the inherent advantages of a pure PLL.

## 7.2 Recommendations for Future Work

Following the conclusions made in this chapter, this section lists the limitations of this thesis and makes recommendations for future work:

- i. The CRLB derived for the  $C/N_0$  estimation process assumed real observations and the ML estimators are also derived based on real inputs. In reality, the signal power is split across in-phase and quadrature arms due to phase tracking errors, resulting in complex accumulated correlator outputs. Thus, a complete derivation of the bound and ML estimator, including the effect of phase error, would give a more accurate analysis.
- ii. The Newton-Raphson method is used to solve the ML equation for deriving the  $C/N_0$  estimators. The computational load can be reduced by considering other approximations of the  $\tanh$  function to solve the ML equation. For example, the  $\tanh$  function can be approximated as (Kwan 1992)

$$\tanh(x) \approx \begin{cases} +1 & x \geq x_s \\ x(\beta - Kx) & 0 \geq x > x_s \\ x(\beta + Kx) & -x_s \geq x > 0 \\ -1 & x \leq -x_s \end{cases} \quad (7.1)$$

where  $\beta$  and  $K$  represents the slope and gain of the non-linear approximation of the  $\tanh$  function in the region between  $-x_s < x < x_s$ .

$x_s$  represents the limit beyond which the  $\tanh$  function saturates to unity.

A similar approximation for the  $\tanh$  function can be found in Anguita et al (1993). A special case of this approximation can be used to arrive at the following approximation:

$$\tanh(x) \approx \begin{cases} \text{sgn}(x) & |x| \geq x_s \\ x & |x| \leq x_s \end{cases} \quad (7.2)$$

which utilizes  $\beta = 1$  and  $K = 0$ . Intuitively, the above approximation might still lead to a biased estimate of  $C/N_0$  as a linear approximation,  $\tanh(x) \approx x$ , which does not exactly represent the *tanh* function under weak  $C/N_0$  conditions. However, this might yield a  $C/N_0$  estimator with less computational complexity that can be utilized in real-time applications.

- iii. Based on the analysis of issues and methods available for joint data/pilot carrier frequency tracking provided in this thesis, a method that accounts for the gain variation in non-linear frequency discriminators under weak  $C/N_0$  conditions may aid in obtaining a more robust FLL.
- iv. The adaptive noise bandwidth algorithm proposed in Chapter 3 is derived and analyzed for a second-order PLL. This algorithm can be extended to a third-order PLL using numerical techniques. In a third-order PLL, the error due to dynamics is from jerk rather than phase acceleration, as in the case of a second-order PLL (Gardner 2005). This extension might help in addressing a larger portion of the navigation community, as third-order PLLs are commonly used in many applications.
- v. Identical predetection intervals ( $T_{coh}$ ), limited to a data bit period ( $T_{coh} \leq 20$  ms) have been assumed in both the data and pilot channels for implementation simplicity. Alternative options using  $T_{coh}$  longer than a data bit period have been provided by Tran & Hegarty (2002) and Ziedan

(2005). In both these options, the tracking loop update is done at the end of a longer predetection interval on the pilot channel. During this period, the accumulated correlator output corresponding to each data bit period is collected on the data channel and, finally, these are combined after accounting for the data bit presence through data bit detection algorithms or external aiding. Although this methodology may help with weak signal tracking, the performance under dynamics may be severely degraded due to low update rates. Thus, a joint data/pilot tracking scheme with asynchronous updates across data and pilot channels may provide better performance under weak signals (with longer  $T_{coh}$  on the pilot channel) as well as dynamic scenarios (with shorter  $T_{coh}$  on the data channel).

- vi. The proposed algorithms were analysed in terms of tracking performance. A detailed analysis of joint data/pilot tracking with regard to positioning accuracy may be helpful.

Including the above changes may help in implementing the proposed joint data/pilot tracking or  $C/N_0$  estimation techniques in commercial receivers.

**REFERENCES**

- Abbasiannik, S. (2009), **Multichannel Dual Frequency GLONASS Software Receiver in Combination with GPS L1 C/A**, M.Sc Thesis, Published as Report No. 20286, Department of Geomatics Engineering, University of Calgary, Canada
- Akos, D.M, P.L. Normark, J. Lee, K.G. Gromov, J.B.Y. Tsui and J.Schmaus (2000), **Low Power Global Navigation Satellite System (GNSS) Signal Detection and Processing**, ION GPS 2000, 19-22 Sep 2000, Salt Lake City, UT, pp.784-791
- Alagha, N.S. (2001), **Cramer-Rao Lower Bounds of SNR Estimates for BPSK and QPSK Modulated Signals**, IEEE Communications Letters, Vol. 5, No.1, January 2001, pp. 10-12
- Anghileri, M., T. Pany, J. Won and G.W. Hein (2006), **An Algorithm for Bit Synchronization and Signal Tracking in Software GNSS Receivers**, ION GNSS 19<sup>th</sup> International Technical Meeting of the Satellite Division, 26-29 Sep 2006, Fort worth, TX, pp.1836-1848
- Anguita. D., G. Parodi and R. Zunino (1993), **Speed Improvement of the Back-Propagation on Current Generation Workstations**, Proceedings of the World Congress on Neural Networking, Portland, Oregon, 1993, Vol. 1, pp. 165-168, Lawrence Erlbaum/INNS Press
- Betz, J.W., M.A. Blanco, C.R. Cahn, P.A. Dafesh, C.J. Hegarty, K.W. Hudnut, V. Kasemsri, R. Keegan, K. Kovach, L.S. Lenahan, H.H. Ma, J.J. Rushanan, D. Sklar, T.A. Stansell, C.C. Wang and S.K. Yi (2007), **Enhancing the Future of Civil GPS – Overview of the L1C Signal**, Inside GNSS – Spring 2007, pp. 42-

49, available at [http://www.insidegnss.com/auto/igm\\_042-049.pdf](http://www.insidegnss.com/auto/igm_042-049.pdf), accessed on 30-Nov-2009

Chen, Y. and N.C. Beaulieu (2005), **An Approximate Maximum Likelihood Estimator for SNR Jointly Using Pilot and Data Symbols**, IEEE Communications Letters, Vol.9, No.6, June 2005, pp.517-519

Crosta, P. (2009), **A Novel Approach to the Performance Evaluation of an Arctangent Discriminator for Phase Locked Loop and application to the carrier tracking of the Ionospheric Scintillation**, European Navigation Conference - Global Navigation Satellite Systems (ENC-GNSS) 2009, May3-6, Naples, Italy

Dedes, G. and A.G. Dempster (2005), **Indoor GPS Positioning - Challenges and Opportunities**, IEEE 62<sup>nd</sup> Vehicular Technology Conference, VTC – Fall 2005, Vol 1, 28-25 Sep 2005, pp. 412-415

Dempster, A. (2006), **Correlators for L2C - Some considerations**, Inside GNSS, September 2006, pp. 40-45

Fontana, R.D., W. Cheung, P.M. Novak and T.A. Stansell Jr. (2001), **The New L2 Civil Signal**, ION GPS 2001, 11-14 September 2001, Salt Lake City, UT

Gardner, F.M. (2005), **Phase Lock Techniques**, Third Edition, Jhon Wiley & Sons, Inc., USA

Gao, G.X., A. Chen, S. Lo, D. De Lorenzo, T. Walter and P. Enge (2008), **Compass – M1 Broadcast Codes and Their Application to Acquisition and Tracking**, Proceedings of the 2008 National Technical Meeting of the Institute of Navigation, January 28 - 30, 2008, San Diego, California

- Gernot, C., K. O'Keefe and G. Lachapelle (2008), **Combined L1/L2C Tracking Scheme for Weak Signal Environments**, Proceedings of ION-GNSS08, Savannah, GA, 16-19 Sep, Session C4, The Institute of Navigation, 15 pages
- Gernot, C., S.K. Shanmugam, K. O'Keefe and G. Lachapelle (2007), **A Novel L1 and L2C Combined Detection Scheme for Enhanced GPS Acquisition**, Proceedings of ION - GNSS07, Forth Worth, 25-28 Sep, Session C1, The Institute of Navigation, 12 pages
- Gibbons, G. (2008), **Russia Approves CDMA Signals for GLONASS, Discussing Common Signal Design**, Inside GNSS 2008 article, April 28, 2008
- Giove (2008), **GIOVE Mission Objectives**, accessed on 2-Dec-2008, available at [http://www.giove.esa.int/page\\_index.php?menu=100&page\\_id=33](http://www.giove.esa.int/page_index.php?menu=100&page_id=33)
- Groves, P.D. (2005) **GPS Signal to Noise Measurement in Weak Signal and High Interference Environments**, Proceedings of ION GNSS 2005, Long Beach, CA, Institute of Navigation, 643-658
- Hadrell, T. and A.R. Pratt (2001), **Understanding the Indoor GPS Signal**, ION GPS 2001, 11- 14 September 2001, Salt Lake City, UT, pp. 1487-1499
- Hegarty, C.J., (1999), **Evaluation of the proposed Signal Structure for the New Civil GPS Signal at 1176.45 MHz**, MITRE center for Advanced Aviation System Development, Working Note June 1999, Chapter 3
- Information – Analytical Centre (2009), **GLONASS Constellation Status**, Status Information Group, accessed on Nov 16, 2009, available at <http://www.glonass-ianc.rsa.ru/pls/htmldb/f?p=202:20:14637162736231801312::NO>

- IS-GPS-200-D (2006), **Interface Specification IS-GPS-200, Revision D**, Interface Revision Notice (IRN)-200D-001, 7 March 2006, Navstar GPS Space Segment / Navigation User Interface
- Julien, O. (2005), **Carrier Phase Tracking of Future Data/Pilot Signals**, ION GNSS 2005, Long Beach, CA, September 13-16, 2005
- Kaplan, E. (2006), **Understanding GPS: Principles and Applications**, Artech House, Chapter 5, pp. 153-241
- Kay, S.M (1993), **Fundamentals of Statistical Signal Processing – Estimation Theory**, Vol.1, Prentice Hall Signal Processing Series
- Kazemi, P.L. and C.O'Driscoll (2008), **Comparison of Assisted and Stand-Alone Methods for Increasing Coherent Integration Time for Weak GPS Signal Tracking**, Proceedings of 21<sup>st</sup> International Technical Meeting of the Satellite Division ION GNSS 2008, Sep 16-19, 2008, Savannah, GA, pp.1730-1740
- Kwan, H.K (1992), **Simple sigmoid-like activation function suitable for digital hardware implementation**, IEEE Electronic Letters, Vol. 28, Issue. 15, pp. 1379-1380, Publication date – 16-July-1992
- Lashley, M and D.M. Bevly (2008), **A Comparison of Performance of a Non-Coherent Deeply Integrated Navigation Algorithm and a Tightly Coupled Navigation Algorithm**, Proceedings of 21<sup>st</sup> International Technical Meeting of the Satellite Division ION GNSS 2008, Sep 16-19, 2008, Savannah, GA, pp.2123-2129
- Ledvina, B.M, M.L. Psiaki, D.J. Sheinfield, A.P. Cerruti, S.P. Powell and P.M. Kintner (2004), **A Real Time GPS Civilian L1/L2 Software Receiver**, in the Proceeding

of Institute of Navigation GPS 2004, 21-24 September, Long beach CA, pp.986-1005

Li, B., R. DiFazio and A.Zeira (2002), **A Low Bias Algorithm to Estimate Negative SNRs in an AWGN Channel**, IEEE Communications Letters, Vol. 6, No.11, November 2002, pp.469-471

Ling, F. (1996), **Convergence and Optimum MSE of Digital Frequency Locked Loop for Wireless Communications**, IEEE 46<sup>th</sup> Vehicular Technology Conference, 1996. 'Mobile Technology for the Human Race', 28 April-1 May 1996, Volume 2, pp.1215 – 1219

Macabiau, C., L.Ries, F.Bastide and J.L.Issler (2003), **GPS L5 Receiver Implementation Issues**, *ION-GPS/GNSS 2003*, 9-12 Sep 2003, Portland, OR, pp. 153-164

Moir,T.J. (2001), **Automatic Variance Control and Variance Estimation Loops**, *Journal of Circuits, Systems and Signal Processing*, Jan 2001, pp. 1-10, Volume 20 No 1

Mongrédien, C. (2008), **GPS L5 Software Development for High-Accuracy Applications**, PhD Thesis, published as UCGE Report No. 20268, Department of Geomatics Engineering, University of Calgary, Canada

Mongrédien, C., M.E.Cannon and G.Lachapelle (2007), **Performance Evaluation of Kalman Filter based Tracking for the New GPS L5 Signal**, Proceedings of the 20th International Technical Meeting of the Satellite Division of the Institute of Navigation ION GNSS 2007, September 25 - 28, 2007, Fort Worth, Texas, pp. 749-758

- Mongrédién,C., G.Lachapelle and M.Cannon (2006), **Testing GPS L5 Acquisition and Tracking Algorithms Using a Hardware Simulator**, ION GNSS 2006, Fortworth, TX, 26-29 Sep 2006, pp.2901-2912
- Muthuraman, K. (2009), **Theoretical Bounds and Reliable  $C/N_0$  Estimation for Modernized GPS Signals**, The Institute of Navigation (ION) – GNSS 2009, Session F6a, Sep 22- 25, 2009, Savannah, Georgia, 9 pages
- Muthuraman, K., R.Klukas and G.Lachapelle (2008), **Performance Evaluation of L2C Data/Pilot Combined Carrier Tracking**, ION-GNSS 21<sup>st</sup> International Technical Meeting of the Satellite Division, 16-19 Sep 2008, Savannah, GA, pp.1658-1666
- Natali, F.D. (1986), **Noise Performance of a Cross-Product AFC with Decision Feedback for DPSK signals**, IEEE Transactions on Communications, Vol. 34, Issue 3, March 1986, pp. 303-307
- NI PXI 5661 (2006), 2.7 GHz RF Vector Signal Analyzer with Digital Downconversion, National Instruments, <http://www.ni.com/pdf/products/us/catvectorsignalanalyzer.pdf>, 2006
- NovAtel 701G (2009), GPS- 701-GG and GPS-702-GG Pinwheel Antenna Datasheet, available at [http://www.novatel.com/Documents/Papers/GPS701\\_702GG.pdf](http://www.novatel.com/Documents/Papers/GPS701_702GG.pdf), retrieved on June 29, 2009
- O’Driscoll, C., and G. Lachapelle (2009), **Comparison of Traditional and Kalman Filter Based Tracking Architectures**, Proceedings of European Navigation Conference 2009 (ENC09), Naples, Italy (3-6 May), 10 pages

- Oppenheim, Alan V. and R.W. Schaffer (1999), **Discrete-Time Signal Processing**,  
Second Edition, Prentice Hall Signal Processing Series
- OS SIS ICD (2006), **Galileo Open Service Signal in Space Interface Control  
Document**, Draft 0, Dt. 23-May-2006, GAL OS SIS ICD/D.0
- Pany, T. and B.Eissfeller (2006), **Use of a Vector Delay Lock Loop Receiver for GNSS  
Signal Power Analysis in Bad Signal Conditions**, IEEE/ION Position, Location  
And Navigation Symposium, PLANS, Apr 25-27, 2006, pp. 893-903
- Pauluzzi, D.R. and N.C.Beaulieu (2000), **A Comparison of SNR Estimation  
Techniques for the AWGN Channel**, IEEE Transactions on Communications,  
Vol. 48, No.10, October 2000, pp.1681-1691
- Petovello, M.G., C. O'Driscoll, G. Lachapelle, D. Borio, H. Murtaza (2008),  
**Architecture and Benefits of an Advanced GNSS Software Receiver**,  
International Symposium on GPS/GNSS 2008, November 11-14, Tokyo, Japan,  
11 pages
- Petovello, M.G, and G. Lachapelle (2006), **Comparison of Vector-Based Software  
Receiver Implementations with Application to Ultra-Tight GPS/INS  
Integration**, ION GNSS 19th International Technical Meeting of the Satellite  
Division, 26-29 September 2006, Fort Worth, Texas, pp. 1790-1799
- PNT (2007), **Selective Availability – Information regarding the Sep-2007 decision**,  
Space based Positioning Navigation and Timing, National Executive Committee  
site, <http://pnt.gov/public/sa/>
- Polischuk, G.M., V.I. Kozlov, V.V. Ilitchov, A.G.Kozlov, V.A.Bartenev, V.E.Kossenko,  
N.A. Anphimov, S.G. Revinykh, S.B. Pisarev, A.E. Tyulyakov, B. V.

- Shebshaevitch, Mr. A. B. Basevitch and Y. L. Vorokhovsky (2002), **The Global Navigation Satellite System GLONASS : Development and Usage in the 21<sup>st</sup> Century**, 34<sup>th</sup> Annual Precise Time and Time Interval Meeting, pp. 151-160
- Press, W.H., S.A. Teukolsky W.T. Vetterling and B.P. Flannery (2007), **Numerical Recipes – The Art of Scientific Computing**, Third Edition, Cambridge University Press, pp.456-458
- Psiaki, M.L., and H. Jung (2002), **Extended Kalman Filter Methods for Tracking Weak GPS Signals**, ION GPS 2002, 24-27 Sep 2002, Portland, OR, pp. 2539-2553
- Ramasubramanian, K. and S.Nadig (2006), **Performance Bounds for Carrier-to-Noise Ratio Estimation in GPS Receivers**, ION NTM 2006, 18-20 January 2006, Monterey, CA, pp. 953-957
- Ray, J. (2007), **Advanced GNSS Receiver Technology**, ENGO 638 Notes, Department of Geomatics Engineering, University of Calgary, Calgary, Canada
- Ries, L., C. Macabiau, O. Nouvel, Q. Jeandel, W. Vigneau, V. Calmettes and JL. Issler (2002), **A Software Receiver For GPS-IIIF L5 Signal**, ION-GPS 2002, 24-27 September 2002, Portland, OR, pp. 1540-1553
- SATNAV (2006), **ISRO Industry Meet on Satellite Navigation**, ISRO Satellite Centre, Bangalore, July 4, 2006, accessed on 2-Dec-2008, News Letter available at <http://www.isro.org/newsletters/spaceindia/aprsep2006/Satnavindustry.htm>

- Schmid, A. and A. Neubauer (2005), **Carrier to Noise Power Estimation for Enhanced Sensitivity Galileo/GPS Receivers**, IEEE 61<sup>st</sup> Vehicular Technology Conference, 2005, Spring, Vol.4, pp.2629-2633
- Shanmugam, S. (2008), **New Enhanced Sensitivity Detection Techniques for GPS L1 C/A and Modernized Signal Acquisition**, PhD Thesis, published as Report No. 20264, Department of Geomatics Engineering, University of Calgary, Canada
- Skone, S. (2005), **Atmospheric Effects on Satellite Navigation Systems**, ENGO 633 Lecture Notes, Department of Geomatics Engineering, University of Calgary
- Sokolova, N. (2009), **Doppler Measurements and Velocity Estimation Indoor: Comparison of Standard and High Sensitivity Receivers**, MSc Thesis, published as Report No. 20299, Department of Geomatics Engineering, The University of Calgary, Canada
- Spilker Jr, J.J. and A.J. Van Dierendonck (1999), **Proposed New Civil GPS Signal at 1176.45 MHz, ION-GPS 1999**, 14-17 September 1999, Nashville, TN, pp. 1717-1725
- The White House (2000), **Statement by the President regarding the United States' decision to stop degrading global positioning system accuracy**, Office of the Press Secretary, Accessed on 25-Nov-2008, available at [http://www.ngs.noaa.gov/FGCS/info/sans\\_SA/docs/statement.html](http://www.ngs.noaa.gov/FGCS/info/sans_SA/docs/statement.html),
- Tran, M., and C.Hegarty (2003), **Performance Evaluations of the New GPS L5 and L2 Civil (L2C) Signals**, ION NTM 2003, 22-24 January 2003, Anaheim, CA, pp. 521-535

- Tran, M., and C.Hegarty (2002), **Receiver Algorithms for the New Civil GPS Signals**, ION NTM 2002, 28-30 January 2002, San Diego, CA, pp. 778-789
- Tsui, J. B.Y (2000), **Fundamentals of Global Positioning System Receivers: A Software Approach**, Wiley Series in Microwave and Optical Engineering, Series Editor: Kai Chapt, Chapter 3, pp. 39-43
- u-blox ANN-MS (2009), **ANN-MS Active GPS Antenna Data Sheet**, u-blox, Document ID: GPS-X-02021-D3, Rev D3, 16-Jan-2009 retrieved from [http://www.u-blox.com/images/downloads/Product\\_Docs/ANN\\_Data\\_Sheet\(GPS-X-02021\).pdf](http://www.u-blox.com/images/downloads/Product_Docs/ANN_Data_Sheet(GPS-X-02021).pdf) on Jun 29, 2009
- U-blox (2008), **UBX-G5000 / UBX-G0010 – Technical Specification**, available at accessed on 25-Nov-2008, [http://www.u-blox.com/products/ubx-g5000\\_ubx-g0010.html](http://www.u-blox.com/products/ubx-g5000_ubx-g0010.html)
- USNO (2009), **United States Naval Observatory – Block II Satellite Information**, accessed on 17-Nov-2009, available online at <ftp://tycho.usno.navy.mil/pub/gps/gpsb2.txt>
- Van Dierendonck, A.J. (1995), **GPS Receivers**, B.Parkinson and J.J.Spilker, Jr., eds., Global Positioning System: Theory and Applications, Volume 1, Chapter 8. American Institute of Aeronautics and Astronautics, Inc., Washington D.C., USA
- Van Dierendonck, A.J, P.Fenton and T.Ford (1992), **Theory and Performance of Narrow Correlator Spacing in a GPS Receiver**, Navigation: Journal of the Institute of Navigation, Vol 39, No.3, Fall, pp.265-283

- Ward, P.W., J.W. Betz and C.J. Hegarty (2006), **Understanding GPS: Principles and Applications**, Artech House, Chapter 5, Satellite Signal Acquisition, Tracking, and Data Demodulation, Second Edition, pp. 153-241
- Woo, K.T. (1999), **Optimum Semicodeless Carrier Phase Tracking of L2**, 12<sup>th</sup> International Technical Meeting of the Satellite Division of the Institute of Navigation, Nashville, Tennessee, September 14-17, 1999, 17 pages
- Ziedan, N.I. (2005), **Extended Kalman Filter Tracking and Navigation Message Decoding for Weak GPS L2C and L5 signals**, ION-GNSS 18<sup>th</sup> International Technical Meeting of the Satellite Division, 13-16 Sep 2005, Long Beach, CA, pp. 178-189

## APPENDIX A: DESIGN OF KALMAN FILTER BASED CARRIER AND CODE TRACKING

Provided in this section is a brief overview of an extended Kalman filter (EKF)-based signal tracking design. Initially, the design procedures are given for tracking either the data or the pilot channel independently, similar to the model described by Petovello & Lachapelle (2006). The design procedure involves deriving the state space model, process noise covariance matrix, observation model, and observation covariance matrix. Finally, the changes required for joint data/pilot tracking using KF are described.

### A.1 State Space Model

The observations for KF-based carrier and code tracking are the early, prompt, and late accumulated correlator outputs, given by

$$Y_k(\epsilon) = NA d_k R(\Delta\tau - \epsilon) \text{sinc}(\Delta f T_{coh}) \exp(j[\widetilde{\delta\phi}]) \quad (\text{A.1})$$

where  $N$  is the number of correlator samples coherently accumulated to obtain  $Y_k(\epsilon)$ ,  $A$  is the signal amplitude,  $d_k$  is the data bit sign in the  $k^{\text{th}}$  coherent integration period ( $T_{coh}$ ),  $R(\tau)$  is the autocorrelation function of the spreading code used,  $\epsilon$  is the chip spacing with respect to the prompt correlator,  $\Delta\tau$  is the code phase error,  $\widetilde{\delta\phi}$  is the average carrier phase error, and  $\Delta f$  is the carrier frequency error.  $Y_k(0.5)$ ,  $Y_k(0)$  and  $Y_k(-0.5)$  correspond to the early, prompt, and late channel accumulated correlator outputs with half chip spacing between them, respectively. They can be represented in the complex form in terms of in-phase ( $I$ ) and quadrature components ( $Q$ ) as

$$\begin{aligned} Y_k(0) &= IP_k + j QP_k \\ Y_k(0.5) &= IE_k + j QE_k \\ Y_k(-0.5) &= IL_k + j QL_k \end{aligned} \quad (\text{A.2})$$

where  $P$ ,  $E$ , and  $L$  are used to indicate prompt, early and late channels.

For carrier and code tracking using a KF, estimates of  $\widetilde{\delta\phi}$  and  $\Delta\tau$  are required. The average carrier phase error ( $\widetilde{\delta\phi}$ ) depends on the residual phase error ( $\Delta\phi$ ), frequency error ( $\Delta\omega = 2\pi\Delta f$ ) and frequency drift ( $a$ ), as follows:

$$\widetilde{\delta\phi} = \Delta\phi + \frac{\Delta\omega T_{coh}}{2} + \frac{aT_{coh}^2}{6}. \quad (\text{A.3})$$

Further, the unknown amplitude ( $A$ ) in the observations should also be included as a state in order to account for its effect. The effect of data bits can be removed by using the  $sign(I)$  operation. Hence, five states need to be estimated for carrier and code tracking and are collected in the state vector ( $\mathbf{x}$ ), defined as

$$\mathbf{x} = \begin{bmatrix} A \\ \Delta\tau \\ \Delta\phi \\ \Delta\omega \\ a \end{bmatrix}. \quad (\text{A.4})$$

In the state vector described by Eq. (A.4),  $A$  is an unknown constant; hence,

$$\dot{A} = 0 \quad (\text{A.5})$$

and the phase-frequency-frequency drift relationship is given by

$$\Delta\dot{\phi} = \Delta\omega + aT_{coh}, \quad \Delta\dot{\omega} = a, \quad \dot{a} = 0 \quad (\text{A.6})$$

for the static case, where the dynamics is due to satellite motion only. The relationship between code and carrier Doppler is given by

$$\Delta\dot{\tau} = \beta(\Delta\omega + aT_{coh}) \quad (\text{A.7})$$

where  $\beta$  is a constant scaling factor used to convert the Doppler associated with the carrier to that of the code. It is given by

$$\beta = \frac{f_{code}}{f_{carrier}} = \frac{1.023 \times 10^6}{1227.6 \times 10^6} \text{ for GPS - L2C signals.} \quad (\text{A.8})$$

The relations described in Eq. (A.5) to (A.8) are used to derive the system dynamics matrix ( $F$ ), given as

$$F = \begin{bmatrix} 0 & 0 & 0 & 0 & 0 \\ 0 & 0 & 0 & \beta & \beta T_{coh} \\ 0 & 0 & 0 & 1 & T_{coh} \\ 0 & 0 & 0 & 0 & 1 \\ 0 & 0 & 0 & 0 & 0 \end{bmatrix}. \quad (\text{A.9})$$

The system dynamics matrix given by  $F$  is in the continuous time domain. The equivalent discrete time transition matrix,  $\phi_k(\Delta t)$ , is computed from  $F$ :

$$\phi_k(\Delta t = T_{coh}) = e^{F\Delta t} = e^{FT_{coh}} \approx \begin{bmatrix} 1 & 0 & 0 & 0 & 0 \\ 0 & 1 & 0 & \beta T_{coh} & \frac{\beta T_{coh}^2}{2} \\ 0 & 0 & 1 & T_{coh} & \frac{T_{coh}^2}{2} \\ 0 & 0 & 0 & 1 & T_{coh} \\ 0 & 0 & 0 & 0 & 1 \end{bmatrix}. \quad (\text{A.10})$$

## A.2 Process Noise

The process noise matrix ( $Q$ ) is generally given by

$$Q = E[G\mathbf{w}\mathbf{w}^T G^T] \quad (\text{A.11})$$

where  $\mathbf{w}$  is the random forcing function and  $G$  is a matrix which maps the noise components (defined in  $\mathbf{w}$ ) to corresponding states ( $\mathbf{x}$ ). The values for  $\mathbf{w}$ , and hence the process noise matrix ( $Q$ ), are initially fixed in the continuous domain using Brown & Hwang (1997) and the implementation of KF based tracking available in GSNRx™ (Petovello et al 2008), and then transformed to the discrete domain.  $\mathbf{w}$  is obtained using the following four factors:

- i. Amplitude Noise :  $w_A$

Even though the state model assumes  $A$  to be a random constant, a noise process of variance  $\sigma_{w_A}^2$  is added in the process noise matrix to account for the short-term variations in  $C/N_0$  of the received signal and also to maintain the numerical stability of the algorithm (value used in this thesis:  $\sigma_{w_A}^2 = 0.5 \text{ dB}^2$ ).

ii. Code-Carrier Divergence:  $w_{\Delta\tau}$

In order to account for the difference in the effect of the ionosphere on code and carrier phases, a noise process ( $w_{\Delta\tau}$ ) is added for the state  $\Delta\tau$  (value used for  $\sigma_{w_{\Delta\tau}}$  is  $0.04 \text{ m}/\sqrt{\text{Hz}}$ ).

iii. Clock Noise:  $w_{\Delta\phi}, w_{\Delta\omega}$

The clock model from Brown & Hwang (1997) is used to initially fix the error variance parameters of the clock phase ( $w_{\Delta\phi}$ ) and clock frequency ( $w_{\Delta\omega}$ ) and then adjust them on a trial-and-error basis to arrive at the final value that fits the clock used during the collection of test data. The final values used are

$$\sigma_{w_{\Delta\phi}}^2 \approx \frac{h_0}{2} \omega_{L2}^2 = \frac{8 \times 10^{-24}}{2} \omega_{L2}^2 \quad (\text{A.12})$$

$$\sigma_{w_{\Delta\omega}}^2 \approx 2\pi^2 h_{-2} \omega_{L2}^2 = 2\pi^2 (4 \times 10^{-27}) \omega_{L2}^2 \quad (\text{A.13})$$

where  $h_0$  and  $h_{-2}$  are the power spectral density coefficients (specific to the clock used), and  $\omega_{L2}$  is the carrier frequency of the GPS-L2C signal.

iv. Line-of-Sight Acceleration Noise ( $w_a$ )

Since a static GNSS receiver is under consideration, a low value for  $\sigma_{w_a}$  is used ( $\sigma_{w_a} = 0.002 \text{ m}/(s^2\sqrt{\text{Hz}})$ ).

These four factors are used to derive the random forcing vector  $\mathbf{w}$ . The process noise matrix ( $Q$ ) in the continuous time domain is computed using  $\mathbf{w}$  and is given by

$$Q = E[G\mathbf{w}\mathbf{w}^T G^T]$$

$$= \begin{bmatrix} 1 & 0 & 0 & 0 & 0 \\ 0 & 1 & \beta & 0 & 0 \\ 0 & 0 & 1 & 0 & 0 \\ 0 & 0 & 0 & 1 & 0 \\ 0 & 0 & 0 & 0 & 1 \end{bmatrix} \begin{bmatrix} \sigma_{w_A}^2 & 0 & 0 & 0 & 0 \\ 0 & \sigma_{w_{\Delta\tau}}^2 & 0 & 0 & 0 \\ 0 & 0 & \sigma_{w_{\Delta\phi}}^2 & 0 & 0 \\ 0 & 0 & 0 & \sigma_{w_{\Delta\omega}}^2 & 0 \\ 0 & 0 & 0 & 0 & \sigma_{w_a}^2 \end{bmatrix} \begin{bmatrix} 1 & 0 & 0 & 0 & 0 \\ 0 & 1 & 0 & 0 & 0 \\ 0 & \beta & 1 & 0 & 0 \\ 0 & 0 & 0 & 1 & 0 \\ 0 & 0 & 0 & 0 & 1 \end{bmatrix}. \quad (\text{A.14})$$

The process noise matrix ( $Q_k$ ) in the discrete domain is calculated using the transformation (Gelb 1974)

$$Q_k = \int_0^{T_{coh}} \boldsymbol{\phi}_k(\tau) Q \boldsymbol{\phi}_k^T(\tau) d\tau. \quad (\text{A.15})$$

### A.3 Observation Model

The relation between the observations and the states described in Eq. (A.1) can be simplified by initially closing the frequency locked loop ( $\Delta\omega$  approaches zero) and then starting the KF-based tracking. This significantly reduces the residual frequency error ( $\Delta\omega$ ), thus allowing the elimination of the *sinc* term in Eq. (A.1). Further,  $N$  is a known constant and Eq. (A.1) can be normalized to remove its effect. Thus, the relationship between the states and the observations can be rewritten as

$$Y_k(\epsilon) = A R(\Delta\tau - \epsilon) \exp\left(j \left[ \Delta\phi + \frac{\Delta\omega T_{coh}}{2} + \frac{a T_{coh}^2}{6} \right]\right) = h(\mathbf{x}_k). \quad (\text{A.16})$$

This observation model has a nonlinear relation to the state vector ( $\mathbf{x}_k$ ), represented in Eq.(A.16) as  $h(x_k)$ . Linearization of  $h(x_k)$  is done with respect to the predicted estimate of the state vector ( $\hat{x}_k(-)$ ), at a point in time  $k$ , before the

observations  $Y_k(\epsilon)$  are recorded (hence the negative sign in the brackets). The first-order linearized model  $H_k^{[1]}$ , is given by

$$H_k^{[1]} = \left. \frac{\partial h(\mathbf{x}_k)}{\partial \mathbf{x}_k} \right|_{\hat{\mathbf{x}}_k(-)}. \quad (\text{A.17})$$

The linearized model,  $H_k^{[1]}$ , can be computed in terms of the in-phase and quadrature components, described in Eq. (A.2), as follows:

$$H_k^{[1]} = \left[ \begin{array}{ccccc} \frac{\partial(IP_k)}{\partial A} & \frac{\partial(IP_k)}{\partial(\Delta\tau)} & \frac{\partial(IP_k)}{\partial(\Delta\phi)} & \frac{\partial(IP_k)}{\partial(\Delta\omega)} & \frac{\partial(IP_k)}{\partial a} \\ \frac{\partial(QP_k)}{\partial A} & \frac{\partial(QP_k)}{\partial(\Delta\tau)} & \frac{\partial(QP_k)}{\partial(\Delta\phi)} & \frac{\partial(QP_k)}{\partial(\Delta\omega)} & \frac{\partial(QP_k)}{\partial a} \\ \frac{\partial(IE_k)}{\partial A} & \frac{\partial(IE_k)}{\partial(\Delta\tau)} & \frac{\partial(IE_k)}{\partial(\Delta\phi)} & \frac{\partial(IE_k)}{\partial(\Delta\omega)} & \frac{\partial(IE_k)}{\partial a} \\ \frac{\partial(QE_k)}{\partial A} & \frac{\partial(QE_k)}{\partial(\Delta\tau)} & \frac{\partial(QE_k)}{\partial(\Delta\phi)} & \frac{\partial(QE_k)}{\partial(\Delta\omega)} & \frac{\partial(QE_k)}{\partial a} \\ \frac{\partial(IL_k)}{\partial A} & \frac{\partial(IL_k)}{\partial(\Delta\tau)} & \frac{\partial(IL_k)}{\partial(\Delta\phi)} & \frac{\partial(IL_k)}{\partial(\Delta\omega)} & \frac{\partial(IL_k)}{\partial a} \\ \frac{\partial(QL_k)}{\partial A} & \frac{\partial(QL_k)}{\partial(\Delta\tau)} & \frac{\partial(QL_k)}{\partial(\Delta\phi)} & \frac{\partial(QL_k)}{\partial(\Delta\omega)} & \frac{\partial(QL_k)}{\partial a} \end{array} \right]_{\hat{\mathbf{x}}_k(-)}. \quad (\text{A.18})$$

As is evident from Eq. (A.16) and Eq. (A.18), the observation model involves computing the autocorrelation function  $R(\tau)$  as well as its derivatives. A model needs to be developed for this function that accounts for the effect of the pre-correlation bandwidth and also to avoid discontinuities, thus making it differentiable. In this work, as described by Petovello & Lachapelle (2006), the autocorrelation function  $R(\tau)$  is modelled using a spline function  $R_1(\tau)$ , given by

$$R_1(\tau) = \begin{cases} 0 & \tau \leq -1 - \sqrt{2}\tau_r \\ r_c - \sqrt{r_c^2 - (\tau - c_1)^2} & -1 - \sqrt{2}\tau_r < \tau \leq -1 + \tau_r \\ 1 + \tau & -1 + \tau_r < \tau \leq -\tau_r \\ 1 - 2\tau_r + \sqrt{(\{\sqrt{2}\tau_r\}^2 - \tau^2)} & -\tau_r < \tau \leq \tau_r \\ 1 - \tau & \tau_r < \tau \leq 1 - \tau_r \\ r_c - \sqrt{r_c^2 - (\tau - c_2)^2} & 1 - \tau_r < \tau \leq 1 + \sqrt{2}\tau_r \\ 0 & \tau > 1 + \sqrt{2}\tau_r \end{cases} \quad (\text{A.19})$$

where the triangular autocorrelation function is smoothed in the intervals  $(-1 - \sqrt{2}\tau_r < \tau \leq -1 + \tau_r)$ ,  $(-\tau_r < \tau \leq \tau_r)$ , and  $(1 - \tau_r < \tau \leq 1 + \sqrt{2}\tau_r)$ .  $\tau_r$  is a control parameter effecting the extent of smoothing defined in units of chips and chosen to be less than 0.05 chips.  $r_c = (2 + \sqrt{2})\tau_r$ ,  $c_1 = -1 - \sqrt{2}\tau_r$ , and  $c_2 = 1 + \sqrt{2}\tau_r$  are the other parameters used.

#### A.4 Observation Noise

The observation vector ( $Z$ ) is given by

$$Z = [IP_k \quad QP_k \quad IE_k \quad QE_k \quad IL_k \quad QL_k]^T. \quad (\text{A.20})$$

The observation covariance matrix is derived based on the following facts:

- i. The noise corrupting the early, prompt, and late observations is considered to be zero mean white Gaussian noise, with variance ( $\sigma_{I/Q}^2$ ) given by

$$\sigma_{I/Q}^2 = \frac{A^2}{4 \left(\frac{C}{N_0}\right)_r T_{coh}} \quad (\text{A.21})$$

where  $\left(\frac{C}{N_0}\right)_r$  is  $C/N_0$  expressed as a ratio.

- ii. The in-phase and quadrature components of the observations are uncorrelated:  $E[IE_k QE_k] = E[IP_k QP_k] = E[IL_k QL_k] = E[IE_k QP_k] = 0$  etc.
- iii. Similarly, the correlation coefficient ( $\rho$ ) of in-phase and quadrature components of the prompt channel with that of early or late channel is given by their chip spacing ( $\epsilon$ ) with respect to the prompt channel, i.e.
- $$\rho_{IP_k IE_k} = \rho_{IP_k, IL_k} = \rho_{QP_k, QE_k} = \rho_{QP_k, QL_k} = (1 - |\epsilon|).$$
- iv. The correlation coefficient between the early and late channel observations is given by  $\rho_{IE_k IL_k} = \rho_{QE_k QL_k} = 1 - 2|\epsilon|$ .

Hence, the observation noise covariance matrix ( $R$ ) is

$$R = \sigma_{I/Q}^2 \begin{bmatrix} 1 & 0 & (1 - |\epsilon|) & 0 & (1 - |\epsilon|) & 0 \\ 0 & 1 & 0 & (1 - |\epsilon|) & 0 & (1 - |\epsilon|) \\ (1 - |\epsilon|) & 0 & 1 & 0 & (1 - 2|\epsilon|) & 0 \\ 0 & (1 - |\epsilon|) & 0 & 1 & 0 & (1 - 2|\epsilon|) \\ (1 - |\epsilon|) & 0 & (1 - 2|\epsilon|) & 0 & 1 & 0 \\ 0 & (1 - |\epsilon|) & 0 & (1 - 2|\epsilon|) & 0 & 1 \end{bmatrix}. \quad (\text{A.22})$$

The derived  $\phi_k$ ,  $Q_k$ ,  $H$  and  $R$  matrices are then used in the standard extended Kalman filter equations, and the output phase and frequency estimates are fed to the numerically-controlled oscillator in the tracking module.

### A.5 Necessary Changes for Joint Data/Pilot Tracking

The state vector ( $\mathbf{x}_k$ ) and the process noise matrix ( $Q_k$ ), derived in section A.1 and A.2 remain unchanged during joint data/pilot tracking. The observation vector ( $Z_{dp}$ ) is updated to include both data and pilot channel observations, as such:

$$Z_{dp} = [Z_{data}^T \quad Z_{pilot}^T]^T \quad (\text{A.23})$$

where  $Z_{data}$  and  $Z_{pilot}$  are the observation vectors from the data and pilot channels respectively, as described in Eq. (A.20). The joint data/pilot observation covariance matrix ( $R_{dp}$ ) accounts for the fact that data and pilot channel accumulated correlator outputs are statistically independent, and thus corrupted by independent-and-identical noise components (equal variance, zero mean etc.). Hence,  $R_{dp}$  for the joint data/pilot case is given as

$$R_{dp} = \begin{bmatrix} R_{data} & 0 \\ 0 & R_{pilot} \end{bmatrix} \quad (\text{A.24})$$

where  $R_{data} = R_{pilot} = R$ , which is defined in Eq. (A.22).

Thus, all 12 observations (or six complex observations) are used to estimate the states required for carrier and code tracking. The  $C/N_0$  estimates used for determining  $\sigma_{I/Q}^2$  are obtained from the joint data/pilot ML  $C/N_0$  estimator (with iteration) described in Chapter 3.

**APPENDIX B: IDENTITIES USED IN THE DERIVATION OF CRLB FOR  $C/N_0$  ESTIMATION**

**B.1 Identity 1**

If the pdf,  $p(y_m; \boldsymbol{\theta})$ , of a random variable  $y_m$  is distributed as

$$p(y_m; \boldsymbol{\theta}) = \frac{1}{\sqrt{2\pi K \sigma_n^2}} \exp\left(-\frac{1}{2K\sigma_n^2} [y_m^2 + K^2 A^2]\right) \cosh\left(\frac{y_m A}{\sigma_n^2}\right) \quad (\text{B.1})$$

where  $K$  is a positive integer ( $K > 1$ ), and  $A$  and  $\sigma_n^2$  are positive real quantities, and  $\boldsymbol{\theta}$  is the vector of unknown parameters,  $[A \quad \sigma_n^2]^T$ , then

$$E \left[ \frac{y_m^2}{\cosh^2\left(\frac{A}{\sigma_n^2} y_m\right)} \right] = \sigma_n^2 h(\alpha, K). \quad (\text{B.2})$$

*Proof:*

The expectation is taken with respect to  $p(y_m; \boldsymbol{\theta})$ . Evaluating the left hand side of Eq.

(B.2) leads to

$$E \left[ \frac{y_m^2}{\cosh^2\left(\frac{A}{\sigma_n^2} y_m\right)} \right] = \frac{\sigma_n^2 \exp(-K\alpha)}{\sqrt{2\pi K}} \int_{-\infty}^{+\infty} \left(\frac{y_m}{\sigma_n}\right)^2 \frac{\exp\left(-\frac{1}{2K}\left(\frac{y_m}{\sigma_n}\right)^2\right)}{\cosh\left(\frac{A}{\sigma_n} \frac{y_m}{\sigma_n}\right)} \frac{dy_m}{\sigma_n} \quad (\text{B.3})$$

and substituting  $u = \frac{y_m}{\sigma_n}$ ,  $du = \frac{dy_m}{\sigma_n}$ , Eq. (B.3) is simplified as follows:

$$E \left[ \frac{y_m^2}{\cosh^2\left(\frac{A}{\sigma_n^2} y_m\right)} \right] = \sigma_n^2 \frac{\exp(-K\alpha)}{\sqrt{2\pi K}} \int_{-\infty}^{+\infty} \frac{u^2 \exp\left(-\frac{u^2}{2K}\right)}{\cosh(u\sqrt{2\alpha})} du. \quad (\text{B.4})$$

Define:  $h(\alpha, K)$  as (as given in Chapter 3)

$$h(\alpha, K) = \frac{\exp(-K\alpha)}{\sqrt{2\pi K}} \int_{-\infty}^{+\infty} \frac{u^2 \exp\left(-\frac{u^2}{2K}\right)}{\cosh(u\sqrt{2\alpha})} du. \quad (\text{B.5})$$

Substituting Eq.(B.5) in Eq.(B.4) proves the identity.

## B.2 Identity 2

If a random variable  $r$  is distributed as  $p(r; \boldsymbol{\theta})$ , given by

$$p(r; \boldsymbol{\theta}) = \frac{\exp\left(-\frac{r^2}{2\sigma_n^2}\right) \exp\left(-\frac{A^2}{2\sigma_n^2}\right)}{\sqrt{2\pi\sigma_n^2}} \cosh\left(\frac{rA}{\sigma_n^2}\right) \quad (\text{B.6})$$

then

$$E\left[r \tanh\left(\frac{rA}{\sigma_n^2}\right)\right] = A. \quad (\text{B.7})$$

*Proof:*

The left hand side of the identity is evaluated to prove the equality as follows:

$$\begin{aligned} & E\left[r \tanh\left(\frac{rA}{\sigma_n^2}\right)\right] \\ &= \frac{1}{\sqrt{2\pi\sigma_n^2}} \exp\left(-\frac{A^2}{2\sigma_n^2}\right) \int_{-\infty}^{+\infty} r \tanh\left(\frac{rA}{\sigma_n^2}\right) \exp\left(-\frac{r^2}{2\sigma_n^2}\right) \cosh\left(\frac{rA}{\sigma_n^2}\right) dr \\ &= \frac{1}{\sqrt{2\pi\sigma_n^2}} \exp\left(-\frac{A^2}{2\sigma_n^2}\right) \int_{-\infty}^{+\infty} r \sinh\left(\frac{rA}{\sigma_n^2}\right) \exp\left(-\frac{r^2}{2\sigma_n^2}\right) dr \\ &= \frac{1}{2} \frac{1}{\sqrt{2\pi\sigma_n^2}} \exp\left(-\frac{A^2}{2\sigma_n^2}\right) \int_{-\infty}^{+\infty} r \left[ \exp\left(\frac{rA}{\sigma_n^2}\right) - \exp\left(-\frac{rA}{\sigma_n^2}\right) \right] \exp\left(-\frac{r^2}{2\sigma_n^2}\right) dr \\ &= \frac{1}{2} \frac{1}{\sqrt{2\pi\sigma_n^2}} \int_{-\infty}^{+\infty} \left\{ r \exp\left(\frac{1}{2\sigma_n^2}[r - A]^2\right) - r \exp\left(\frac{1}{2\sigma_n^2}[r + A]^2\right) \right\} dr \\ &= \frac{1}{2} \left( E\left[r; \left[\frac{+A}{\sigma_n^2}\right]\right] - E\left[r; \left[\frac{-A}{\sigma_n^2}\right]\right] \right) = \frac{1}{2}(A - (-A)) = A. \end{aligned} \quad (\text{B.8})$$

### APPENDIX C: CRLB FOR PHASE ESTIMATION IN AWGN CHANNEL

This appendix provides the derivation of the Cramer-Rao lower bound (CRLB) for phase estimation using a prompt channel accumulated correlator output corrupted by additive white Gaussian noise (AWGN). The signal model for the accumulated correlator output ( $x$ ) is assumed to be

$$x = A \exp(j\Delta\phi) + n_I + jn_Q = x_i + jx_q \quad (\text{C.1})$$

where  $A$  is the signal amplitude,  $\Delta\phi$  is the phase error, and  $n = n_I + jn_Q$  is the complex noise sample corrupting the observation. The pdf of  $n$  follows  $\mathcal{N}(0, \sigma_n^2)$ , hence  $n_I$  and  $n_Q$  are identical and independently distributed as  $\mathcal{N}\left(0, \frac{\sigma_n^2}{2}\right)$ .  $x_i$  and  $x_q$  are the real and imaginary parts of the observation  $x$ , respectively. The noise variance ( $\sigma_n^2$ ) and signal power ( $A^2$ ) are related to the carrier-to-noise density ( $C/N_0$ ) as (Kaplan 2006)

$$\frac{A^2}{\sigma_n^2} = \left(\frac{C}{N_0}\right)_r T_{coh} \quad (\text{C.2})$$

where  $(C/N_0)_r$  is the  $C/N_0$  expressed as a ratio and  $T_{coh}$  is the predetection interval.

The unknown parameters in  $x$  are given by  $\boldsymbol{\theta}$  as

$$\boldsymbol{\theta} = [A \quad \sigma_n^2 \quad \Delta\phi]^T. \quad (\text{C.3})$$

The pdf ( $p(x; \boldsymbol{\theta})$ ) of the observation ( $x$ ) can be given as

$$p(x; \boldsymbol{\theta}) = \frac{1}{\pi\sigma_n^2} \exp\left(-\frac{1}{\sigma_n^2} ([x_i - A \cos \Delta\phi] + [x_q - A \sin \Delta\phi])\right). \quad (\text{C.4})$$

Defining  $P \equiv \ln(p(x; \boldsymbol{\theta}))$ ,  $P$  can be written as

$$P = -\ln \pi\sigma_n^2 - \frac{1}{\sigma_n^2} (x_i^2 + x_q^2) - \frac{A^2}{\sigma_n^2} + \frac{2A}{\sigma_n^2} (x_i \cos \Delta\phi + x_q \sin \Delta\phi). \quad (\text{C.5})$$

The elements of Fisher information matrix ( $I(\boldsymbol{\theta})$ ) are obtained from  $P$  as

$$\frac{\partial P}{\partial A} = -\frac{2A}{\sigma_n^2} + \frac{2}{\sigma_n^2}(x_i \cos \Delta\phi + x_q \sin \Delta\phi)$$

$$\frac{\partial^2 P}{\partial A^2} = -\frac{2}{\sigma_n^2}$$

$$[I(\boldsymbol{\theta})]_{11} = -E \left[ \frac{\partial^2 P}{\partial A^2} \right] = \frac{2}{\sigma_n^2} \quad (\text{C.6})$$

$$\frac{\partial P}{\partial \sigma_n^2} = -\frac{1}{\sigma_n^2} + \frac{1}{\sigma_n^4}(x_i^2 + x_q^2) + \frac{A^2}{\sigma_n^4} - \frac{2A}{\sigma_n^4}(x_i \cos \Delta\phi + x_q \sin \Delta\phi)$$

$$\frac{\partial^2 P}{\partial \sigma_n^4} = \frac{1}{\sigma_n^4} - \frac{2}{\sigma_n^6}(x_i^2 + x_q^2) - \frac{2A^2}{\sigma_n^6} + \frac{4A}{\sigma_n^6}(x_i \cos \Delta\phi + x_q \sin \Delta\phi)$$

$$-E \left[ \frac{\partial^2 P}{\partial \sigma_n^4} \right] = -\frac{1}{\sigma_n^4} + \frac{2}{\sigma_n^6} E(x_i^2 + x_q^2) + \frac{2A^2}{\sigma_n^6} - \frac{4A}{\sigma_n^6} (E(x_i) \cos \Delta\phi + E[x_q] \sin \Delta\phi)$$

$$= -\frac{1}{\sigma_n^4} + \frac{2}{\sigma_n^6} \left( A^2 \cos^2 \Delta\phi + \frac{\sigma_n^2}{2} + A^2 \sin^2 \Delta\phi + \frac{\sigma_n^2}{2} \right) + \frac{2A^2}{\sigma_n^6}$$

$$- \frac{4A}{\sigma_n^6} (A \cos^2 \Delta\phi + A \sin^2 \Delta\phi)$$

$$[I(\boldsymbol{\theta})]_{22} = -E \left[ \frac{\partial^2 P}{\partial \sigma_n^4} \right] = \frac{1}{\sigma_n^4} \quad (\text{C.7})$$

$$\frac{\partial P}{\partial \Delta\phi} = \frac{2A}{\sigma_n^2} (-x_i \sin \Delta\phi + x_q \cos \Delta\phi)$$

$$\frac{\partial^2 P}{\partial (\Delta\phi)^2} = \frac{2A}{\sigma_n^2} (-x_i \cos \Delta\phi - x_q \sin \Delta\phi)$$

$$[I(\boldsymbol{\theta})]_{33} = -E \left[ \frac{\partial^2 P}{\partial (\Delta\phi)^2} \right] = \frac{2A^2}{\sigma_n^2} \quad (\text{C.8})$$

$$\frac{\partial^2 P}{\partial \sigma_n^2 \partial A} = +\frac{2A}{\sigma_n^4} - \frac{2}{\sigma_n^4} (x_i \cos \Delta\phi + x_q \sin \Delta\phi)$$

$$[I(\boldsymbol{\theta})]_{12} = -E \left[ \frac{\partial^2 P}{\partial \sigma_n^2 \partial A} \right] = 0 \quad (\text{C.9})$$

$$\frac{\partial^2 P}{\partial \Delta \phi \partial A} = \frac{2}{\sigma_n^2} (-x_i \sin \Delta \phi + x_q \cos \Delta \phi)$$

$$[I(\boldsymbol{\theta})]_{13} = -E \left[ \frac{\partial^2 P}{\partial \phi \partial A} \right] = 0 \quad (\text{C.10})$$

$$\frac{\partial^2 P}{\partial \Delta \phi \partial \sigma_n^2} = -\frac{2A}{\sigma_n^4} (-x_i \sin \Delta \phi + x_q \cos \Delta \phi)$$

$$[I(\boldsymbol{\theta})]_{23} = -E \left[ \frac{\partial^2 P}{\partial \phi_r \partial \sigma_n^2} \right] = 0 \quad (\text{C.11})$$

Thus, the Fisher information matrix is given as

$$I(\boldsymbol{\theta}) = \begin{bmatrix} \frac{2}{\sigma_n^2} & 0 & 0 \\ 0 & \frac{1}{\sigma_n^4} & 0 \\ 0 & 0 & \frac{2A^2}{\sigma_n^2} \end{bmatrix}. \quad (\text{C.12})$$

Hence, the CRLB for estimate of phase error ( $\Delta \phi$ ) from a given sample  $x$  is given by

$$\text{var}(\Delta \hat{\phi}) \geq \frac{\sigma_n^2}{2A^2} = \frac{1}{2(C/N_0)_r T_{coh}}. \quad (\text{C.13})$$